Melt Productivity of Aluminous Anatectic Rocks of the Central Grenville Province and Characterization of Potential Anatectic Granite Layers

By

Daniela Mendoza Marin

A thesis submitted to the School of Graduate Studies in partial fulfillment of the
requirements for the degree of Master of Science

Department of Earth Sciences
Memorial University of Newfoundland

January 2023

Abstract

Partial melting of middle to lower crust plays an important role in the evolution of large hot orogens and is a major source of S-type granites in orogenic crust. However, such granites seem to be scarce in the Mesoproterozoic Grenville Province. This project explores the melt productivity of aluminous anatectic rocks of the central Grenville Province, focusing mainly on metapelites of the Plus Value Complex (PLV; mid-*P* belt) that were metamorphosed during the Ottawan phase of the Grenvillian orogeny, and on leucocratic layers and scarce granite exposures of potentially anatectic origin. The mineral assemblage of the PLV metapelites is consistent with the biotite dehydration melting reaction: biotite + Al-silicate ± plagioclase + quartz = garnet + K-feldspar + melt, and its good preservation is suggestive of significant melt loss during prograde metamorphism. Based on phase equilibria modelling, maximum *P*–*T* conditions of about ~10.6–10.7 kb and 860–903 °C, and moderate gradient *P*–*T* paths, are inferred. Additionally, phase equilibria modelling predicts that the rocks produced up to 45% of melt with ~ 6–8% having remained in situ. With increasing *T* the modelled melts show a general increase in K_2O and decrease in Na_2O, an evolution from granodioritic to monzogranitic compositions, and an increase in peraluminosity. Broadly similar trends are also observed in modelled melts using other types of mid-*P* aluminous rocks from the wider area, and high-*P* rocks from structurally lower levels. On the other hand, leucocratic layers associated with the PLV metapelites and the granite exposures have minor amounts of garnet, biotite, and (in some cases), sillimanite, and are peraluminous and monzogranites. Monazite in the PLV granites show morphologies and chemical patterns ranging from complex, consistent with several episodes of growth and resorption, to simple, and provide evidence for growth (of part of the monazites, at least) in the presence of melt. Dominant $^{206}Pb/^{238}U$ monazite ages range from 1062 ± 17 to 1033 ± 10 Ma and are similar to those of the metamorphic ages of the PLV aluminous rocks (1080 – 1040 Ma) reported from the literature. Even though processes such as mixing of melts, fractional crystallization and wall-rock contamination are not assessed, the PLV granites seem to be related to the PLV aluminous rocks. They most likely represent melts produced by the biotite melting reaction and could be the first documented S-type granites of Ottawan age in the central Grenville Province.

Acknowledgments

First and foremost, I would like to thank Dr. Aprhodite Indares for her guidance, insight, support, patience, and all the time she dedicated to this project. I am beyond grateful and feel incredibly honoured to have been under her supervision these past three years.

Secondly, I would like to thank my committee member, Dr. Gregory Dunning, who also guided and provided me with valuable advice, particularly on the geochronology part of this project. It was a privilege to work with him.

I want to thank my amazing research group. Susan Strowbridge, for being there for me every single time I needed help with anything, THERMOCALC, thin sections, how to deal with the world, etc. Thank you from the bottom of my heart; you truly made everything easier for me. Kirsten Costello, for having the nicest disposition to assist me with anything I needed, thank you for guiding me through my first semesters here. Lastly, but not least, Elliot Hoyle, Dr. Caroline Lotout, Arlin Fonseca and Ivan Yip, for their support and unconditional help.

Additionally, I'd like to thank the CREAIT Network at MUN. Dr. Wanda Aylward, Dylan Goudie and Dr. Markus Wälle for their assistance with the EPMA, SEM-MLA imaging, and LA-ICP-MS.

My family and friends, for supporting me in going alone across the world to pursue my dreams; I would not have done this without you. Thank you for encouraging me every day. You are my everything.

This research was supported by NSERC Discovery Grant to Dr. Aphrodite Indares. I would also like to thank the School of Graduate Studies for its financial support throughout my master's program.

Table of Contents

List of Tables

Chapter 2

Chapter 3

Chapter 4

Chapter 5

List of Figures

Chapter 1

Chapter 3

Chapter 4

Chapter 5

present bulk composition, from the dry solidus to the biotite-out line. Dotted and solid black line represent results from closed and open system, respectively from Pavan et al., 2021.

LIST OF APPENDICES

Appendix C: Phase Equilibria Modelling Data

- Appendix C1: Bulk composition calculations.
    - Appendix C1.1: Bulk composition calculation of the PLV1 sample HJ-60c.
    - Appendix C1.2: Bulk composition calculation of the PLV1 sample HJ-88D2.
    - Appendix C1.3: Bulk composition calculation of the PLV2 sample 12-AI-10Y.
- Appendix C2: Additional diagrams not used in the thesis.

1 CHAPTER 1: Introduction and Background

1.1 Aim

Partial melting plays a major role in the evolution of the crust in mountain belts (Brown, 2010; Rosenberg and Handy, 2005), most particularly in large hot orogens (Beaumont et al., 2006; Jamieson and Beaumont, 2013). The Mesoproterozoic Grenville Province in eastern Canada (Rivers et al., 2012) is an exceptional location to study high-temperature (*T*) processes due to the wide exposure of middle to lower crust, dominated by granulite-facies rocks (Fig. 1.1). These exposures have provided the basis for the classification of the Grenville Province as a large hot orogen.

In the central Grenville Province, aluminous anatectic rocks of broadly pelitic composition are present in both the mid-pressure (*P*) and high-*P* belts of the orogen (Fig. 1.2) and provide varied microstructural evidence of partial melting and melt loss during the Ottawan phase of the Grenvillian orogeny (e.g., Indares et al., 2008; Lasalle and Indares, 2014). However, granitic products of the migrated melt have not been identified yet (probably because they moved to higher structural levels, now eroded), except for rare metric scale exposures of biotite-garnet bearing granite, of potentially anatectic origin, in the mid-*P* belt.

This project evaluates the melt productivity of aluminous anatectic rocks from the central Grenville Province, primarily focusing on metapelites from the Plus Value Complex (PLV; Moukhsil et al., 2012) of the mid-*P* belt, but also considering other aluminous rocks from the high-*P* and the mid-*P* belts. The PLV metapelites exhibit varied relations between restite and leucosome, and the granitic bodies of potentially anatectic origin were observed in the same area. This study explores potential links between the anatexis of the aluminous rocks and these granites using mineral assemblages and their microstructures in thin sections, phase equilibria modelling, monazite geochronology, and bulk-rock geochemistry. If they are indeed the product of partial melting of the PLV metapelitic rocks, these granite bodies would represent the first documented S-type granites of Ottawan age in the central Grenville Province.

1.2 Background in Anatectic Aluminous Rocks

Partial melting is common in high-*T* tectonic environments and leads to important rheological changes in the crust such as the development of a low-viscosity layer, a ductile and flowing lower-middle crust that facilitates the exhumation of high-grade rocks (Vanderhaeghe and Teyssier, 2001). The weakness generated in the partially molten areas allows the crust to flow at faster geological strain rates, between tectonic detachment horizons (Yakymchuk and Brown, 2014 and references herein). In addition, anatectic melts tend to migrate out of their source, to produce granites (Brown, 2010).

The present study focuses on metapelites that have undergone anatexis in middle to lower orogenic crust in the central Grenville Province. Metamorphosed aluminous rocks such as metapelites, exhibit a wide range of mineral assemblages that evolve as the P–T conditions change, making them one of the most diagnostic lithologies for deciphering the metamorphic history of geological terrains (Palin and Dyck, 2021). In addition, they typically experience widespread partial melting at granulite-facies conditions, therefore they are key rocks for the study of anatectic processes in the crust (Brown, 2010). Tools commonly used to decode the partial melting history of aluminous anatectic rocks include documentation of microstructures and their interpretation in terms of melt-producing reactions, phase equilibria modelling, and dating using zircon, monazite, and garnet.

1.2.1 Melting reactions in pelitic systems

In middle to high-pressure aluminous rocks, partial melting can first occur by fluid-consuming reactions at upper amphibolite-facies conditions (Fig. 1.3). However, the proportion of melt produced by these reactions is not expected to be high, since the amount of fluid at the wet solidus is limited by the poor porosity of high-grade metamorphic rocks (Yardley and Valley, 1997). In these systems, large amounts of melt are produced at higher temperatures, by reactions that involve the breakdown of hydrous minerals where their OH is transferred to the melt. This starts with muscovite dehydration melting reactions such as:

$$[R1]\ Ms \pm Pl + Qtz = Als + Kfs + melt$$

(Fig.1.3; abbreviations are after Whitney and Evans, 2010). This reaction also consumes plagioclase (if present) and quartz, and in addition to melt, it produces K-feldspar and aluminum silicate (sillimanite or kyanite, depending upon the pressure). R1 can produce amounts of melt as high as 70% of the initial volume of muscovite (Spear et al., 1999). Once muscovite is exhausted, partial melting continues with the breakdown of biotite with aluminum silicate, plagioclase (if present) and quartz, to produce melt, garnet or cordierite, and K-feldspar. The consumption of biotite through this reaction may produce ~30% of melt, and it can be generalized by the following continuous reaction (Spear et al., 1999):

$$[R2]\ Bt + Als\ \pm Pl +\ Qtz = Grt/Crd + Kfs +\ melt$$

Based on natural and experimental observations, melt starts forming as a thin film at grain edges and as cuspate pockets between the reactant minerals. These minerals, with time, become more resorbed or embayed and usually end up as small, rounded inclusions inside the melt (Holness, 2008; Holness and Sawyer, 2008). Moreover, the experiments show that melt tends to accumulate in pools with triangular cuspate margins with concave outlines since the bordering reactant minerals are resorbed by the melt-producing reactions. On the other hand, when the melt is crystallizing, the minerals that form tend to develop crystal faces towards the melt side. These minerals may grow as new grains, or they may form overgrowths on the reactants (Jurewicz and Watson, 1985; Sawyer, 2001).

Commonly the melt generated in anatectic rocks migrates from its source and forms domains/layers of leucosome spatially associated with the source rocks, or even distal granite bodies. Nevertheless, a minor quantity of melt stays in the residuum where it fills grain corners or can occur as films or veinlets (Sawyer, 2008). Melt-producing reactions and metamorphism conditions can be best assessed using microstructures in the residuum because this part of the anatectic rocks contains minerals that were present during melting.

1.2.2 Phase Equilibria Modelling

Phase equilibria modelling can provide varied insights on the evolution of aluminous anatectic rocks. *P–T* pseudosections calculated for specific bulk rock compositions show the distribution of stable mineral assemblages in a selected *P–T* range and provide the framework to interpret microstructures and mineral chemistry in terms of *P–T* paths. In addition, they can be used to calculate melt compositions at different *P–T* conditions, and to add melt to residual bulk rock compositions to account for presumed lost melt (Powell and Holland, 2010).

Melt calculations for anatectic aluminous rocks has become a hot research topic. For instance, Yakymchuk and Brown (2014), investigated the volume of melt produced by average pelite and greywacke and its implications in tectonics. They considered two different environments: a closed-system where melt is retained and an open-system where the melt is removed cyclically. They noted that some leucosomes and/or granites may be the result of migration of melt followed by its accumulation at shallow levels and stated that this process should be considered as the cause of exhumation of suprasolidus crust, rather than the production of large amounts of melt due to decompression. However, this study did not consider the change of composition of the melt fraction produced as melting progresses. On the other hand, Koblinger and Pattison (2017) examined the variation in the composition of leucosomes due to different melting and crystallization processes. They determined the leucosome composition is mainly influenced by the composition of the melt rather than the type of crystallization process (fractional crystallization, crystallization of only the melt separated from the solid phases, and crystallization of the melt in contact with the solid phases).

Most recently, Pavan et al. (2021) modelled bulk compositions of greywacke and shale to compare the evolution of the residue and anatectic melt with increasing temperature, in both closed and open systems at different pressure. Their results are consistent with natural observations, suggesting the effectiveness of using modelling to provide more insight into the residue-leucosome linkage.

1.2.3 Dating anatectic processes

There are several mineral chronometers that can be used to add time constraints on the evolution of anatectic systems (e.g., zircon, monazite, apatite, garnet). Here the focus will be on monazite, since this chronometer has been the most widely used in aluminous rocks of the central Grenville Province (Indares and Dunning, 2001; Dunning and Indares, 2010; Lassalle et al., 2014).

Monazite is an accessory monoclinic, rare-earth elements-rich phosphate mineral [(Ce, La, Nd, Th) PO4] commonly found in felsic igneous rocks, and aluminous quartzofeldspathic metamorphic rocks. Its high content of U and Th (up to 27 oxide wt.%) make monazite suitable for U–Pb dating using ID-TIMS (Isotope Dilution Thermal Ionization Mass Spectrometry), in situ LA_ICP MS (Laser Ablation Inductively Coupled Plasma Mass Spectrometry), and IMP (Ion Microprobe) techniques (Patchett and Samson, 2003). In addition, owing to slow elemental diffusion, monazite commonly preserves distinct composition domains and ages that can add constraints to its growth history (Kelsey et al., 2008).

Yakymchuk et al. (2017) modelled the behaviour of monazite in anatectic systems and distinguished 4 types of monazite: detrital, produced by solid-state prograde reactions, precipitated from a fluid, and crystallized from anatectic melt. In suprasolidus systems, earlier monazite tends to dissolve in melt during anatexis and then, new monazite grows during melt crystallization, upon cooling. The modelling inferred that the solubility of monazite increases with increasing H_20 contents in the melt and with decreasing P concentrations, whereas monazite crystallization is controlled by the temperature, pressure, and the bulk composition of the melt. Kelsey et al. (2008) and Yakymchuk and Brown (2014) used phase equilibria modelling and solubility equations to show that the dissolution of monazite increases with prograde metamorphism, meaning that for ultra-high-temperature metamorphism, most monazite will be consumed. However, prograde, or earlier, inherited monazite commonly persists in suprasolidus rocks, mostly as inclusions in other minerals.

In anatectic rocks, different types of monazite can also be identified based on changing Th and Y contents during prograde metamorphism, melting and melt crystallization (Fig. 1.4). This allows the identification of three important domains: (1) early formed monazite, with high Th and Y -not in the rim-; (2) late-prograde monazite, with low Y and Th domains; and (3) post-anatectic monazite, with high Y and Th overgrowths (Kohn, 2016). Early monazite forms with high Th and Y content, from the breakdown of LREE-rich clays, or Th, LREE oxides and hydrous phosphates (Yakymchuk et al., 2017 and references herein). During later solid-state prograde reactions, the Y content of monazite decrease due to the growth of garnet (major mineral sink for HREE; Yakymchuk et al., 2017). Because monazite is a sink for Th, any further growth will deplete the matrix in Th and therefore in any later-grown monazite. During anatexis, some monazite dissolves and upon melt crystallization, new monazite grows with high Th and Y linked to garnet breakdown at this stage. This new monazite grows as discrete grains, or as overgrowths on relict, earlier grains. The late-prograde and post-anatectic monazite frame the time of melting and peak metamorphism. In this manner, the Th and Y contents of monazite from anatectic rocks are considerably useful to determine different generation domains, which along with the monazite U–Pb ages link the mineral reaction history with regions of the *P–T* space; allowing to get more details of the tectonic events the rock went through (Kohn, 2016). On the downside, although the trends in Th and Y summarized above provide useful guidelines to interpret monazite history, commonly the observed patterns are less straightforward (eg. see Hetherington et al., 2017).

In the specific cases of leucosomes and anatectic granites, it is expected that monazite would dominantly form during melt crystallization. However, older relicts, entrained in the melt from the host rocks, may persist if the melt reached saturation in P before dissolving all the monazite present. These two types can be possibly separated by morphology and Th and Y content (Kohn, 2016).

1.3 Geological Setting

1.3.1 The Grenville Province

The Grenville Province extends along the east coast of North America, from the Labrador Sea to Texas and Mexico (Fig.1.1). It consists of terranes formed in an active margin along the eastern border of the Laurentian continent from ~1.8 to 1.2 Ga (Rivers and Corrigan, 2000), later reworked by continental collision (Grenvillian Orogeny) during the establishment of the Rodinia supercontinent at ~ 1.09–0.98 Ga (Tohver et al., 2004). The Grenville Province is classified as a large hot orogen based on its large dimensions, the long duration of the orogeny, and the widespread exposure of granulite-facies rocks (Rivers et al., 2012).

Overviews of the Grenville Province are published in a series of papers by Rivers (2008, 2012, 2015; also, Rivers et al. 2012). Tectonically, the Grenville Province is divided into two parts by the Allochthonous boundary thrust; The Parautochthonous Belt at the NW, consists of Archean and Proterozoic rocks directly correlated with the foreland of the orogen and metamorphosed during the late stages of the Grenvillian orogeny (Rigolet phase: 1000 – 980 Ma) under greenschist to granulite facies conditions. On the other hand, the Allochthonous Belt (or hinterland) to the SE, consists of Paleoproterozoic to Mesoproterozoic rocks most of which represent the orogenic infrastructure and were metamorphosed under upper amphibolite and granulite facies conditions but at contrasting pressures (high, mid, and low-*P* belts) during the main phase of the Grenvillian orogeny (Ottawan phase: 1090–1020 Ma). The orogenic suprastructure, or orogenic lid, located at the uppermost structural levels of the hinterland, is the only area unaffected by Grenvillian-age, high *P*–*T* metamorphism.

Tectonic models for the Grenville Province involve development of a ductile, low-viscosity layer in the middle to lower parts of the thickened crust, and generation of an orogenic plateau (e.g., Jamieson et al., 2007; Rivers 2008). Jamieson et al. (2010) and Jamieson and Beaumont (2011) used thermal-mechanical models to examine the possible effects of syn- and post-convergent ductile flow in the exhumation of high-grade rocks in western and central Grenville. Moreover, a collapsed orogenic plateau was proposed by Rivers (2012) as the driving mechanism of the resulting structure of the Grenville Province.

1.3.2 Geological outline of the central Grenville Province

A review of the makeup and metamorphic framework of the central Grenville Province was recently published by Indares (2020). In this area, all the different levels of the hinterland and the Parautochthonous Belt are exposed (Fig.1.2). This study is mainly focused on aluminous rocks of the mid-*P* belt and on those from the southern part of the high-*P* belt, on both sides of the Manicouagan reservoir.

The high-*P* belt in the central Grenville Province mostly comprises Labradorian-age (~1.65 Ga) anorthositic and plutonic mafic rocks. In addition, anatectic aluminous rocks of uncertain affiliation (the type of protoliths is not known) sporadically occur at the southern margin of the high-*P* belt. By contrast, the mid-*P* belt mainly consists of Pinwarian-age (~1.50 to 1.45 Ga) plutonic and metasedimentary rocks, transected by a 1.23 Ga supracrustal belt of volcaniclastic origin (Indares and Moukhsil, 2013; Lasalle et al., 2013). Aluminous rocks are found in the Plus Value (PLV) metasedimentary sequence with a deposition age of 1.5 Ga (Moukhsil et al., 2012; Lasalle et al., 2013), where they are interpreted as metapelites; and as rocks of broadly pelitic composition that are the metamorphic products of hydrothermally altered felsic rocks (HAF) in the 1.23 Ga supracrustal sequence (Hindemith et al., 2017). South of the Manicouagan reservoir, the PLV is intruded by an A-type, hornblende-bearing Ottawan-age (1.06 Ga) granitic pluton and several Rigolet-age (990 to 980 Ma) ultrapotassic dykes and felsic pegmatites (Dunning and Indares, 2011; Turlin et al., 2017).

1.3.3 Previous work in anatectic aluminous rocks from the central Grenville Province

Aluminous rocks of the mid-and high-*P* belts of the central Grenville mainly consist of garnet ± biotite–K-feldspar ± plagioclase–quartz–Al-silicate. Al-silicate is kyanite and sillimanite in the high-*P* and mid-*P* belts respectively (Indares, 2000 and references herein). Cordierite has only been found as a retrograde phase in some HAF samples (Patrick and Indares, 2017). The rocks exhibit melt-related microstructures, consistent with biotite dehydration melting, and subsequent melt crystallization similar as the PLV metapelites (Lasalle and Indares

2014). These microstructures were documented by optical microscopy, Scanning Electron Microscopy (SEM) imaging of thin sections, and cathodoluminescence (CL) mapping of quartz and kyanite (Indares, 2020, Kendrick and Indares, 2018a, b).

The age of the metamorphism of the aluminous rocks is constrained by monazite dating. U–Pb TIMS ages of monazite from the high-*P* belt are mostly in the range of 1040–1030 Ma (Dunning and Indares, 2010; Indares and Dunning, 2001). In the mid-*P* belt, monazite from metapelites of the PLV exhibit an age range from 1059 to 1067 Ma, but farther north in the same belt, HAF rocks are younger e.g., 1040–1000 Ma. The ages are spread even at the sample scale, consistent with an episodic growth of monazite during Ottawan metamorphism (Dunning and Indares, 2010). In addition, U–Pb dating of monazite from the same samples by ICP-MS showed that part of the spread of the TIMS data is due to a late monazite growth event at 1010–990 Ma, during the Rigolet phase (Lasalle et al., 2014).

Interpretation of microstructures and phase equilibria modelling has constrained the *P–T* conditions of the thermal peak at 9–10 kb /~850°C, with moderate d*P*/d*T* gradient *P–T* paths in the mid-*P* belt and 15–16 kb / ~850–900°C, with steeper d*P*/d*T* gradient *P–T* paths in the high-*P* belt (Indares et al., 2008, Lasalle and Indares, 2014, Patrick and Indares, 2017).

These *P–T* patterns are consistent with the numerical models of the Grenville orogeny developed by Jamieson et al. (2010) and Jamieson and Beaumont (2011) as follows: the *P–T* paths with steep dP/dT gradients facilitate the exhumation of deep rocks in the orogenic flanks, while the *P–T* paths with moderate d*P*/d*T* gradients are representative of extended lateral transport of ductile crust under an orogenic plateau.

1.3.4. Field relations in the PLV

This study focuses on metapelites and their potential anatectic equivalents in the PLV. The PLV is a metasedimentary sequence dominated by metapelite and metagreywacke, with subordinate quartzite and scarce calcsilicate rocks (Moukhsil et al., 2012), which is exposed over a large area south of the Manicouagan reservoir in the mid-*P* belt (Fig. 1.2). Metapelites are variably migmatized and are arranged as layers/rafts intermingled with leucocratic layers/domains potentially representing (in part at least) leucosome (Fig. 1.5a,b). Some of these leucocratic layers have sharp boundaries, are a few tens of centimeters thick and may represent channels through which melt once migrated. In addition, scarce metric-scale outcrops of biotite–

garnet-bearing foliated granite have been observed, but their contacts with the supracrustal rocks were not exposed (Fig. 1.5.c). The presence of garnet and biotite suggests that these rocks may be anatectic. These rocks will be referred to as PLV granites.

1.4 General approach

The main objective of this thesis is to investigate the melt productivity of metapelites from the metasedimentary sequence PLV of the mid-*P* belt using phase equilibria modelling of characteristic samples, and to compare the compositions of modelled melts with those of discrete leucocratic layers associated with the metapelites, and those of the PLV granites. The results are also compared with melt compositions calculated using other aluminous rocks from the wider area: hydrothermally altered rocks (HAF), from the mid-*P* belt, and aluminous rocks of uncertain origin from the southern part of the high-*P* belt.

The PLV samples of metapelite come from two locations, referred to here as PLV1 and PLV2 (Fig. 1.2). Metapelites of the PLV have been previously studied in PLV1, with one sample - HJ60- modelled by Lasalle and Indares (2014) and Kendrick and Indares (2018) for *P–T* determinations. In the context of the present study, supplementary samples from PLV1 were investigated, covering a wider composition range, as well as samples of metapelite from PLV2, leucocratic layers and samples of PLV granite from both locations.

The foundational component of this research involved documentation of microstructures in these new samples, geochemical characterization of leucocratic layers and of PLV granites, and phase equilibria modelling of the metapelites using THERMOCALC (e.g Powell and Holland, 2010) to infer *P–T* paths and set the framework for melt calculations. PLV2 has been interpreted to have experienced *P–T* conditions similar to the rest of the mid-*P* belt (Indares, 2020), and this hypothesis will be tested here.

Comparing the PLV granites with modelled anatectic melts implies that the age of the former is broadly the same as the age of metamorphism of the aluminous rocks. The age of metamorphism is well established in the aluminous rocks of the PLV, the HAF, and the high-*P* belt. However, the age of PLV granites, presumed to have formed by anatexis is unknown. Therefore, a second component of this research, was to date the crystallization age of these granites using U–Pb on monazite.

Finally, the last component of the research involved calculation of melt compositions expected to be produced by the aluminous rocks, and comparisons with the compositions of the presumably anatectic PLV granites from the mid-*P* belt. Melt compositions and proportions were modelled using THERMOCALC simulating closed systems, where the generated melt remains in the rock and continues to equilibrate with the residue along the *P–T* path, and open systems, where as the melt is produced, a portion of it migrates from out of the rock. The different melt compositions were compared using standard geochemical classification diagrams.

1.5 Thesis Organization

The first chapter provided the introduction and background of the thesis; it covered basic concepts on the anatexis of aluminous rocks, key features of the Grenville Province and on the local geological context, and the general approach. Chapter two describes the methodology and analytical techniques used. The next three chapters cover the main components of the thesis: petrography (Chapter 3), geochemistry and geochronology (Chapter 4); and phase equilibria modelling (Chapter 5), with each one presenting results and discussion on key points. Finally, chapter 6 summarises, and integrates the different outcomes of this work, and provides concluding remarks.

Figures Chapter 1

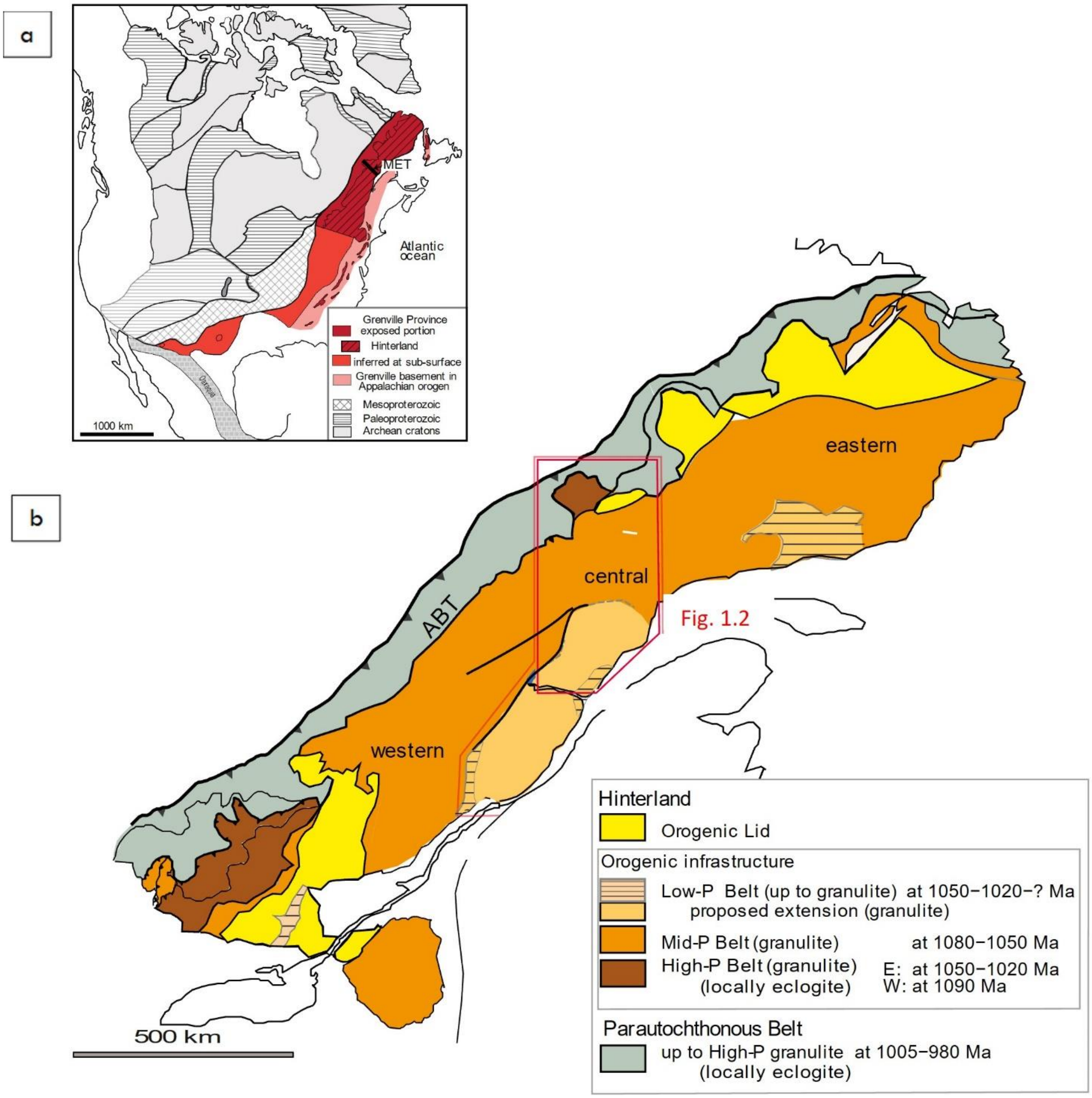

Figure 1.1 a) Extension of the Grenville Province along the east coast of North America. b) Tectono-metamorphic divisions of the Grenville Province. Red box represents the location of Fig 1.2. ABT: allochthon Boundary Thrust (modified from Indares, 2020).

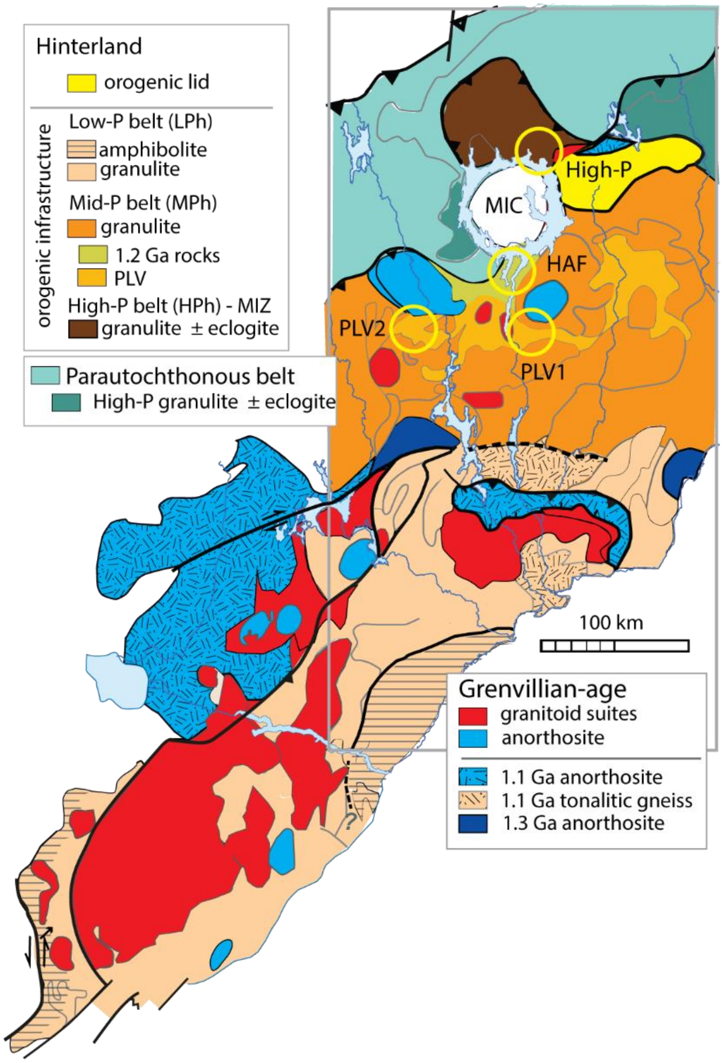

Figure 1.2 Location of the investigated aluminous rocks in the central Grenville Province: PLV1 and PLV2 metapelites, hydrothermally altered felsic rocks (HAF) and high-*P* aluminous rocks; MIC: Manicouagan Impact Crater (modified from Indares, 2020).

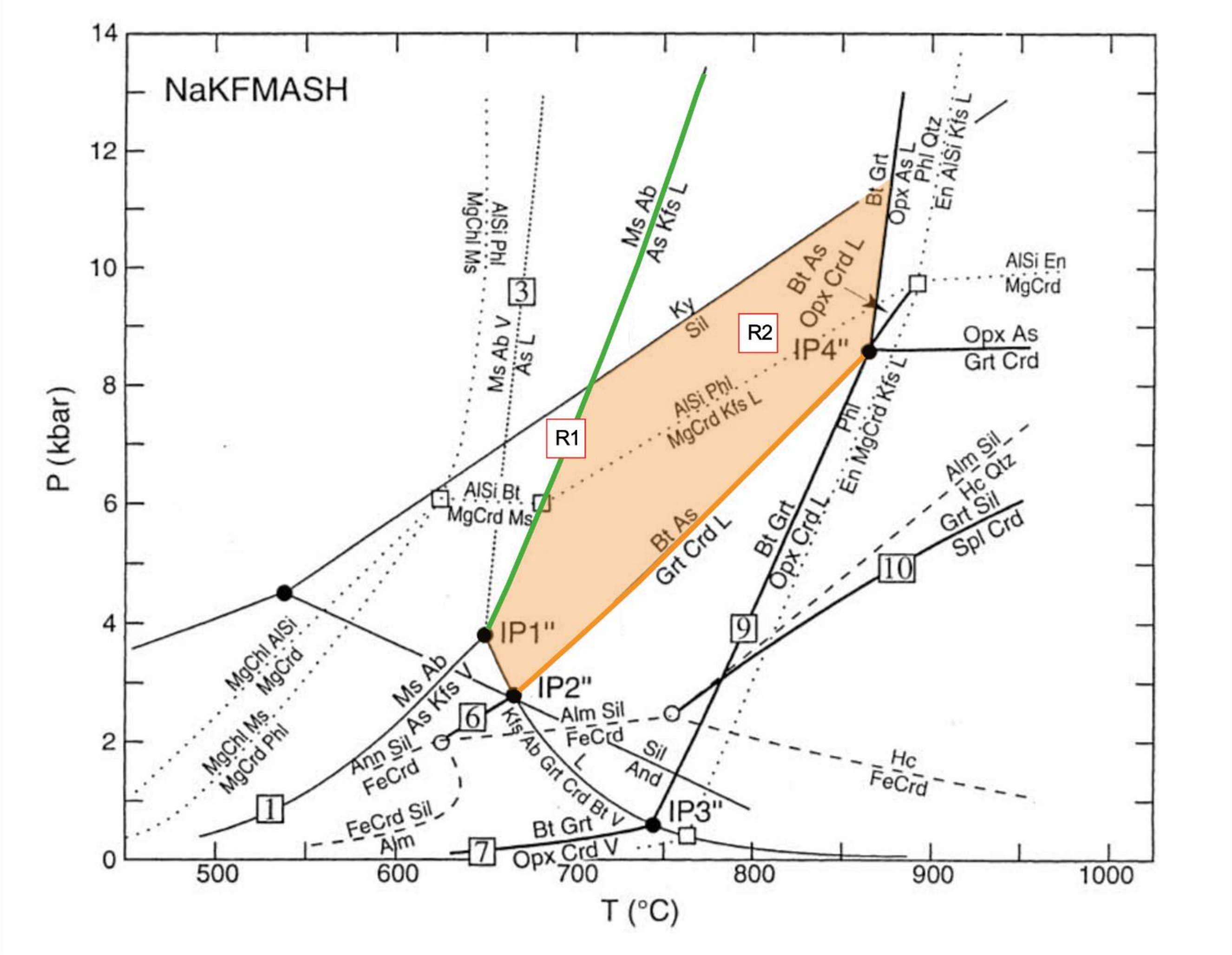

Figure 1.3 Petrogenetic grid for the NaKFMASH system of a typical metapelite showing key melting reaction at upper amphibolite to granulite-facies conditions. Dashed lines: KFASH system; dotted lines: KMASH system. Shaded field: *P*–*T* field of continuous reaction Bt+Sil+Qtz= Grt (or crd)+/-Kfs+L (R2) (modified from Spear et al., 1999).

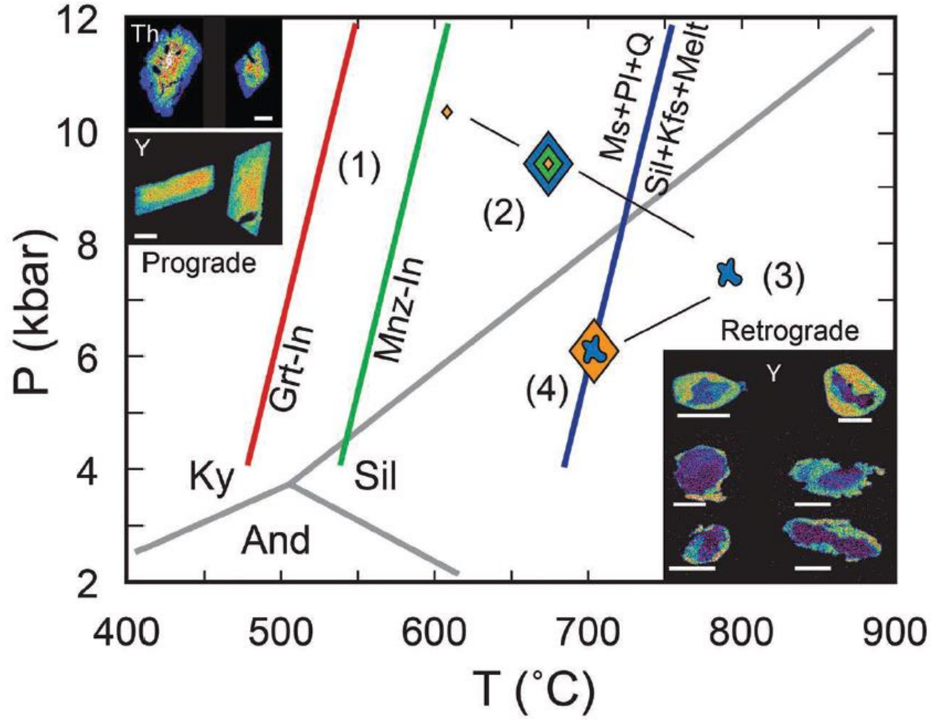

Figure 1.4 Schematic Th and Y chemical progress of monazite related to garnet growth and partial melting (from Kohn, 2016).

Figure 1.5. a, b) Anatectic metapelite in PLV showing aluminous layers and rafts in leucocratic Domains. The leucocratic domains locally form discrete layers. c) foliated, garnet–biotite-bearing granite in PLV.

2 CHAPTER 2: Methodology and Analytical Techniques

This work explores the melt productivity of aluminous anatectic rocks from the central Grenville Province, with special focus on those from the Plus Value Complex (PLV) of the mid-*P* belt, as well as links between melt presumably produced by and migrated from these rocks and exposed granite of potentially anatectic origin (PLV granites). This involves documentation of microstructures of the aluminous rocks, of associated leucocratic layers and of the PLV granites; determination of ages and chemical characteristics of the latter; and modelling of melt compositions produced by the aluminous rocks.

Microstructures and mineral assemblages of the different rock types were documented by detailed petrography using optical microscopy and SEM–MLA false color mineral maps of polished thin sections. Thin sections of aluminous rocks covered a wide range of proportions and relations between restite and leucosome, and special attention was placed in decoding microstructural evidence for anatexis in these rocks. The geochemistry of leucocratic layers and of the PLV granites was determined by traditional bulk rock analyses. In addition, crystallization ages of the PLV granites were determined by U–Pb dating of monazite, following documentation of monazite morphologies and chemical zoning. Finally, to link the compositions of the granites and the presumed lost melt generated by the aluminous rocks, metamorphic *P–T* conditions were inferred, and melt compositions were calculated using THERMOCALC (Holland and Powell, 1998).

2.1 Petrography

Thirty-five samples of aluminous gneisses, leucocratic layers (interpreted to be leucosome) and granites were documented in the context of this study (Table 2.1). The hand specimens were classified macroscopically, in terms of general appearance, and mineralogy. Then polished thin sections were examined with an optical microscope to document mineral assemblages and microstructures.

2.1.1 SEM–MLA imaging

Sixteen thin sections (seven of aluminous rocks samples, two of leucocratic layers and three of PLV granites) were selected for imaging with the FEI Quanta 400 scanning electron microscope (SEM), located in the Core Science Building at Memorial University of Newfoundland. The analytical conditions used were an acceleration voltage of 25kV and a current of 10nA. The SEM is equipped with mineral liberation analysis (MLA) software (JKTech, University of Queensland, Australia), which generates false-color mineral maps by defining mineral boundaries and matching the composition of the grains with a mineralogical database, thus identifying each mineral and giving each mineral a different colour. At the same time back-scatter electrons (BSE) maps are acquired. This method allows one to image microstructures and distribution of minerals at the thin section scale and also calculates the modal proportions of the minerals present.

Two different SEM–MLA modes were used for imaging the samples depending on the complexity of the mineralogy and microstructures. The regular mode (1) operates with a resolution of 500 pixels per frame, X-ray step size of 10 pixels and a BSE image scan time of 16 μs, whereas the fast method (2) consists of 400 pixels per frame, 16 pixels and 8 μs. The mode used for every sample is listed in Table 2.1.

2.1.2 Mineral chemistry

The mineral chemistry of garnet, plagioclase, k-feldspar and biotite of 7 samples (Table 2.1) was determined using a JEOL JXA-8230 Electron Probe Microanalyzer (EPMA) with five wavelength dispersive spectrometers (WDS) at Memorial University of Newfoundland.

For all the minerals a voltage of 15kV and a current of 20nA were used. Garnet was analyzed for Mn, Ca, Al, Si, Mg, Fe and Ti along transects across the largest grains with a beam of 1 micron. Feldspars were analyzed for K, Ca, Na, Al, Si and Fe, with a beam of 1 micron, in cores and rims for larger grains, and core for smaller grains. Finally, biotite was analyzed for F, Cl, K, Al, Si, Mg, Fe and Ti with a beam of 5 microns, in cores and rims, (or only cores of small grains). For each analyzed mineral, the standards used for the calibration of each element as well as the secondary standards and the spectrometers used for the analysis are listed in Table 2.2.

Additionally, X-ray chemical maps of Ca, Fe, Mg and Mn in garnet from one sample (HJ-60c, PLV1) were produced to assess zoning.

2.2 U-Pb Monazite Dating

U–Pb monazite dating was undertaken in the PLV granites (samples 12-AI-15 and 12-AI-20 from PLV1, and 11-AI-448 from PLV2), to compare with the monazite ages published for the PLV metapelites, and other aluminous rocks from the wider area. Monazite was identified in the thin sections of 12-AI-15, 12-AI-20, where its distribution was imaged in the SEM–MLA maps and was dated in situ. In contrast, no monazite was observed in the thin sections of 11-AI-448. Therefore, this sample was broken into small fragments and pulverized later to separate the minerals using heavy liquids. After this was done, the Frantz Isodynamic Magnetic Separator was used to separate minerals based on their magnetic properties. The resulting material was composed of garnet, zircon, titanite and monazite. Monazite was picked by hand using a binocular microscope afterwards.

X-ray maps of Th, Nd, Pb, Y and U were generated for the largest monazite grains of the 3 samples (four from sample 12-AI-15, seven from sample 12-AI-20 and fourteen from sample 11-AI-448) with the EMPA to assess the internal structure and guide the locations for dating spots (core and rim).

Next, monazite was dated using Laser Ablation ICP Mass Spectrometry (LA–ICP–MS) in the Bruneau Innovation Center at Memorial University of Newfoundland. The LA–ICP–MS measurements were done on a 193ArF Excimer Laser, GeoLas (Coherent, Germany) and an Element XR, Thermo Fisher (Germany). A crater size of 20um, a laser repetition rate of 3 Hz, an energy density of 2 J/cm2 and a carrier gas flow of 1 L/min Helium were used. The ICP–MS was tuned to high sensitivity and a ThO+/Th+ (Thorium oxide) ratio of less than 0.3%. Each analysis consisted of 30 sec background acquisition followed by 40 sec ablation. The isotopes 202Hg, 204Pb, 206Pb, 207Pb, 208Pb, 232Th, 235U and 238U were measured. The iolite software was used for data processing with the STK monazite as primary standard and KMO3-72 and Trebilcock as quality control standards. Further details on this technique can be found in Lasalle et al. (2014).

2.3 Phase Equilibria Modelling

P–T pseudosections for metapelite samples HJ-60c from the PLV1, and 12-AI-10Y from the PLV2 were calculated to assess the *P–T* stability fields of the observed mineral assemblages, infer *P–T* paths and eventually compute melt proportions and melt compositions. Additionally, *P–T* pseudosections for hydrothermally altered felsic rocks or HAF (216c, 333x) of the mid-*P* belt, and aluminous rocks from the high-*P* belt (244 and 320) were reproduced from the literature, for melt calculations (Lasalle and Indares, 2014; Indares et al., 2008).

Phase equilibria modelling was done in the NCKFMASHTO system with THERMOCALC version 3.33 (updated from Powell & Holland, 1988) along with the thermodynamic database tcds55 (Holland & Powell, 1998; updated in 2003, and activity models by White et al., 2007; Coggon and Holland, 2002; and Holland and Powell, 2003). This is an older dataset, but it is the most accurate so far for aluminous anatectic rocks. As stated in Kendrick and Indares (2018a), *P–T* pseudosections calculated with the new database tcds62 (updated from Holland & Powell, 2011) in the MnNCKFMASHTO system restricts unrealistically the stability field of the biotite dehydration melting reaction for kyanite-bearing rocks. This problem may be due to the lack of data for fluorine in the models since fluorine stabilizes biotite to higher temperatures (as cited in Kendrick and Indares, 2018a; White et al., 2014b).

2.3.1 Bulk rock compositions

P–T pseudosections are calculated for specific bulk rock compositions. The bulk compositions of the samples for which *P–T* pseudosections were calculated here for the first time (PLV1 and PLV2 metapelites HJ-60c, and 12-AI-10Y), were determined from the proportions of minerals (in area %) obtained by SEM–MLA and the mineral compositions (for those of solid solutions, acquired by EPMA). This procedure consists of the following steps: (a) the molar volume of each phase was calculated based on the average proportion for every phase component in a given phase. (b) the mode % of each phase was divided by the molar volume to obtain the number of moles of the phase of interest; (c) this value was then divided by the sum of the total number of moles of all the phases present and multiplied by 100 to get the mol % of the phases; (d) the mol% of each phase component, was calculated by multiplying the mol% of the phase by the average proportion; (e) the moles of the constituent oxides was calculated multiplying the mol% of the phase component by the number of moles of the oxide in the structural formula~~.~~ After that, the mol% of each phase component was multiplied by the number of moles of each oxide in their respective structural formula in order to calculate the total amount of moles of each oxide in each phase; (f) the results for each oxide were summed up and then normalized to obtain the mol% of the oxides, the bulk composition in mol %. The bulk compositions of the HAF and the aluminous rocks of the high-*P* belt, were previously calculated by Lasalle and Indares (2014), and Kendrick and Indares (2018) using the same procedure described above.

For the model system used (NCKFMASHTO), in addition to the oxides, a value of O has to be set apart of the bulk composition. This is used by THERMOCALC to convert a certain amount of Fe into Fe^{3+}. The value of O used in the calculations was 0.1, based on the absence of Fe^{3+} bearing oxides

2.3.2 P–T pseudosections and melt calculations

THERMOCALC calculates boundaries of the stability fields of minerals as function of pressure and temperature. It also allows one to determine compositions and proportions of phases (in this case minerals and melt) at any *P–T* point. Phase equilibria modelling was carried out to calculate *P–T* pseudosections delineating the stability fields of mineral assemblages for specific bulk compositions of aluminous samples. In these fields was also added the distribution of selected mineral proportion and mineral composition isopleths. These *P–T* pseudosections provided the framework for: (a) the interpretation of mineral chemistry and microstructures of aluminous samples in terms of *P–T* paths; and (b) to calculate melt compositions and melt proportions at selected *P–T* conditions, to assess changes in melt composition with progress of anatexis, and the potential composition and amount of melt loss during prograde metamorphism.

2.4 Granite Compositions and Geochemical Classification Diagrams

Modelled melt compositions produced by the PLV metapelites, HJ-60C and 12-AI-10Y were compared with the bulk compositions of the PLV granite and leucocratic layers (interpreted to be leucosome) from the same area, along with calculated melt compositions from the HAF from the mid-*P*, 216c and 333x, and metapelites from the high-*P*, 244 and 320 (from Lasalle and Indares, 2014, and Kendrick and Indares, 2018a). The major element bulk compositions of the granite and leucocratic layers were determined by X-ray fluorescence (XRF) in the ACTLABS laboratory

The calculated melt compositions, the residuum, and the bulk compositions from the granites and aluminous rocks were plotted using IGPET, in K_2O vs. Na_2O (wt%) binary diagrams, $FeO + MgO$ -Na_2O + CaO - K_2O (mol%) ternary diagrams, and QAP ternary diagrams, the later for the names of the granite rocks and calculated melts. These diagrams were used to assess the evolution of the melts at different *P–T* conditions, and also to compare the results with the work done by Pavan et al. (2021). In addition, these results were plotted in Shand's index diagrams to assess their aluminosity.

Table 2.1

Analytical techniques used in the samples from the PLV1 and PLV2.

Area	Sample	Group	SEM-MLA MODE	Mineral Chemistry	Monazite Dating
PLV1	HJ-60c	A	1	x	
	HJ-60d	A	2		
	HJ-60d1	A			
	HJ-60e	A			
	HJ-60f	A			
	HJ-60h	A			
	HJ-80	A			
	HJ-85	A			
	HJ-88	A			
	HJ-88d1	A			
	HJ-88d2	A	1	x	
	08-60-1	Q	2		
	08-60-2	Q	2		
	08-60-3	Q	2		
	08-60a-1	A	2		
	08-60a-2	A	2		
	08-60a-3	Q	2		
	08-65-A	Q*	1	x	
	08-65-A1	Q*			
	08-66	A			
	08-67-1	Q*	2		
	08-67-2	Q*			
	08-67-3	Q*			
	11-448	G	1		x
PLV2	12-AI-10a	A			
	12-AI-10e	A	1		
	12-AI-10e1	A			
	12-AI-10e2	A			
	12-AI-10f	A	1		
	12-AI-10y	A	1	x	
	12-AI-10z	A			
	12-AI-15	G		x	x
	12-AI-20	G		x	x
	12-AI-46b	A			
	12-AI-49	A	1	x	
	12-AI-49b	A			

Note: A, aluminous rock; Q, quartzofeldspathic rock; Q* quartzofeldspathic rock interpreted to represent leucosome; G, granite. SEM–MLA mode 1: regular; SEM–MLA mode 2: fast.

Table 2.2

Standards used for minerals analyzed with the electron probe micro-analyzer (EPMA)

Standards											
Garnet				**Biotite**				**Feldspar**			
Number of Oxygens: 12				Number of Oxygens: 22				Number of Oxygens: 8			
Primary Standards				**Primary Standards**				**Primary Standards**			
Element	Standard	Crystal	CH	Element	Standard	Crystal	CH	Element	Standard	Crystal	CH
Mn	Rhodenite	LIFL	2	F	JMH_fluorapatite_319	LDE1	1	K	Orthoclase	PETL	3
Ca	Diopside	PETL	3	Cl	Tugtupite	PETL	3	Ca	Diopside	PETL	3
Al	Almandine	TAP	4	K	Orthoclase	PETL	3	Na	Albite	TAP	4
Si	Almandine	TAP	4	Al	pyrope	TAP	4	Al	Almandine	TAP	4
Mg	Olivine	TAP	4	Si	Diopside	TAP	4	Si	Orthoclase	TAP	4
Fe	Almandine	LIFH	5	Mg	pyrope	TAP	4	Fe	Almandine	LIFH	5
Ti	rutile	LIFH	5	Fe	Almandine	LIFH	5				
				Ti	rutile	LIFH	5				
Secondary Standard				**Secondary Standard**				**Secondary Standard**			
Astimex pyrope				Stimex biotite				Astimex plag			

3 CHAPTER 3: Petrography and Mineral Chemistry

3.1 Petrography

The examined samples are from metapelites of the PLV, from leucocratic layers associated with them at the outcrop scale and from the PLV granites (for example, see Fig. 1.5). A subset of representative samples was selected for detailed petrography by optical microscopy and SEM–MLA imaging (36 and 18 polished thin sections respectively). This was done to determine mineral assemblages, document microstructures and, for the metapelites, assess petrographic evidence of partial melting. The full list of thin sections and observed assemblages is in Appendix A1, and a detailed petrographic description of each thin section is in Appendix A2. Mineral proportions in thin sections that were analyzed by SEM–MLA are listed in Table 3.1.

3.1.1 Mineralogy and microstructures

3.1.1.1 PLV Metapelites

The metapelites of the PLV are layered at the scale of one to a few tens of centimeters. They consist of garnet–sillimanite–biotite-rich layers or elongated rafts (referred to herein as aluminous and inferred to represent a mixture of residue and leucosome), finely interlayered at a centimetric scale with layers dominated by feldspars and quartz, the more leucocratic and coarse-grained of which are presumed to represent leucosome. The layering is variably disrupted by leucosome (Fig. 3.1a) and occasionally it is diffuse (Fig 3.1b). Locally, the rocks also exhibit variations in grain size (Fig. 3.2a and Appendix A3), and the finer-grained quartzofeldspathic layers are interpreted to represent more quartzofeldspathic portions of the protolith that did not go through partial melting. These layers will not be considered further.

Based on the arrangement between the aluminous layers and leucosome, the metapelites are categorised as metatexite locally ranging to diatexite, following the classification of Sawyer (2008). The arrangement and varied proportions of aluminous and leucocratic domains are also captured by the examined thin sections.

The main mineral assemblage in these rocks consists of garnet, sillimanite, biotite, K-feldspar, plagioclase, and quartz. Zircon, monazite, ilmenite, and pyrite are present as minor phases (Table 3.1). Some samples contain texturally late chlorite, muscovite, sericite, and carbonates. Generally, these rocks show a variably interconnected network of biotite and sillimanite defining the foliation and garnet, intertwined with leucocratic pods or layers of quartz, K-feldspar, plagioclase, and biotite (Figs. 3.2, 3.3).

Garnet ranges from porphyroblasts that are sub-rounded or elongate within the foliation, to smaller subhedral grains. It generally contains inclusions of sillimanite, biotite, quartz, and feldspar, as well as polymineralic inclusions and embayments. These commonly consist of resorbed quartz in a pool of feldspar (Fig. 3.4a, b, c). Some garnet rims are replaced by biotite and sillimanite clusters (Fig. 3.4d). In most the cases, the smaller garnet grains are inclusion-free and are sporadically located near or within the quartzofeldspathic domains.

Sillimanite, besides being present as an inclusion in garnet, occurs as prismatic crystals forming elongate clusters parallel to and defining the foliation, commonly with biotite in garnet replacement sites (Fig 3.4d). In samples, HJ-60h, HJ-88, HJ-88d1, HJ-88d2, some sillimanite grains are completely replaced by a very fine flaky material (pinite/sericite). *Kyanite* occurs as a minor phase in some samples of PLV1 (see Appendix A1). It is present as resorbed crystals, breaking down to sillimanite or completely pseudomorphed by it, and generally surrounded by felsic pools or films (Fig 3.4e). *Biotite* occurs as single laths or clusters along the foliation, commonly with sillimanite. It is also present as smaller interstitial flakes in the quartzofeldspathic domains and surrounding garnet. Some biotite is replaced by chlorite.

Quartz, plagioclase and K-feldspar are mainly concentrated in specific layers/domains (Fig. 3.3), some of which have coarser grain size. Quartz and K-feldspar are more abundant than plagioclase in most samples. K-feldspar is mostly perthitic (Fig. 3.4f). In addition, quartz, and feldspars occupy embayments in garnet, where they define finer microstructures including felsic pools with relict quartz and interstitial films (Fig. 3.4b, 3.5a, b). These are found inside garnet and surrounding sillimanite or kyanite, and biotite. The interstitial films are preferentially located at garnet grain boundaries against resorbed quartz. They are also observed pervasively inside biotite and addition, quartz is locally intergrown with biotite (Fig. 3.5c).

3.1.1.2 Leucocratic layers

This section focuses on a few tens of centimeters-thick, discrete quartzofeldspathic layers associated with the metapelites in PLV, and which may represent channels through which melt might have migrated. These rocks consist of K-feldspar, plagioclase, and quartz, with minor garnet, biotite, and sillimanite (Fig. 3.6a,b). *Sillimanite* is generally present only as acicular inclusions in garnet, except for sample 08-67-1, where it also occurs as prismatic crystals surrounding some garnet grains (Figs. 3.6b, 3.7a). *Garnet* is present as embayed and resorbed grains with inclusions of quartz and feldspar within felsic pools (Fig. 3.7b) and also as small, inclusion-free subhedral to anhedral grains that may represent tips of larger crystals. *Biotite* occurs as individual flakes or forms clusters elongate to and defining the foliation. K-feldspar is mostly perthitic. In addition, in one of the leucocratic layers (08-65-A) chlorite locally replaces biotite and garnet, whereas muscovite (randomly oriented) replaces feldspars (Fig. 3.6a).

3.1.1.3 PLV Granites

The granites are composed of varied proportions of K-feldspar, plagioclase and quartz with minor biotite and garnet (up to 5% mode), and trace muscovite, monazite, zircon and opaques (Fig. 3.6c,d,e). *Garnet* occurs as xenomorphic grains of variable sizes. In some samples, it is partly rimmed by biotite and has inclusions (or embayments?) of quartz, feldspar and opaques (Fig 3.7d). *Biotite* is present as clusters, occasionally around garnet and as interstitial individual flakes in the groundmass. *Quartz, plagioclase* and K-*feldspar* show a relatively homogeneous distribution and grain size, and K-feldspar is perthitic. Quartz and feldspar form intergrowth textures and rims around resorbed biotite (Fig 3.7e), and K-feldspar locally forms grains interstitial to other phases in the PLV1 granite (Fig 3.7f,g).

3.1.2 Insights from the mineralogy and microstructures

3.1.2.1 Evidence for partial melting

The main mineral assemblage of the aluminous layers of the PLV metapelites, quartz, garnet, K-feldspar, plagioclase, biotite, and Al-silicate (Table 3.1, Fig. 3.3) is consistent with the biotite dehydration melting reaction:

$$Bt + Als + \ Qtz \ \pm Pl = Grt + Kfs + \ melt$$

([R2] in Fig. 1.3).

This reaction occurs continuously over a range of temperatures above the muscovite stability field, at granulite-facies conditions (Spear et al., 1999). Furthermore, there is evidence of former melt in a range of microstructural settings according to criteria set by Holness and Sawyer (2008), Holness (2008), Sawyer (2001) and Vernon (2011), the felsic pools and films enclosing resorbed quartz that are observed as inclusions and embayments in garnet (Fig 3.4a,b,c), are interpreted to represent former melt trapped inside garnet that grew peritectically by reaction R2. These are also found surrounding sillimanite, kyanite and biotite (Fig 3.4e).

Clusters of biotite, commonly with sillimanite, overgrowing garnet rims are consistent with reaction R2 in the reverse sense, during melt crystallization (Fig. 3.4a) (Sawyer, 1999, Jones and Brown, 1990, Vernon, 2011). In fact, concentration of biotite in garnet resorption sites, and the presence of biotite elsewhere as small interstitial grains suggests that a large portion of this mineral grew during melt crystallization. However, the peak mineral assemblage is generally well preserved, suggesting that part of the produced anatectic melt has migrated away from its source, and that only a limited amount remained to produce back retrograde biotite and aluminum silicate during cooling. Melt loss is commonly documented in granulite-facies rocks metamorphosed in dynamic environments (White and Powell, 2002).

3.1.2.2 Petrological link between the aluminous layers, leucocratic layers, and the PLV granites

The leucocratic samples and the granite samples have broadly a granite mineralogy, even though they have varied quartz and feldspars proportions (Table 3.1, Fig. 3.6). In addition, they contain garnet, biotite, and sillimanite (the later in the leucocratic layers only), as do the metapelites, but in much smaller amounts (up to 5%). Therefore, a potential linkage between these rocks and the metapelites is suggested through a common protolith.

In the leucocratic rocks and the granites, there are two types of garnet: (a) variably resorbed grains, with former melt inclusions and associated with biotite and sillimanite as in the aluminous layers (Figs. 3.6b, 3.7a); and (b) xenomorphic and embayed garnet with discrete quartz and feldspar inclusions (Figs. 3.6a,c,d,e, 3.7b,c). The first type occurs in some leucosome layers, and could represent peritectic garnet formed by reaction [R2], entrained into the melt, and then partly replaced by biotite and sillimanite during melt crystallization. The second type of garnet mainly occurs in the granite samples and may have crystallized directly from the melt. Additionally, the chlorite (replacing biotite and garnet) and muscovite (replacing feldspars) found in some of the leucocratic samples (08-65-A) is consistent with a later hydration event.

3.2 Mineral Chemistry

The solid solution minerals, garnet, feldspars, and biotite were analyzed using EMPA to determine their chemical composition in seven samples: four aluminous (HJ60c and HJ-88d2 from PLV1, 12-AI-Y and 12-AI-49 from PLV2), one leucocratic (08-65-A) and two granitic (12-AI-20, 12-AI-15; see Appendix A4 and A5). Additionally, garnet X-ray chemical maps (Ca, Fe, Mg and Mn) from sample HJ-60C (PLV1) were generated to assess zoning patterns. Overall, the maps show a homogeneous composition with minor zoning (see Appendix A6) and will not be discussed further.

3.2.1 Garnet

Garnet was analyzed from core to rim along transects in the largest grains. It is predominantly homogenous, but some rims show a slight decrease in Ca, and those next to biotite have slightly higher Fe and lower Mg. In the aluminous layers, garnet is generally almandine rich (X_{Alm}~ 0.65), with moderate pyrope, and minor grossular and spessartine proportions (X_{Prp} ~0.31, X_{Grs} ~ 0.03, X_{Sps} ~ 0.01). The exception is sample 12-AI-10Y from PLV2, in which garnet has almost equivalent pyrope and almandine proportions (X_{Prp} ~0.46, X_{Alm} 0.50; Fig.3.8). Garnets in the leucocratic and granite samples are distinguished from those in the aluminous rocks, by higher almandine (X_{Alm} ~ 0.73), grossular (X_{Grs} 0.06) and spessartine (X_{Sps} 0.05) and lower pyrope (up to X_{Prp} 0.20; Fig. 3.8) proportions. No difference in the chemical composition in the two types of garnet from these rocks was detected.

3.2.2 Biotite

Biotite analyzed in the aluminous layers has generally higher X_{Mg} in the PLV2 sample relative to those of PLV1 (0.62–0.84 and 0.52–0.69 respectively), with the highest values in a biotite inclusion in garnet (sample 12-AI-10-Y, PLV2). In contrast, Ti ranges are similar in all samples (0.24 to 0.62 p.f.u) with the highest values in biotite farther away from garnet. For each sample, there is a clear trend of decreasing Ti with increasing $X_{Mg.}$ In most cases, analyzed grains located near garnet have higher X_{Mg} and lower Ti (Fig. 3.9) except for biotite in sample HJ-60C, where this trend is less prominent.

Al^{VI} in biotite is higher in the PLV1 samples (0.47–0.77) relative to those in PLV2 (0.25–0.47) (Fig. 3.9). In sample 12-10-Y there is a clear trend consisting of higher X_{Mg} with increasing Al^{VI}, with the highest values in grains close to garnet. In the other samples, the grains closest to garnet exhibit higher X_{Mg} but the Al^{VI} varies from grain to grain.

Biotite in the granite samples has lower X_{Mg} that in the aluminous layers (0.48 to 0.63). Ti contents vary from 0.29 to 0.57 p.f.u, with biotite following the same trend as most of the PLV aluminous layers, higher X_{Mg} and lower Ti contents when biotite is close to garnet. However, this trend is less pronounced compared to the aluminous rocks. Al^{VI} increases with X_{Mg}, but in sample 12-AI-15, the biotite grains closer to garnet display higher X_{Mg} and Al^{VI}. Due to the scarcity of biotite grains, biotite was not analyzed in the leucocratic sample 08-65-A

3.2.3 Feldspars

Plagioclase in the aluminous layers has uniform composition, with X_{An} ~ 0.28 in the PLV2 metapelites, and less calcic compositions in PLV1 samples (X_{An} ~ 0.18 in HJ-60c and up to ~0.23 in HJ-88D2; Fig. 3.9). The composition of K-feldspar varies from X_{Or} 0.77 to 0.93 (Fig. 3.10). However, in sample HJ-60c, some grains show lower X_{Or} values down to ~0.50, attributed to fine exsolutions of plagioclase in the grain. Plagioclase from the leucocratic layer 08-65-A, has the widest range and highest Na contents (X_{Ab} 0.99–0.76), whereas the granites show more calcic compositions (X_{An} 0.22–0.27). K-feldspar has a similar range for both, leucosome and granite samples, with X_{Or} ranging from 0.82–0.93 (Fig. 3.10).

3.2.4 Key points

The compositions and chemical trends of garnet, biotite and feldspars in the analyzed aluminous rocks from PLV1 and PLV2 are comparable, and the higher Mg contents in garnet and biotite from the PLV2 sample relative to the rest, are likely due to differences in the bulk Mg between these rocks. The overall homogeneity of garnet in the aluminous samples is interpreted to be the product of diffusion at high temperatures during an extended period of time and, potentially, during the early stages of cooling (Spear and Florence, 1992). The slight change in Fe and Mg at the rims of the garnet when in contact with biotite, is attributed to further Fe–Mg exchange between the two phases at their adjacent rims during cooling (Ferry and Spear, 1978). Therefore, the core compositions of garnets of the aluminous layers are inferred to represent *P–T* conditions the closest to the thermal peak. The higher amounts of Fe, Ca and Mn in garnets in the leucocratic and granite samples are generally consistent with more advanced resorption (for the garnets interpreted to have formed by R2 and entrained in the melt), or reflect a difference between the earlier, prograde peritectic garnet and garnet precipitating from melt (in the case of granite layers).

Ti *vs*. X_{Mg} trends in biotite of the aluminous layers are consistent with retrograde formation of biotite close to garnet, and with more efficient Fe–Mg exchange between the two minerals during cooling (Spear and Florence, 1992). In fact, as inferred by microstructures, large part of the biotite formed during melt crystallization. On the other hand, such trends are not as prominent in the granite layers, where there is less garnet in the rock and the presumably magmatic garnet is not particularly associated with biotite.

Mostly, the feldspars show a consistent composition range, overlapping in the PLV1, PLV2, and the PLV granites. However, in the leucocratic layer there is a wider range of X_{Ab}, and one sample from the PLV1, HJ-60C, also shows a broader range of X_{Or}, associated with the perthitic texture of the analyzed K-feldspars.

Figures Chapter 3

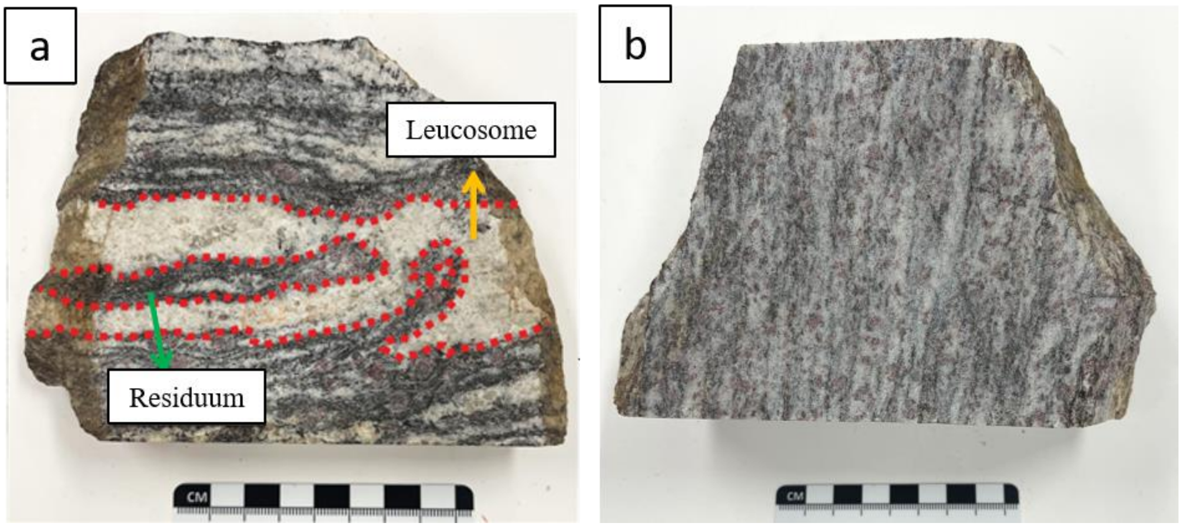

Figure 3.1. a) Metapelite from PLV1, with complex residuum-leucosome arrangement. The residuum consists of biotite, garnet and sillimanite and has a darker color, whereas the leucosome is composed of quartz, K-feldspar, and plagioclase. b) Metapelite from PLV2, showing diffuse layering.

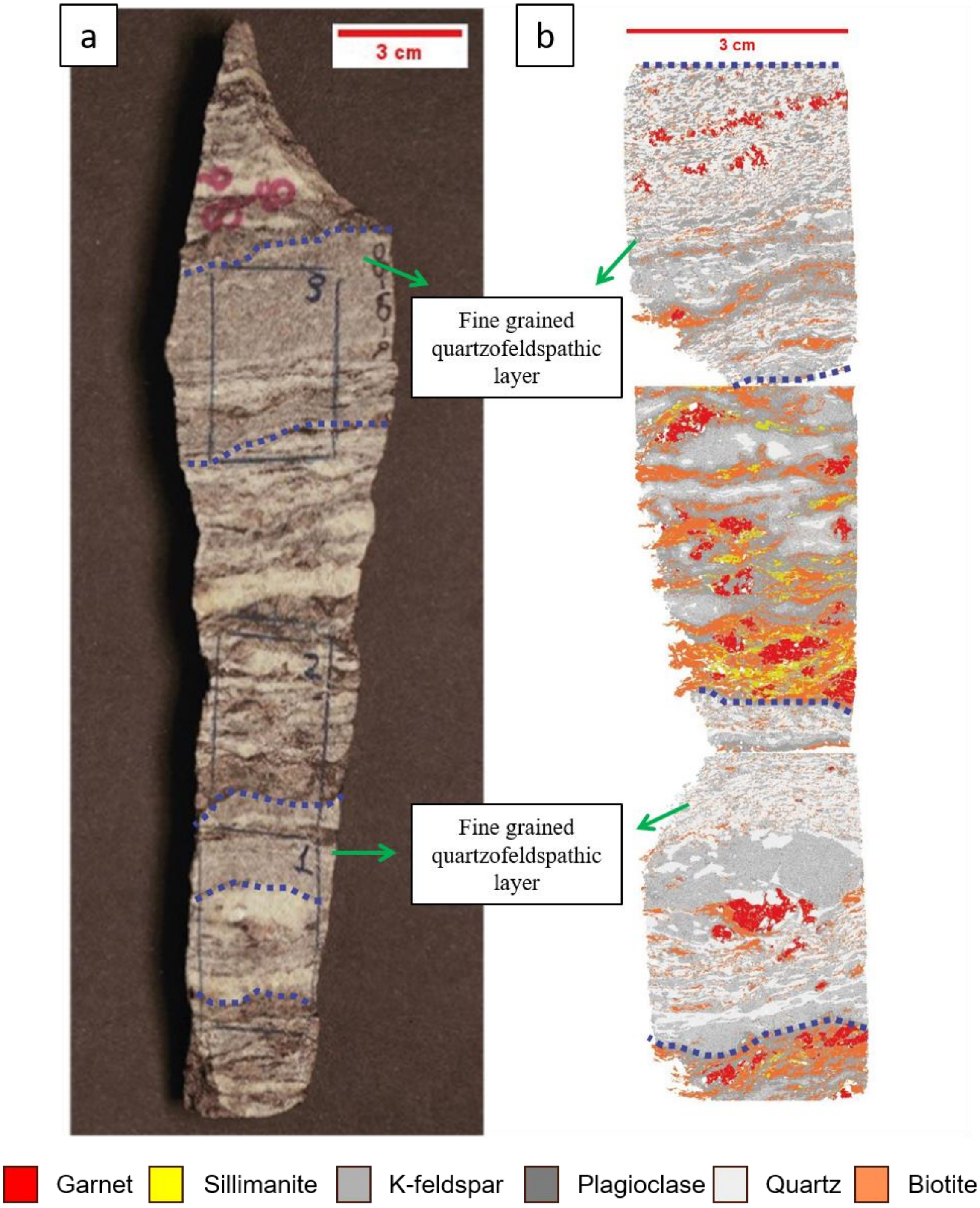

Fine grained quartzofeldspathic layer

Fine grained quartzofeldspathic layer

Figure 3.2. a) Slab 08-60a, from the PLV1, displaying varying proportions of aluminous and quartzofeldspathic layers/domains, along with variations in grain size. b) SEM–MLA maps of three thin sections cut from this slab.

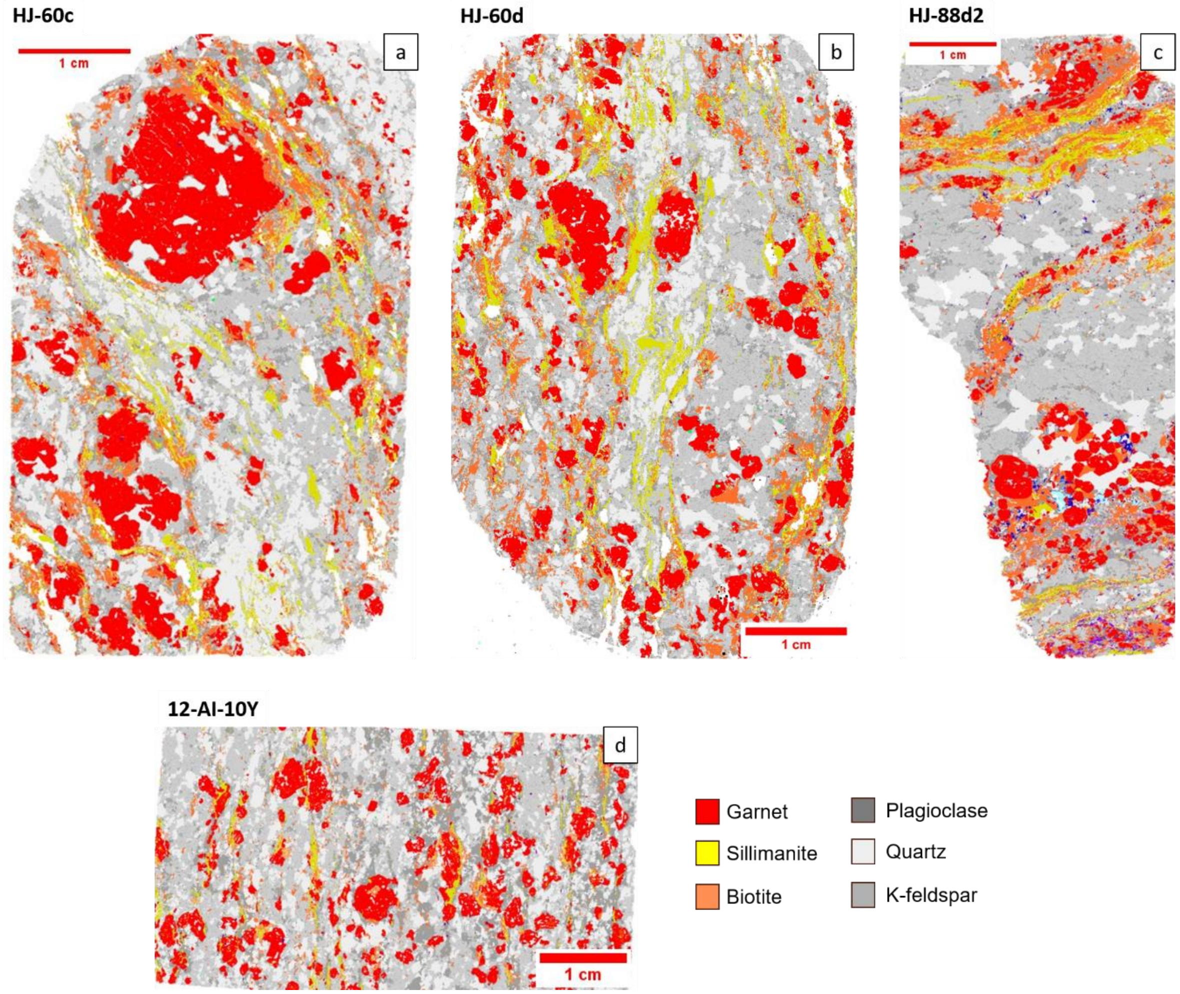

Figure 3.3. SEM–MLA false color mineral maps of three large thin sections from the PLV1, showing the range of relations between the different microstructural domains in this group, and one thin section from the PLV2.

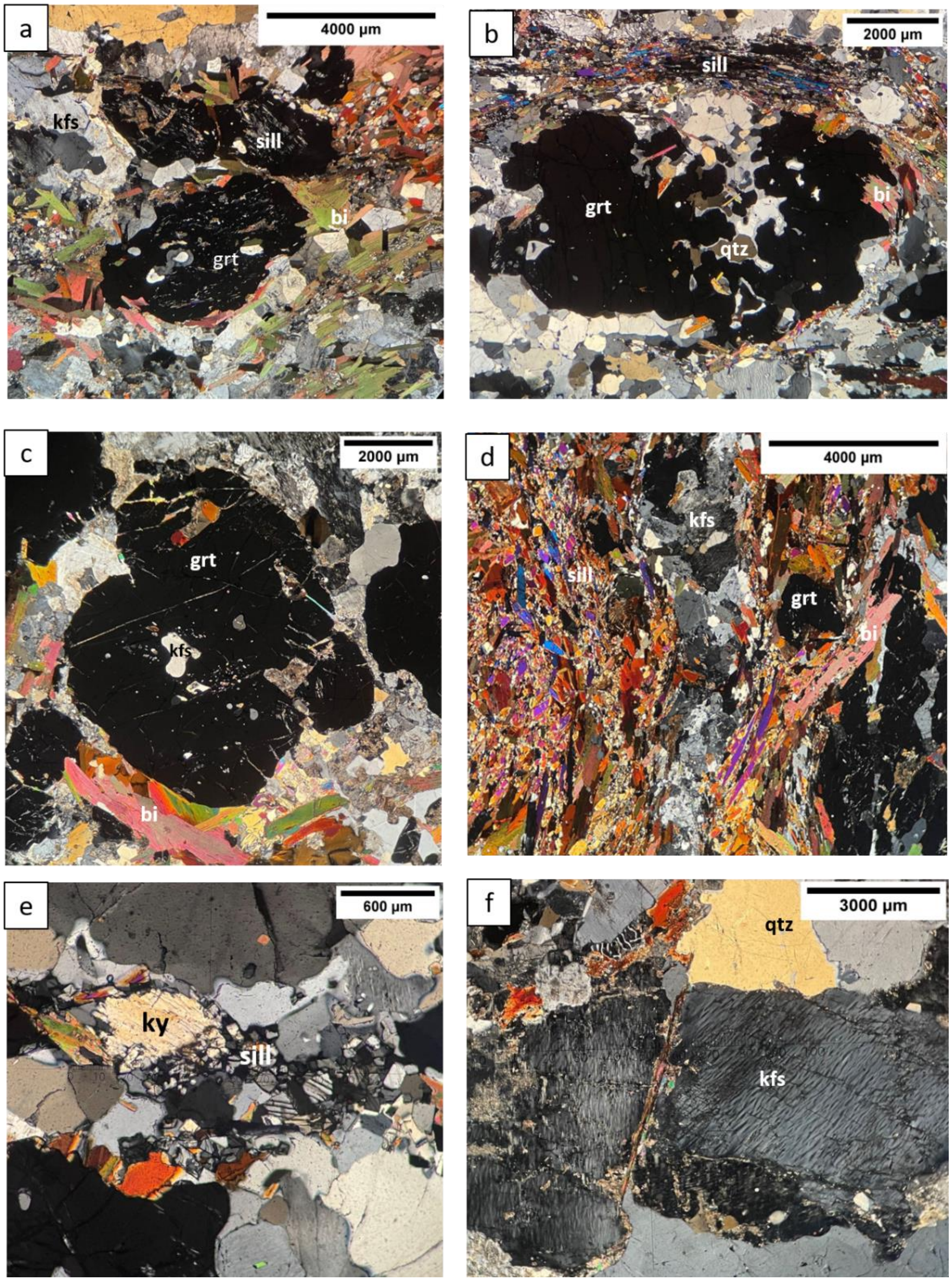

Figure 3.4 Photomicrographs of characteristic microstructures of the PLV1 metapelites (in XP). a) Elongated garnet with inclusions of fibrous sillimanite and felsic pools enclosing quartz. The garnets are surrounded by sillimanite and biotite clusters (HJ-60h) b) Garnet with embayments of felsic pools enclosing quartz; at the top layer of prismatic sillimanite (HJ-60d). c) Garnet with felsic pools (HJ-88d2). d) Layers composed of sillimanite, biotite, and garnet, enclosing a leucocratic domain of K-feldspar and quartz (HJ-88d2) e.) Kyanite breaking down to sillimanite (HJ-60d). f) K-feldspar showing perthitic texture (HJ-88d2).

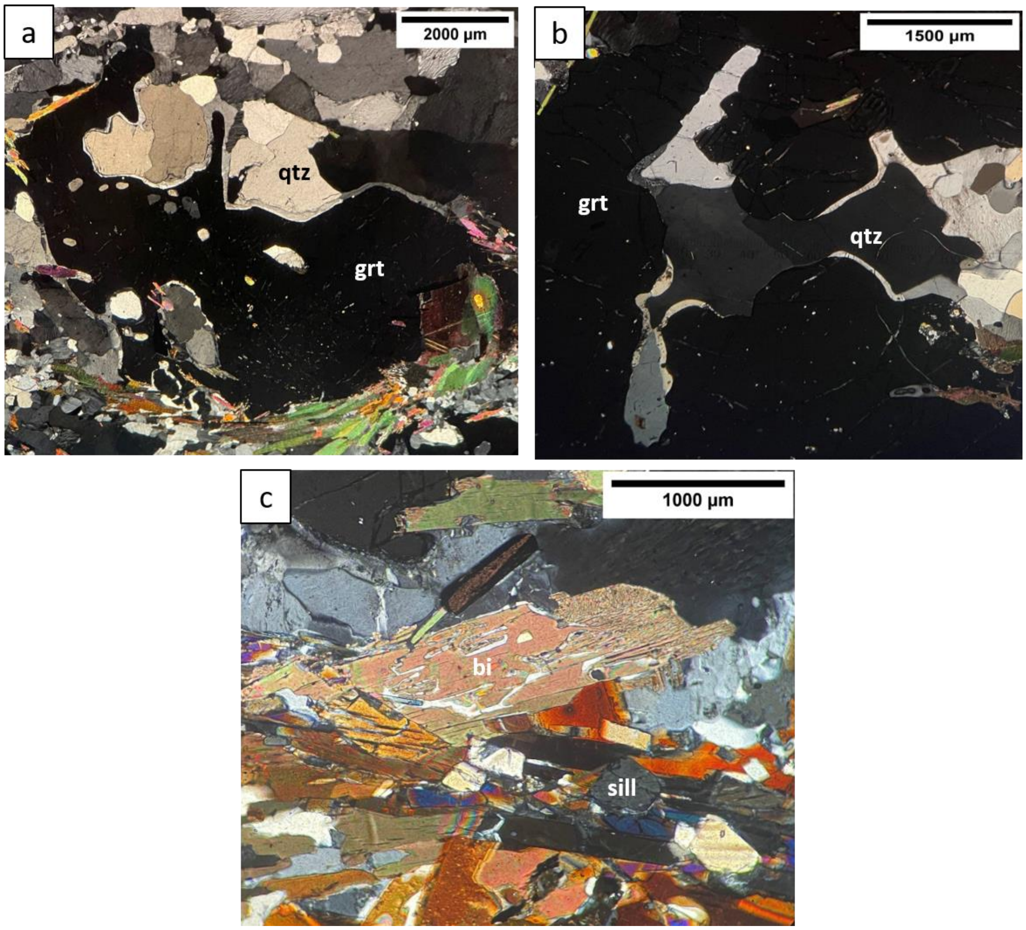

Figure 3.5 Photomicrographs of fine melt-related textures in the PLV metapelites (in XP). a) K-feldspar (plagioclase in certain places) films between garnet and quartz (08-60a-1). b) Detailed photo of plagioclase and K-feldspar films between garnet and resorbed quartz (HJ-60c). c) Quartz films within biotite grain, and intergrowth of biotite and quartz symplectite at the top right of the grain(HJ-88d2).

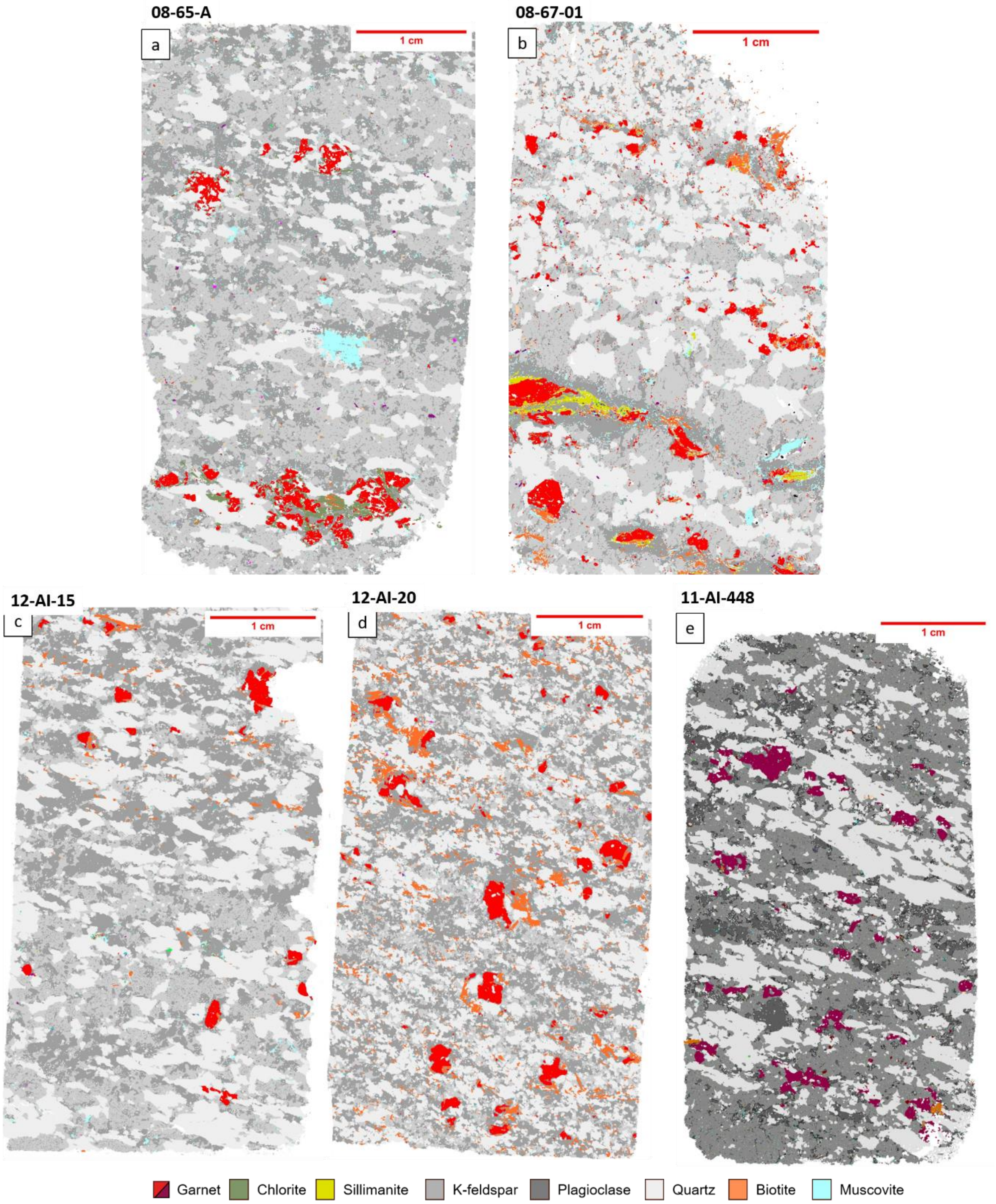

Figure 3.6 SEM–MLA False color mineral maps of leucocratic layers and granites. a,b) Leucocratic samples, interpreted to be leucosome, from PLV1, 08-65-A and 08-67-01, respectively. c, d, e) Granite samples from PLV2: 12-AI-15,12-AI-20, and 11-AI-448 from PLV1, respectively.

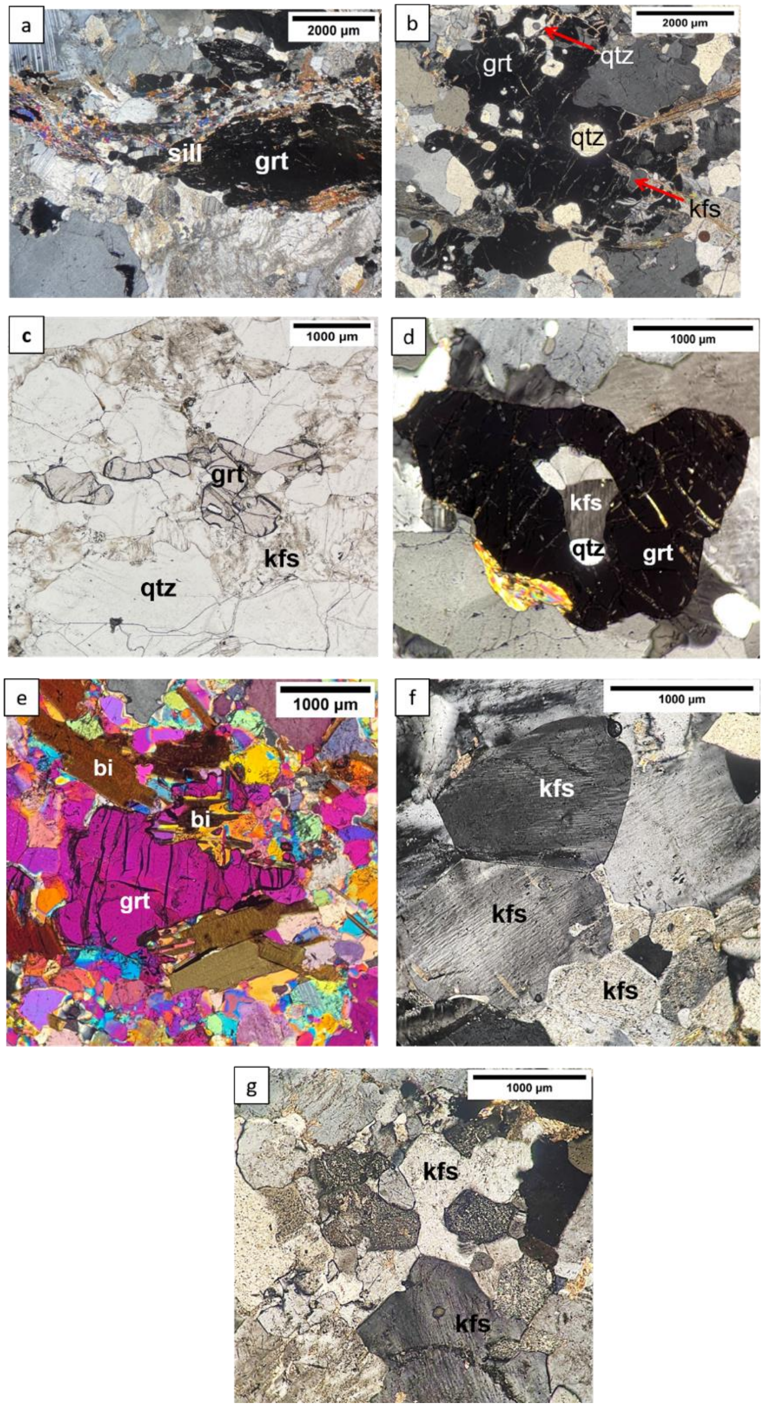

Figure 3.7 Photomicrographs of microstructures in leucocratic layers (a, b) and granites (c to g). a) Prismatic sillimanite surrounding and inside garnet (XP) (08-67-1). b) Garnet porphyroblast with embayments, and inclusions of quartz within a felsic pool (08-65-A) (XP). c) Smaller xenomorphic garnet grains (PPL) (12-AI-15). d) Polymineralic inclusion of quartz and feldspar inside a felsic pool (XP) (11-AI-448). e) Biotite inside a felsic pool (yellow), next to a resorbed garnet (XP with one wave quartz plate) (12-AI-20). f) Interstitial K-feldspar, bottom right (XP) (11-AI-448). g) Interstitial K-feldspar (XP) (11-AI-448).

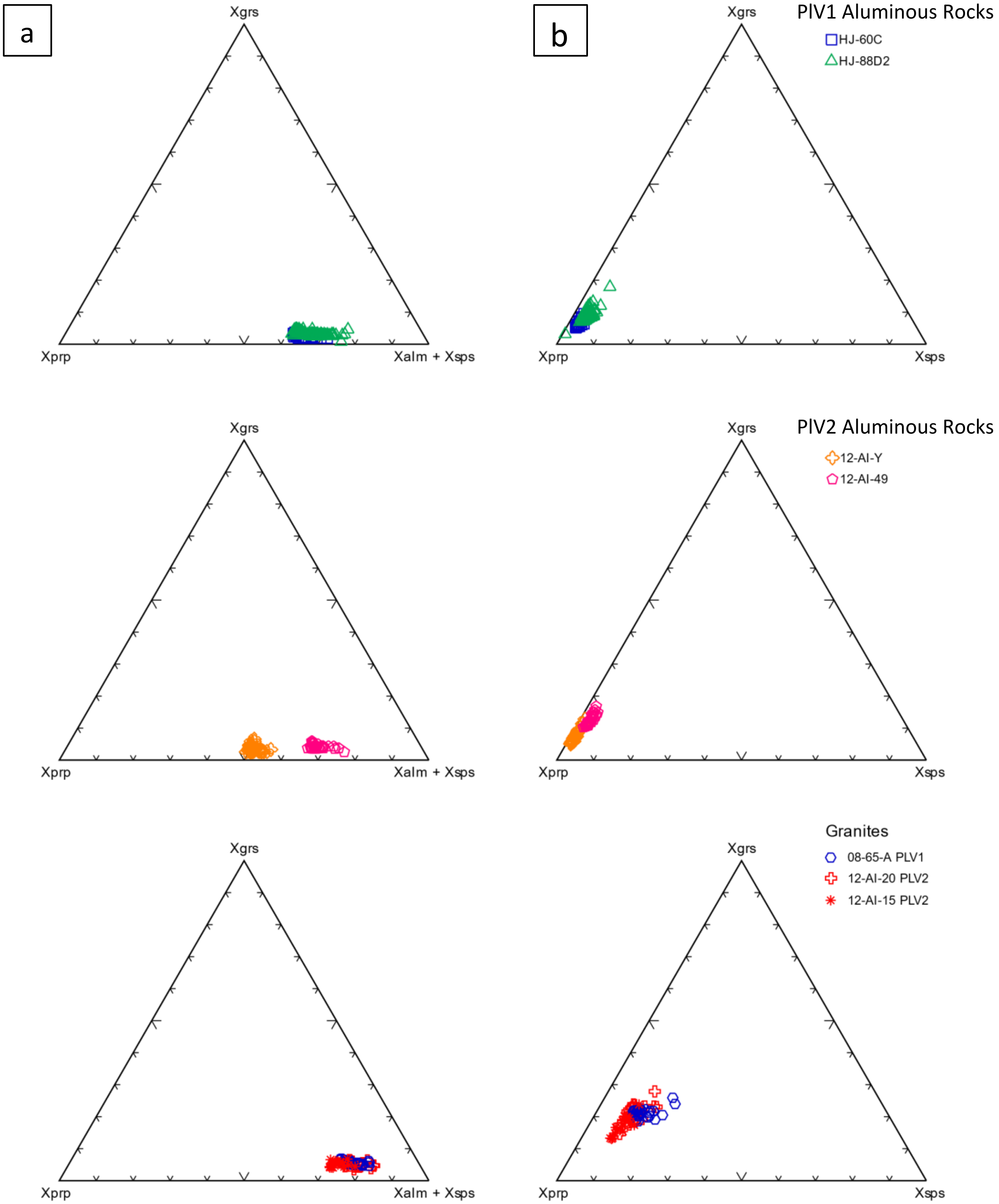

Figure 3.8 a) Ternary diagram of garnet end member compositions from PLV1, PLV2 aluminous rocks, leucocratic layer 08-65-A and PLV granite b) Ternary diagram of garnet end member compositions without almandine (X_{Alm}).

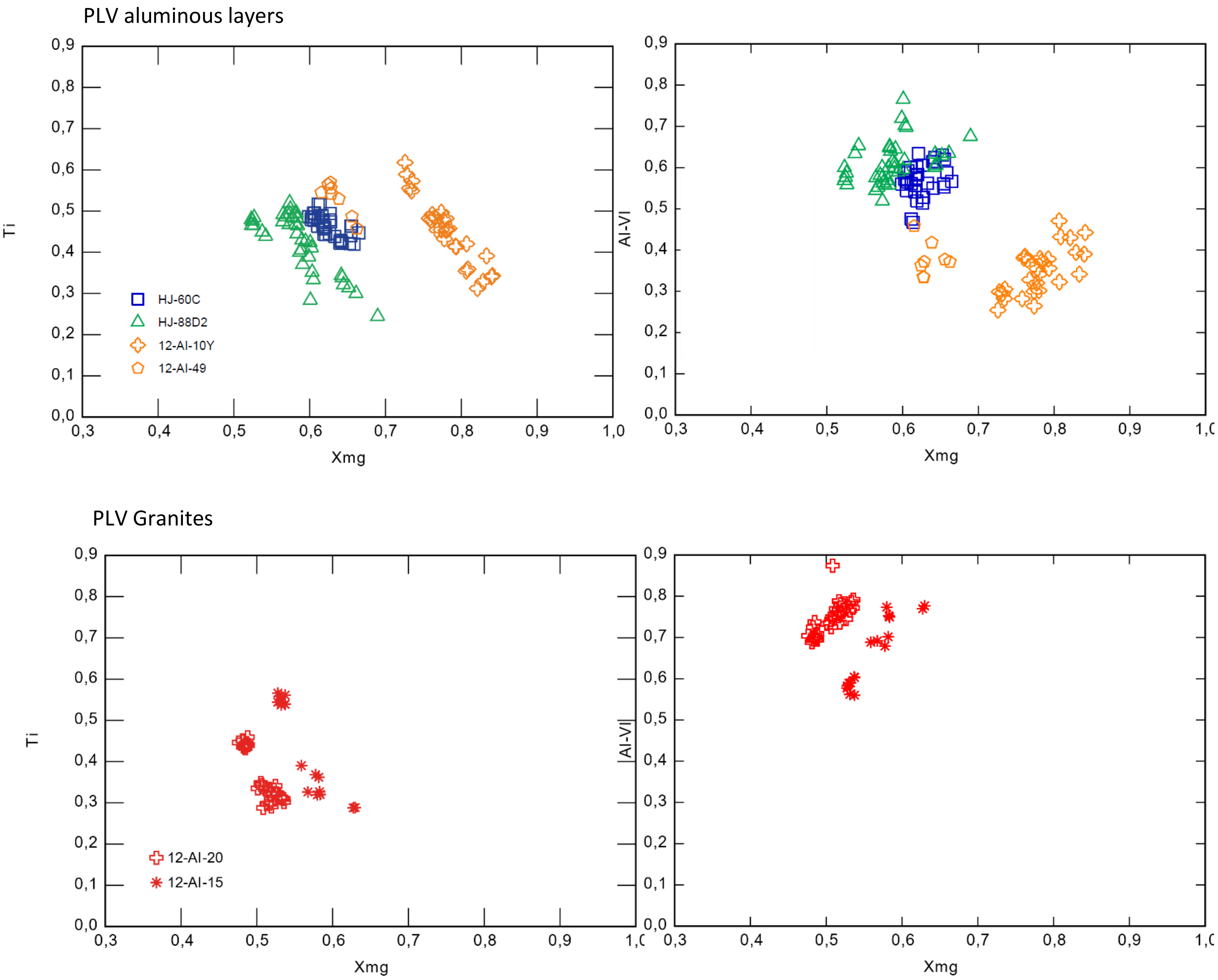

PLV aluminous layers

PLV Granites

Figure 3.9 X_{Mg} vs. Ti p.f.u. (left) and X_{Mg} vs Al^{VI} diagram (right) showing the composition of biotite analyzed near and far from garnet from the PLV aluminous rocks and granites.

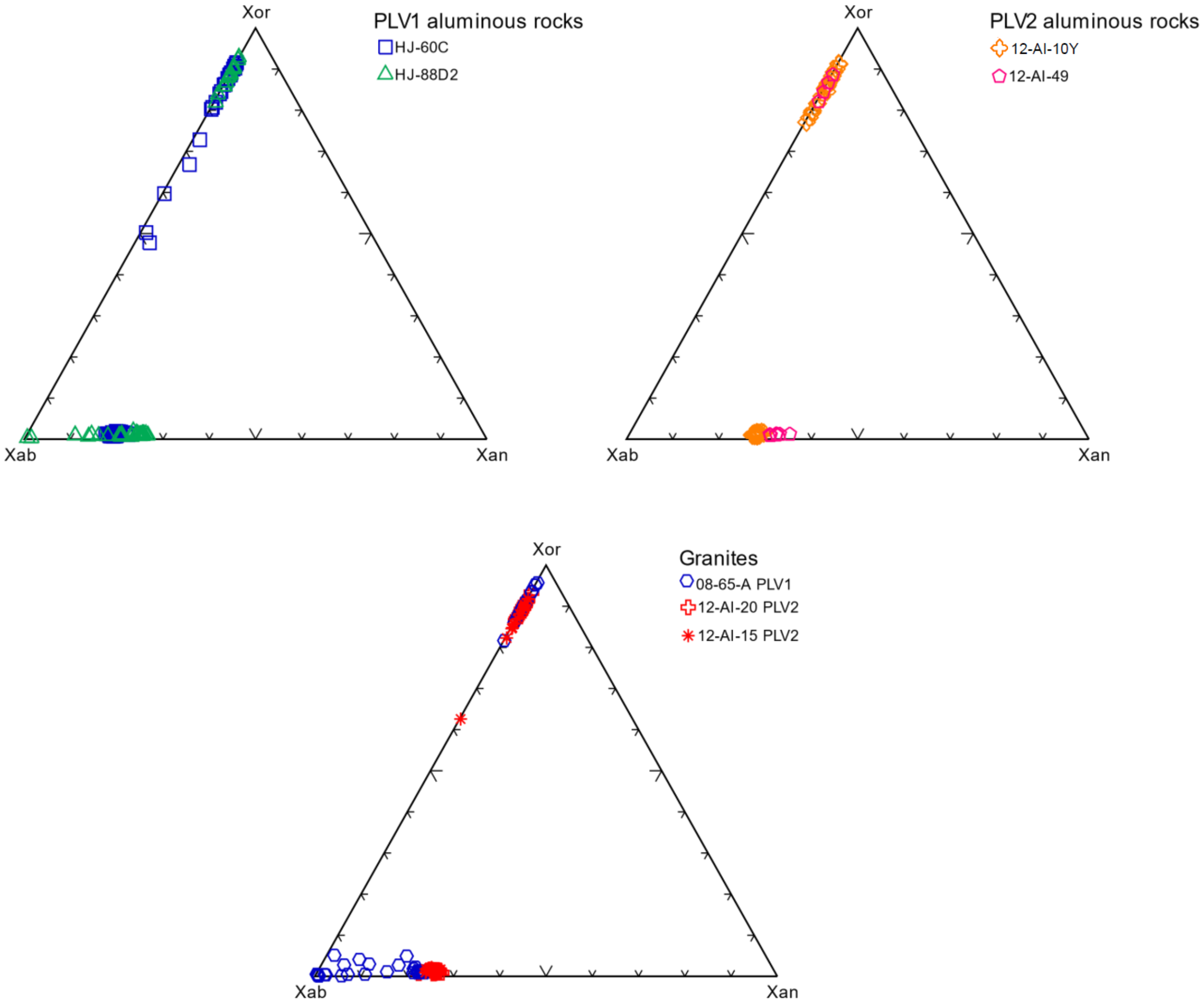

Figure 3.10 Ternary diagram of feldspar end-member compositions, from the PLV aluminous layers, leucocratic layer 08-65-A and PLV granites.

Table 3.1

Mineral proportions of the PLV1 and PLV2 samples obtained from the SEM–MLA.

Minerals mode in area%

	PLV1												PLV2					
Mineral	HJ-60C	HJ-88D2	HJ-60D	08-65A	08-60-1	08-60-2	08-60-3	08-60a-1	08-60a-2	08-60a-3	08-67-1	11-AI-448	12-AI-10E2	12-AI-10F	12-AI-10Y	12-AI-49	12-AI-15	12-AI-20
Garnet	19.58	10.71	12.61	2.74	2.71	0.21	1.52	4.46	7.06	2.32	4.46	3.55	8.61	17.32	15.57	8.31	1.35	3.06
Biotite	9.84	14.47	11.18	0.11	14.50	9.26	12.08	11.32	25.14	9.69	2.53	0.13	14.09	12.64	3.79	16.92	0.86	5.01
Sillimanite	5.58	5.54	7.15	0.01	0.01	0.00	0.01	0.32	5.88	0.00	0.80	0.00	0.02	0.25	2.61	6.48	0.00	0.00
Sum Al	35.00	30.72	30.94	2.86	17.22	9.47	13.61	16.10	38.09	12.00	7.79	3.68	22.72	30.21	21.97	31.71	2.21	8.07
Sil/ Al_{tot}	0.16	0.18	0.23	0.00	0.00	0.00	0.00	0.02	0.15	0.00	0.00	0.00	0.00	0.01	0.12	0.20	0.00	0.00
Quartz	26.37	16.59	22.60	25.53	28.46	37.39	26.25	26.93	5.16	37.50	43.35	36.27	28.96	26.03	27.95	1.11	39.69	39.51
K-feldspar	25.63	33.93	31.36	42.07	10.95	13.91	27.66	34.04	19.44	16.92	30.72	43.99	3.36	3.50	29.81	45.76	27.93	18.62
Plagioclase	12.48	15.27	13.83	25.84	40.00	35.89	29.70	22.34	36.22	32.91	14.76	9.15	44.13	38.81	18.98	19.08	29.59	33.41
Sum QF	64.48	65.79	65.80	93.44	79.40	87.19	83.61	83.31	60.82	87.32	88.83	89.41	76.45	68.34	76.74	65.95	97.21	91.54
Monazite	0.03	0.01	0.04	0.01	0.02	0.01	0.02	0.02	0.02	0.01	0.01	0.00	0.02	0.02	0.02	0.02	0.01	0.01
Rutile	0.09	0.07	0.11	0.05	0.02	0.03	0.02	0.01	0.02	0.02	0.19	0.01	0.03	0.24	0.31	0.07	0.02	0.02
Ilmenite	0.09	0.03	0.08	0.00	0.00	0.00	0.00	0.00	0.00	0.01	0.02	0.23	0.00	0.00	0.00	0.00	0.03	0.09
Spinel	0.00	0.00	0	0.00	0.01	0.00	0.01	0.00	0.01	0.00	0.00	0.00	0.00	0.00	0.00	0.00	0.00	0.00
Pyrite	0.03	0.01	0.02	0.06	0.55	0.56	0.64	0.37	0.60	0.44	0.01	0.00	0.35	0.41	0.37	0.74	0.00	0.01
Group	A	A	A	Q*	Q	Q	Q	Q	A	Q	Q*	G	A	A	A	A	G	G

Note: Sum Al, sum of aluminous minerals; Sil/Altot, sillimanite proportion divided by Sum Al; Sum QF, sum of quartzofeldspathic minerals; A, aluminous rock; Q, quartzofeldspathic layer; Q* quartzofeldspathic layer interpreted to be leucosome; G, granite. *In sample HJ-60c, part of the sillimanite represents partly resorbed and pseudomorphed kyanite.

4 CHAPTER 4: Geochemistry and U-Pb Monazite Dating of the Granites

To test the hypothesis that PLV metapelites and granites are related, three granite samples were geochemically characterized and dated by U–Pb on monazite. Sample 11-AI-448, is from a granite exposure in PLV1, and samples 12-AI-15 and 12-AI-20 are from granite exposures in PLV2. In addition, this chapter discusses the geochemistry of discrete, decimetric-scale leucocratic layers of potentially anatectic origin, interlayered with metapelite.

4.1 Geochemistry of the Granites and Leucocratic Layers of PLV

Major element bulk compositions of the selected samples were obtained using XRF (see chap. 2, section 2.4). The results are shown in Table 4.1 and are plotted in geochemical classification diagrams (Fig. 4.1).

The PLV1 granite, 11-AI-448, stands out by its high K_2O (~6.5 wt%) and low Na_2O content (~1.9 wt%) relative to the PLV2 granites (~3.3–4.6 wt% and 2.8–2.9 wt%, respectively (Fig. 4.1a). The leucocratic layers fall into two distinct groups in terms of K_2O: 4.2–4.8 wt% (4 samples) and 1.7–2.2 wt% (2 samples) but have similar Na_2O contents (2.5–3.5 wt%). The two K_2O -poor samples also have the highest (Na_2O $+CaO$) (AI-08-61) and ($FeO+MgO$) (AI-08-64) proportions (Fig. 4.1b).

In the Q–A–P normative diagram, the granite and most leucocratic compositions spread across the monzogranitic field, with the PLV1 granite straddling on to the grano-syenitic field. In contrast, the K_2O -poor leucocratic layers fall in the granodiorite field (Fig. 4.1c). Most samples are peraluminous except for the K_2O -poor leucocratic rock AI-08-61 which is metaluminous and falls apart from the rest. (Fig. 4.1d).

Overall, the granites and the K_2O - rich leucocratic samples cluster together in the geochemical diagrams and fall in the field of peraluminous granite, whereas the K_2O - poor leucocratic rocks seem to be distinct, with granodioritic compositions, high Al/(Na+K) and marginally peraluminous to markedly metaluminous signatures (Figs. 4c,d).

4.2 U–Pb Monazite Dating

Monazite dating with LA–ICP–MS was used to determine the age of the PLV granites and compare them with the age of metamorphism of the metapelites (for analytical techniques, see chapter 2). The latter ages were constrained on metapelites from PLV1, by U–Pb dating of monazite by TIMS, in the range of 1081–1059 Ma (Ottawan phase) and with a wide spread, even at the sample scale (Dunning and Indares, 2010). In addition, U–Pb dating of monazite from the same samples by ICP-MS showed that part of the spread of the TIMS data is due to a late monazite growth event at 1010–990 Ma, during the Rigolet phase. This late monazite was mostly identified as bright rims in BSE images, around darker, Ottawan age cores (Lasalle et al., 2014).

Eighty-three monazite grains from the PLV1 sample (11-AI-448) were hand-picked using a binocular microscope and mounted afterwards, whereas monazite from the two PLV2 samples (12-AI-15 and 12-AI-20) was dated in-situ (See chapter 2, section 2.4). In these samples, the monazite grains and their locations were identified in the thin section using the SEM–MLA maps, and therefore, their microstructural setting is known. Most monazite is associated with quartz and/or feldspars, except for some grains in granite 12-AI-20, which occur adjacent to ilmenite, biotite and garnet (grains M10 and M6) or included in garnet (grain M7; Fig. 4.2). Prior to dating, the twenty-five largest monazite grains were selected to produce false colour X-ray maps for Th, Nd, Pb, Y and U, along with BSE images, four from sample 12-AI-15 (100.3 – 432.3 μm), seven from sample 12-AI-20 (80.2 – 139.2 μm), and fourteen from sample 11-AI-448 (113.5 – 223.5 μm). Th and Y maps and BSE images of representative monazite are shown in Figures 4.3, 4.4 and 4.5, and the total maps, also including Nd, Pb, and U are found in appendix B.

4.2.1 Monazite morphologies and chemical patterns

The monazite grains display distinct morphologies and chemical patterns.

Generally, the monazite grains from the PLV2 have rims that are variably smoothened by resorption, but some preserve euhedral faces (ex. M1, M2, M3; Figs 4.3, 4.4), with locally high Y next to some of them (ex. M2, M9, M10; Figs 4.3, 4.4).

Monazite grains from sample 12-AI-15 display varied patterns (Fig. 4.3). Most grains (M1, M2, and M3) show distinctive BSE-dark irregular areas enclosed in BSE-brighter domains, whereas the opposite pattern is observed in M4. All four grains have discontinuous BSE-darker rims. The BSE-dark portions of the grains have lower Th and higher Y than the BSE -light parts.

The BSE patterns from sample 12-AI-20 (Fig. 4.4), are not as well defined. Similar to 12-AI-15, in most grains (M5, M6, M9, and M10) the BSE-dark areas of the grains have lower Th and higher Y than the BSE-light parts. In the two other grains (M7 and M11), this link is not as distinguishable, probably because of the poor quality of the BSE images of these grains. M7 and M11 show a patchy distribution of high Y and high Th domains, decoupled from each other.

The monazite grains from the PLV1 sample, 11-AI-448, are more rounded than the previous group but preserve variably smoothened euhedral faces in several instances (ex. M15, M21 – M24; Fig. 4.5), where most of them show high Y contents. They display a wide range of BSE and Th patterns whereas, Y is more subdued relative to the PLV2 monazites. The most common BSE pattern consists of concentric rim (or near-rim) BSE-light zones (M12, M17, M18, M20, M23), in some case truncated (M22, M25), or defining a spiral extending to the core (M14). These bright zones enclose BSE-darker cores that are rounded and smoothened (ex. M12, M19, M20), but locally preserving euhedral faces (ex. M22). Other patterns include subdued, patchy BSE signatures (M16, M24, M21), a BSE-brigher core relative to the rim (M13), and one grain has a ‘feathery’ distribution of bright and dark BSE zones (M15).

As with most of the PLV2 monazites, the BSE-light areas have higher Th contents than the BSE-dark areas. Concerning Y, some grains are nearly homogenous (M13, M15, M16, M23, M24) and the remaining grains show higher Y contents in brighter BSE areas compared to the BSE-dark domains, opposite to the pattern observed in the PLV2.

The Nd, Pb and U maps from both PLV1 and PLV2 grains, show broadly similar zoning pattern as Th, but to a lesser extent, (see appendix B). Homogeneous areas within resolution (20 µm) were selected for dating according to variation in Th content, to find out if these differences in values correspond to different ages.

4.2.2 U–Pb ages

The results are listed in Tables 4.2 and 4.3 with 9, 12 and 23 analyses for sample 12-AI-15, 12-AI-20, and 11-AI-448, respectively. The data are plotted on Concordia diagrams (Fig. 4.6) and weighted average ^{206}Pb/^{238}U ages were calculated for groups of closely overlapping data. Three analyses were not concordant, two from PLV1 (analyses #29 and #40; 1060± 32 and 1019 ±29 Ma, respectively) and one from PLV2 (analysis #12; 1057 ± 41 Ma), these were not considered for the weighted averages. Calculations were done with Isoplot (version 3.7; Ludwig, 2012), and reported uncertainties are plotted and recorded at 2 sigma confidence intervals (Fig. 4.6). In the next section, the ages cited are $^{206}Pb/^{238}U$. In addition, Grenvillian ages are labelled as Ottawan or Rigolet, following the age ranges defined by Rivers et al. (2012) (Ottawan: 1090 to 1020 Ma; Rigolet: 1005 to 980 Ma).

4.2.2.1 PLV2

The monazite ages from the two PLV2 granites vary from 1355 Ma to 1034 Ma (Table 4.3, Fig. 4.6a). Pre-Grenvillian ages (1355 ± 45 Ma, 1177±46 Ma, 1131 ± 37 Ma, and 1121±54) are preserved in 4 grains of sample 12-AI-20. These ages were measured in cores of homogeneous grains (M7, M11) or at moderate to high Th patches in the core of monazites (M9, M10) that have Ottawan, lower Th rim domains. The oldest grain (M7, 1355 ± 45 Ma) is included in garnet and the other three are in contact with quartz and feldspar. Ottawan ages fall in two main clusters, with weighted averages of 1087 ± 16 Ma (n=5) and 1062 ± 10 Ma (n=11). In sample 12-AI-15, all 4 grains analyzed showed Ottawan ages in both BSE-dark (Th poor) and BSE-bright (Th rich) domains. These ages range from 1097± 34 Ma to 1034 ± 35 Ma, with an analysis from M2 showing an age of 1106 ± 37 inside a low Th, BSE-dark domain. These monazites are in groundmass and are in contact with quartz and feldspar.

4.2.2.2 PLV1

All individual monazite spot ages from the PLV1 granite are Grenvillian, ranging from 1065 to 980 Ma (Fig. 4.6b). Ottawan ages are represented by two main clusters of 3 and 10 analyses with weighted average of 1062 ± 17 Ma and 1033 ± 10 Ma respectively. These ages are in both cores and rims of the grains and have variable Th content.

There may be two younger clusters, 1002 ± 14 (n=5) and 985 ± 20 Ma (n=3), that fall in the Rigolet age range, but due to the laser data uncertainty, the ages overlap. These are recorded in chemically homogenous (Th, Y) grains (M16, M21), in cores and rims (M24) and at the BSE bright rims of M18 and M19, with moderate to high Th in most cases. For these two clusters, the element values from the chemical maps in counts per second were examined to determine if these grains are chemically distinct (Table 4.4, Fig. 4.7). The results show some difference in the counts, the younger cluster of 985 ± 20 Ma (orange) show higher Th/Y, Th/U and Th/Nd ratios than 4 of 5 analyses in the 1002 ± 14 Ma cluster (black). This might represent a chemical difference between the two younger ages, although there are two anomalous values, one from each group. Monazite M21 (1007 ± 37 Ma), shows higher Th values than the rest of the grains, whereas the core of grain M19 (980 ± 35 Ma) is significantly depleted in Th.

4.3 Summary and Discussion

Overall, monazite grains are variably rounded and smoothened, with those from PLV2 having more irregular shapes. However, in all samples, some grains preserve some idiomorphic rims, with some of these rims showing high Y. This is suggestive of monazite growth in the presence of melt, whereas the rounded rims suggest variable subsequent resorption (Kohn, 2016; Hetherington et al., 2017). In addition, the preservation of rounded or patchy BSE and chemical domains in the cores of several monazite grains, are generally consistent with different stages of growth and resorption in the monazite history.

PLV2 monazite grains show some pre-Grenvillian and only Ottawan ages, whereas the PLV1 monazite shows Ottawan and Rigolet ages. Two types of pre-Grenvillian ages are recorded in PLV2 granites: 1355 ± 45 and 1177±46 Ma to 1121±54, while Ottawan ages span from 1087 ± 16 to 1062 ± 10 Ma. Ottawan ages of the PLV1 granite are younger, with two main clusters at 1062 ± 17 Ma and 1033± 10 Ma. Rigolet ages in the PLV1 are 1002 ± 14 to 985 ± 20 Ma, with significant overlap but with different element chemistry.

Pre-Grenvillian monazite is only present in the PLV2. The zoning patterns are more faint and less defined in the most corroded grains (M7 and M11) and cannot be correlated to a distinct Th nor Y composition. Most Ottawan monazite from the PLV2 shows a consistent pattern where BSE-dark domains correspond to lower Th and higher Y contents, compared to the BSE-light areas. In the PLV1 this trend is only observed for the Th maps since Y values are also higher in bright BSE areas in both Ottawan and Rigolet monazite grains. The arrangement of these domains varies from grain to grain, for some of them, the BSE-dark zones are enclosed in BSE-light areas (e.g. M1, M2, M3, M8), whereas the opposite is seen in the other monazite grains (e.g. M4, M5, M6, M10).

These results show the variability and style of the monazite grains studied by Lasalle et al. (2014), and are consistent with the analyzed ages, where they determined some inherited Pre-Grenvillian ages up to 1400 Ma, Ottawan ages in the main cluster (1070–1020 Ma) and Rigolet ages (1010– 990 Ma), where the Rigolet ages were found mostly in BSE-light rims, and Ottawan ages in BSE-dark cores. The main cluster from the PLV granites ranges between 1033 ± 10 and

1087 ± 16 Ma (weighted average), corresponding to the main Ottawan ages also found by Lasalle et al. (2014). However, the ages shown by the monazite from the PLV granites, are most commonly found in entire grains rather than in core or rims.

Figures Chapter 4

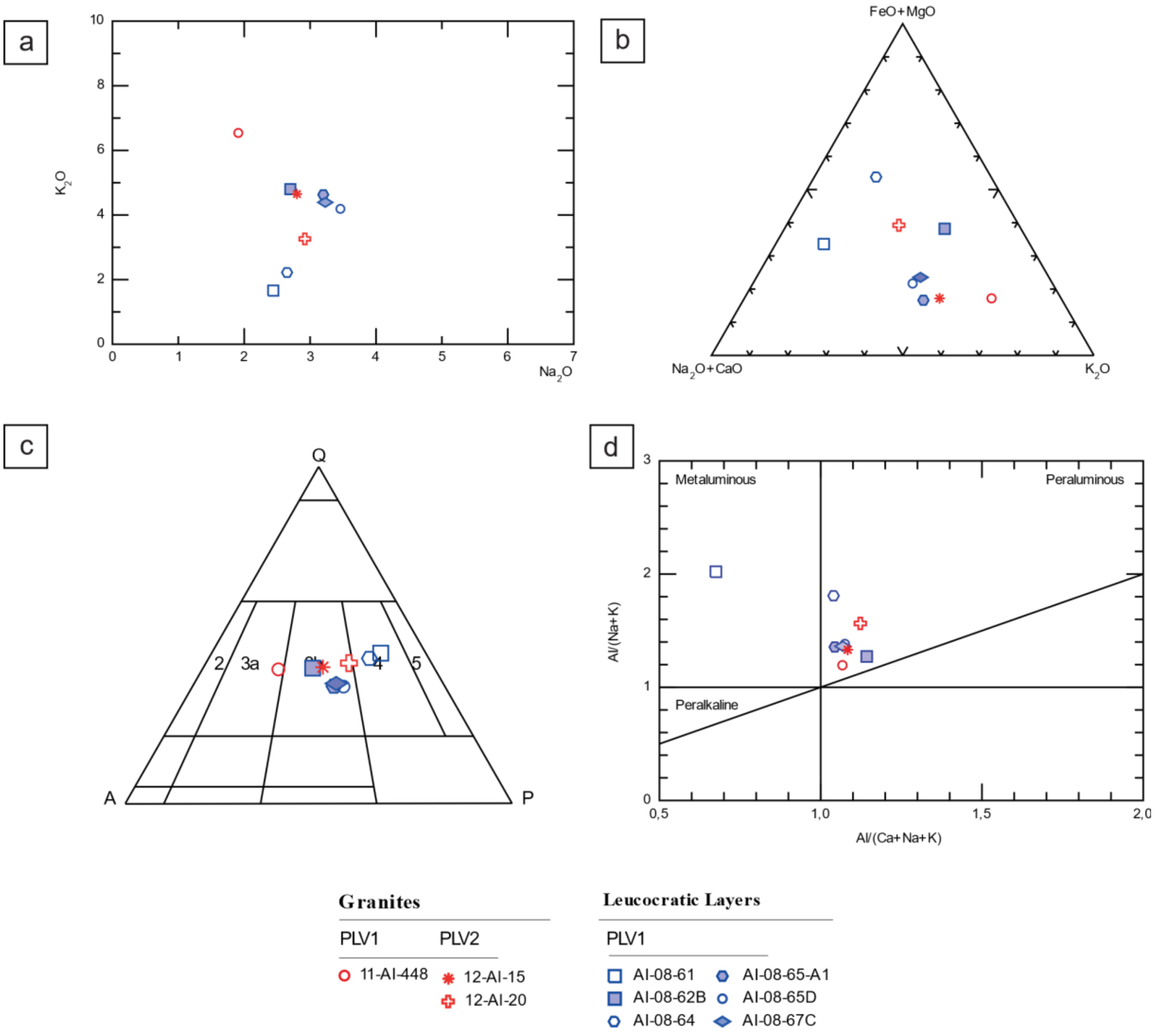

Figure 4.1 Geochemical classification diagrams for the PLV granites, and the leucocratic layers from PLV1. a) Na_2O vs K_2O (wt%). b) $FeO + MgO$ Vs Na_2O + CaO vs K_2O (mol%).c) Q–A–P (wt%). d) Shand's Index. QAP legend: 2, Alkali-Feldspar Granite; 3a, Syenogranite; 3b, Monzogranite; 4, Granodiorite; 5, Tonalite.

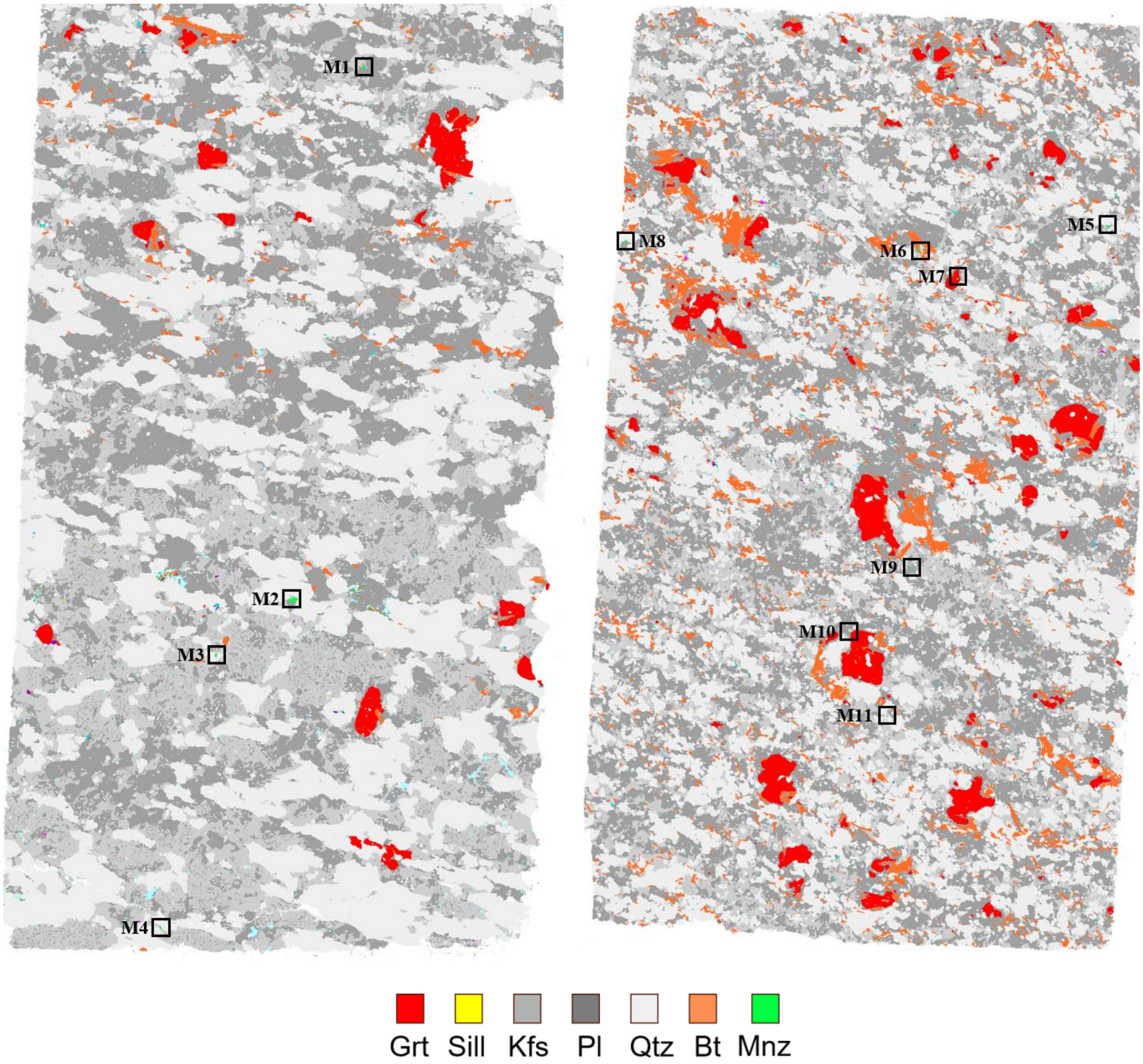

Figure 4.2 SEM–MLA maps of PLV granite samples 12-AI-15 (left) and 12-AI-20 (right) with the location of the monazite grains analyzed.

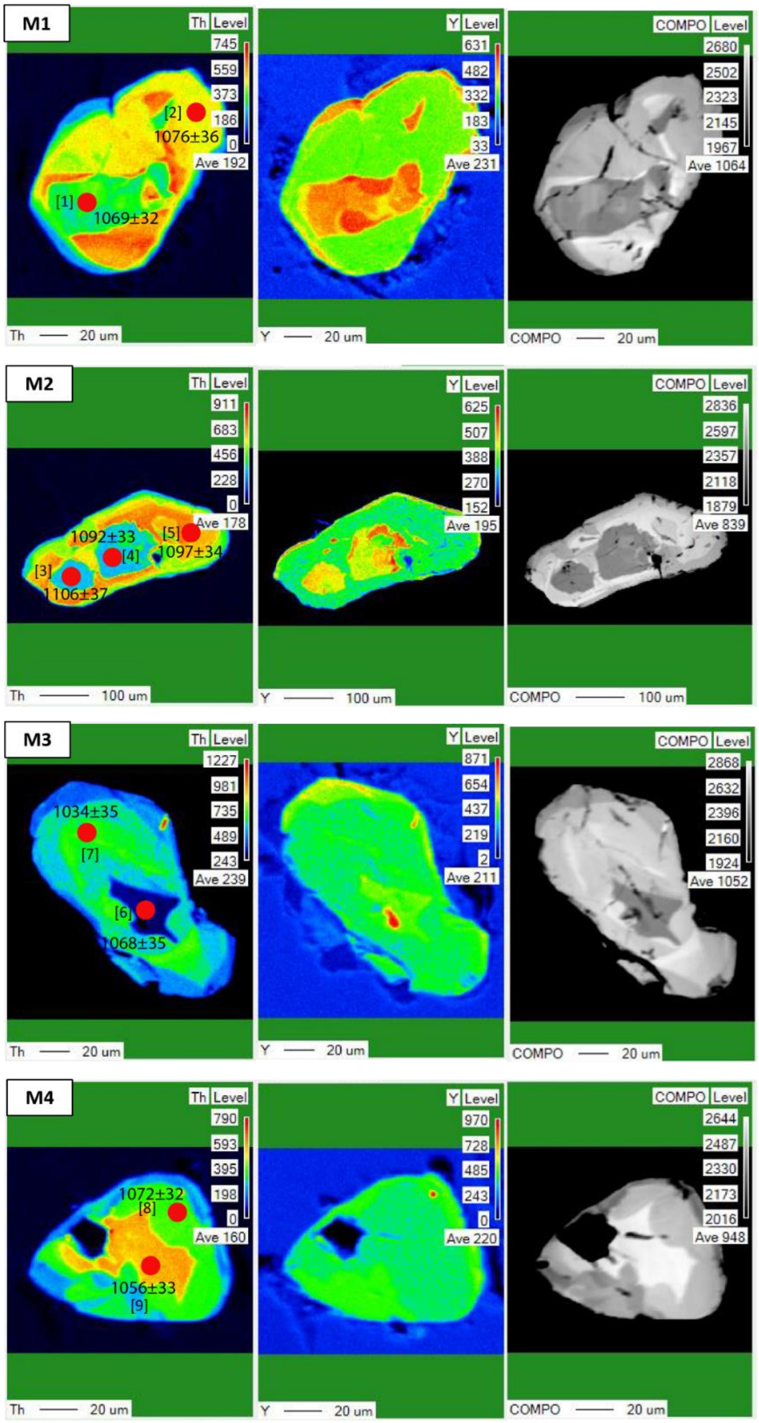

Figure 4.3 Th, Y and BSE maps showing the internal structure of typical monazites from sample 12-AI-15 of PLV2.

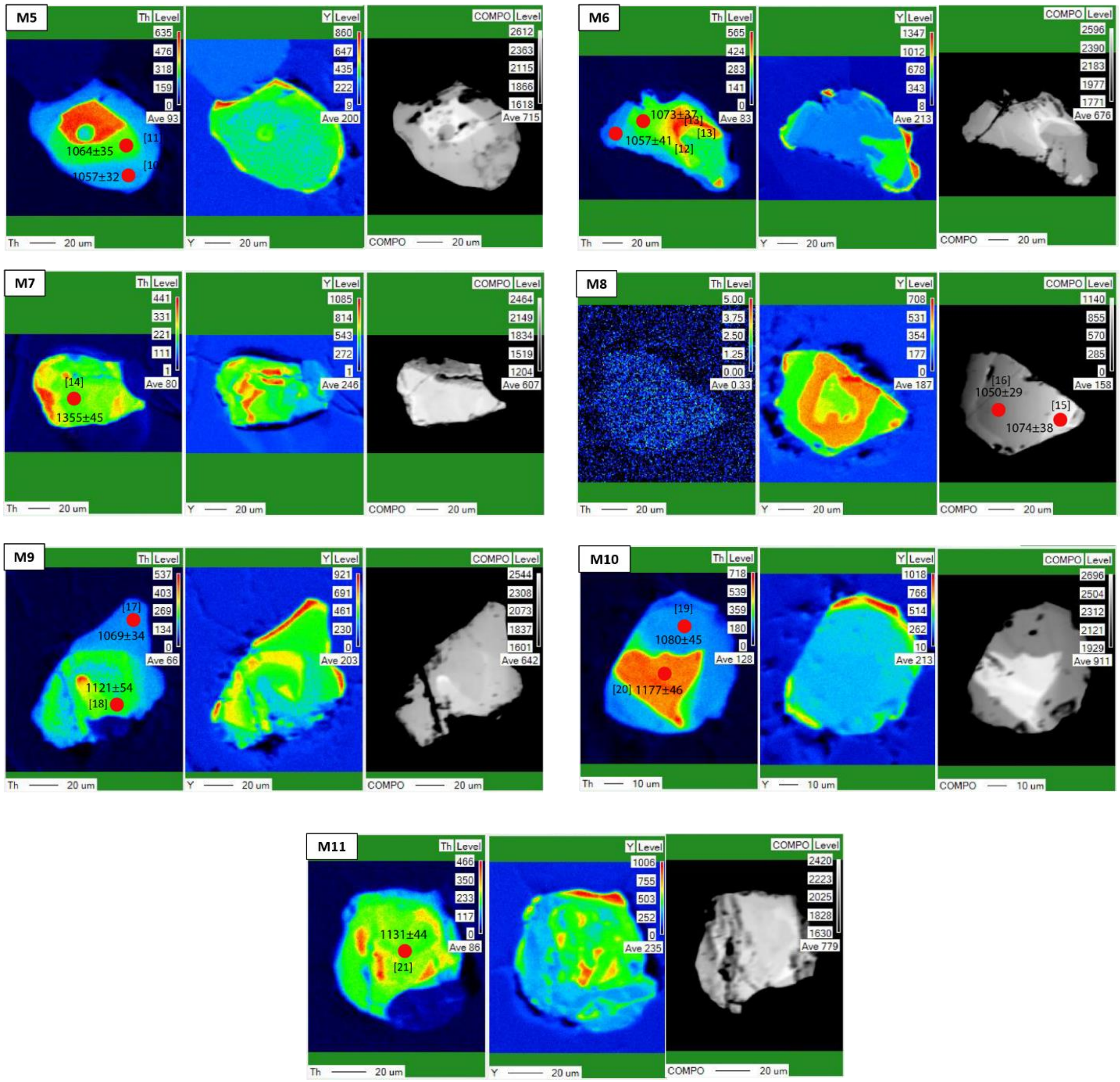

Figure 4.4 Th, Y and BSE maps showing the internal structure of typical monazites from sample 12-AI-20 of PLV2.

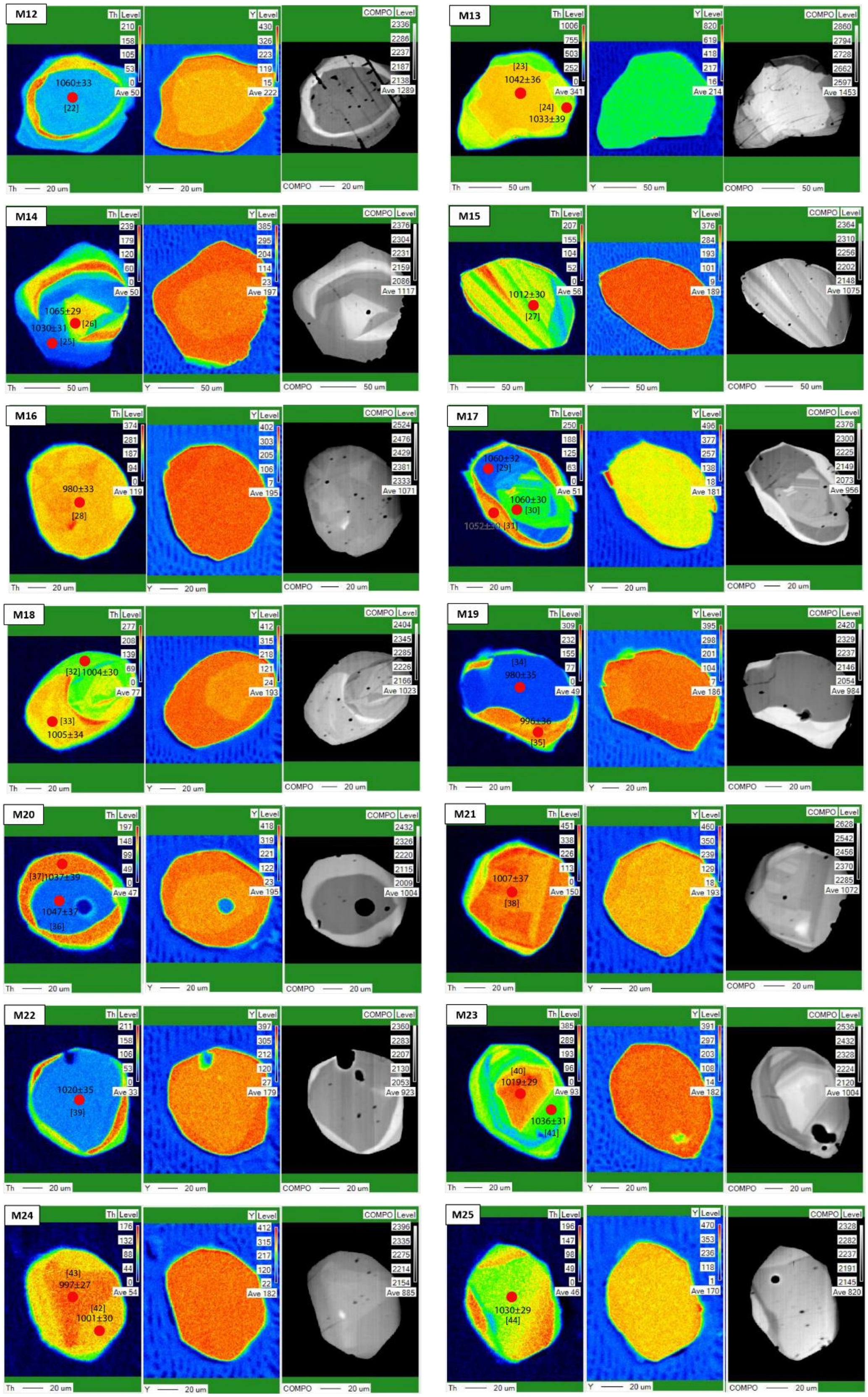

Figure 4.5 PLV1 Th maps showing the internal structure of typical monazites.

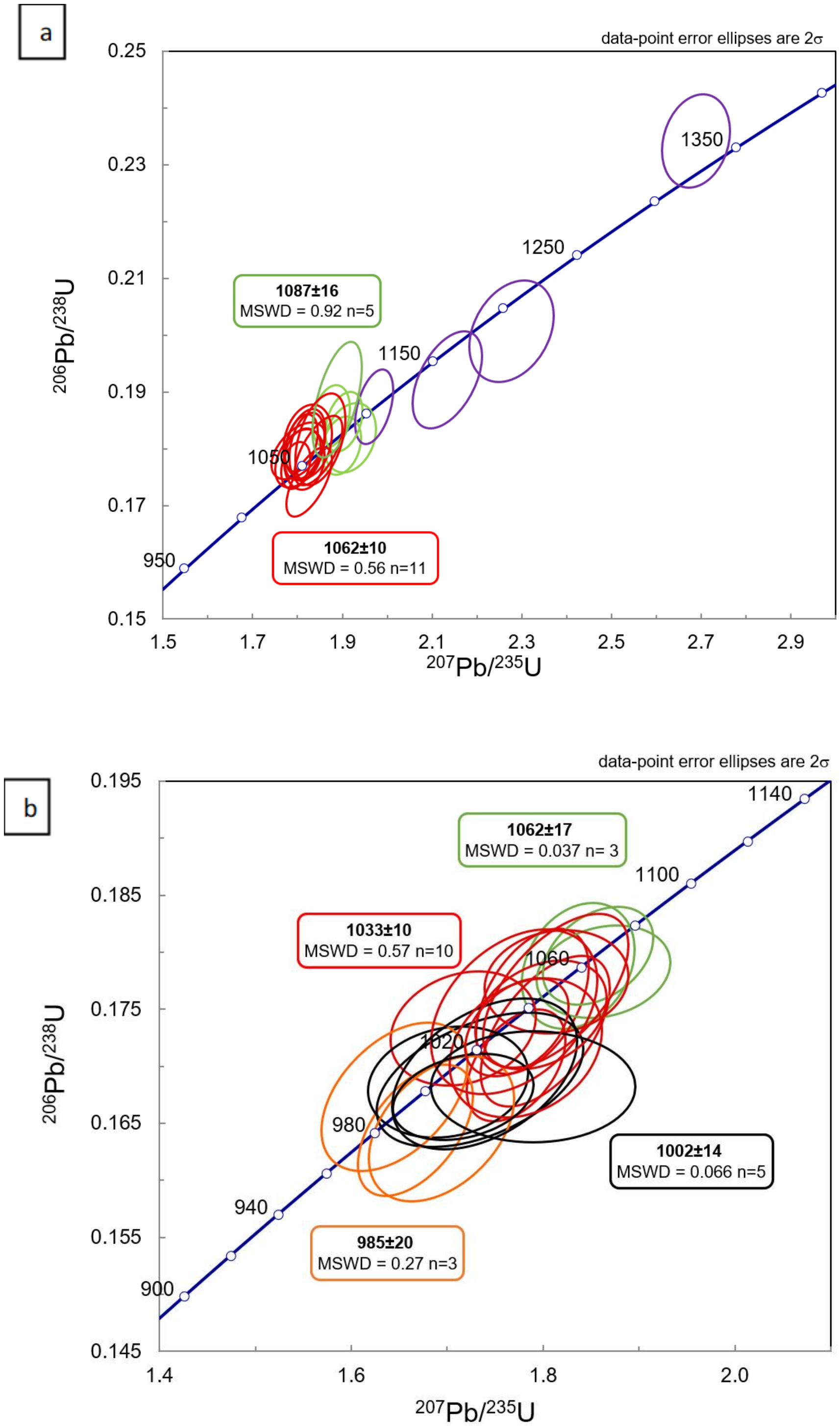

Figure 4.6 Concordia diagrams. a) Samples 12-AI-15 and 12-AI-20 from PLV2. b) Sample 11-448 from PLV1. Several entire grains yielded the older ages, and apparent cores with different chemistry in some grains were within resolution the same age.

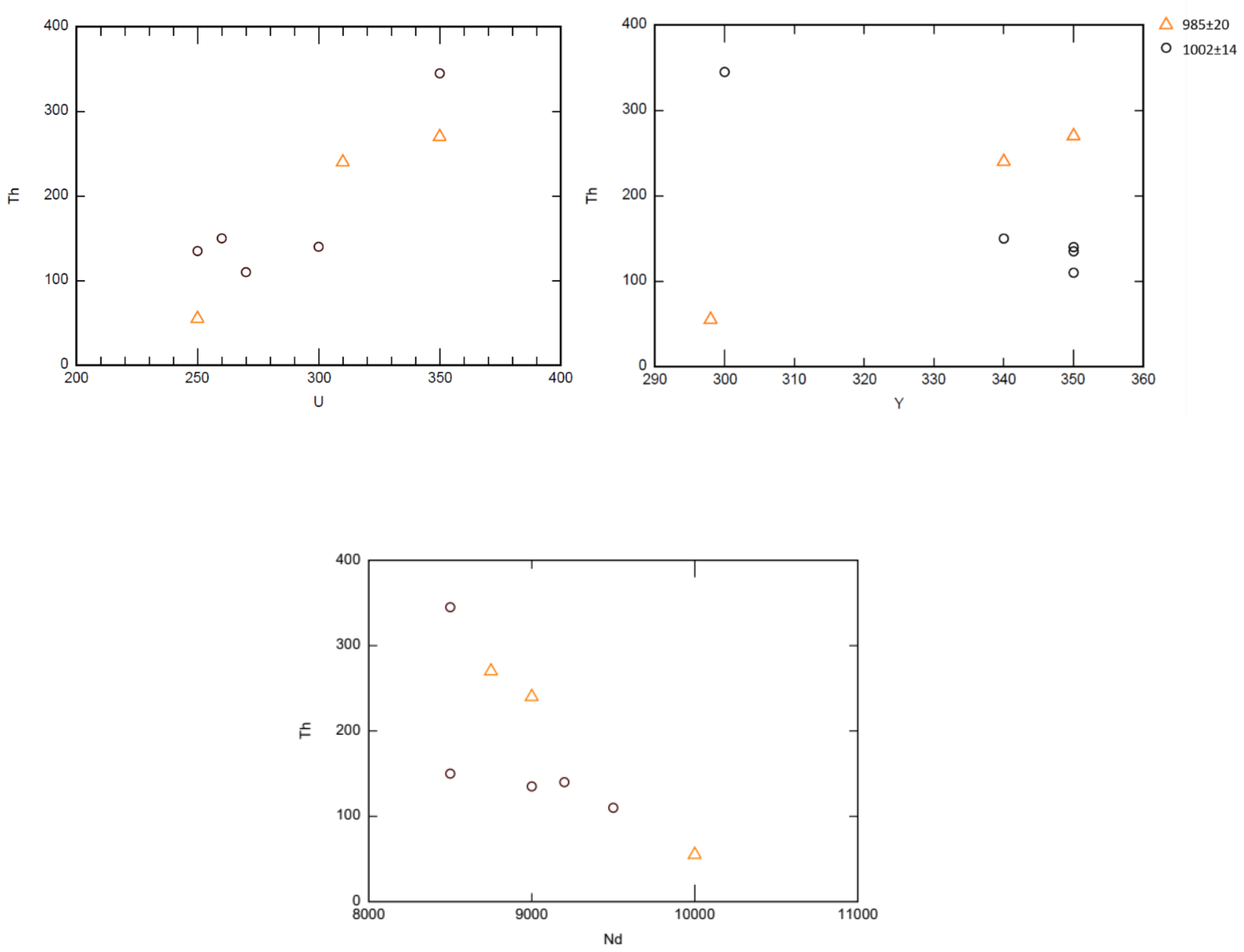

Figure 4.7 Th/U, Th/Y and Th/Nd ratios (counts per second) from the younger monazite clusters of sample 11-AI-448 (PLV1).

Table 4.1

Major element composition of granite and leucocratic (leucosome) samples from the PLV.

Geochemistry wt%

Area	Sample	Group	SiO2	Al2O3	FeO	MnO	MgO	CaO	Na2O	K2O	TiO2	P2O5	Total
PLV1	AI-08-61	L	71.73	11.74	2.54	0.06	1.05	6.37	2.44	1.66	0.38	0.14	100
	AI-08-62B	L	74.86	12.26	2.64	0.02	0.95	0.60	2.70	4.80	0.39	0.04	100
	AI-08-64	L	72.51	12.23	3.52	0.06	2.28	2.75	2.65	2.22	0.39	0.08	100
	AI-08-65-A1	L	74.19	13.93	1.05	0.02	0.31	1.69	3.20	4.63	0.20	0.09	100
	AI-08-65D	L	73.86	14.14	1.51	0.04	0.33	1.61	3.46	4.19	0.18	0.06	100
	AI-08-67C	L	73.96	13.71	1.67	0.06	0.37	1.52	3.23	4.39	0.15	0.07	100
	11-AI-448	G	76.59	12.21	1.41	0.03	0.12	0.67	1.91	6.54	0.10	0.11	100
PLV2	12-Al-15	G	76.65	12.83	1.13	0.03	0.21	1.21	2.80	4.65	0.07	0.02	100
	12-Al-20	G	74.41	13.03	2.89	0.05	0.76	1.80	2.92	3.26	0.34	0.04	100

Geochemistry mol%

Area	Sample	Group	SiO2	Al2O3	FeO	MnO	MgO	CaO	Na2O	K2O	TiO2	P2O5	Total
PLV1	AI-08-61	L	78.12	7.53	2.97	0.05	1.70	5.80	1.69	1.75	0.31	0.07	100
	AI-08-62B	L	80.04	7.72	3.02	0.02	1.52	0.53	1.84	4.98	0.31	0.02	100
	AI-08-64	L	77.64	7.71	4.03	0.05	3.63	2.47	1.81	2.30	0.31	0.04	100
	AI-08-65-A1	L	80.52	8.91	1.22	0.02	0.50	1.53	2.22	4.87	0.17	0.04	100
	AI-08-65D	L	80.18	9.05	1.76	0.04	0.53	1.46	2.40	4.41	0.15	0.03	100
	AI-08-67C	L	80.25	8.77	1.94	0.06	0.59	1.38	2.23	4.61	0.13	0.03	100
	11-AI-448	G	81.70	7.67	1.61	0.03	0.19	0.60	1.30	6.76	0.08	0.05	100
PLV2	12-Al-15	G	82.31	8.12	1.30	0.03	0.33	1.09	1.92	4.84	0.06	0.01	100
	12-Al-20	G	79.88	8.24	3.32	0.05	1.21	1.62	2.00	3.39	0.28	0.02	100

Note: L* Leucocratic layer interpreted to represent leucosome. G* PLV granite.

Table 4.2

Monazite U–Pb data for the PLV1 (11-AI-448) and PLV2 (12-AI-15, 12-AI-20) granite samples.

Sample	Monazite	# of the analysis	Ratio						
			^{207}Pb/ ^{235}U	2SE	^{206}Pb/ ^{238}U	2SE	Correlation	^{207}Pb/ ^{206}Pb	2SE
12-AI-15	M1	1	1.8970	0.0670	0.1805	0.0059	0.2610	0.0756	0.0016
		2	1.9170	0.0750	0.1819	0.0065	0.2522	0.0743	0.0018
	M2	3	1.9710	0.0680	0.1874	0.0068	0.4384	0.0780	0.0017
		4	1.9040	0.0660	0.1847	0.0060	0.3587	0.0748	0.0015
		5	1.8750	0.0660	0.1857	0.0062	0.2718	0.0746	0.0016
	M3	6	1.8210	0.0630	0.1803	0.0064	0.3224	0.0739	0.0018
		7	1.8260	0.0680	0.1742	0.0063	0.6449	0.0768	0.0019
	M4	8	1.8080	0.0620	0.1810	0.0058	0.3796	0.0738	0.0016
		9	1.8150	0.0650	0.1782	0.0060	0.1204	0.0736	0.0016
12-AI-20	M5	10	1.8010	0.0670	0.1783	0.0058	0.3935	0.0743	0.0016
		11	1.8470	0.0710	0.1797	0.0065	0.6418	0.0759	0.0018
	M6	12	2.0010	0.0840	0.1783	0.0075	0.1835	0.0807	0.0022
		13	1.8230	0.0700	0.1813	0.0067	0.2110	0.0737	0.0020
	M7	14	2.6890	0.1000	0.2342	0.0086	0.2081	0.0844	0.0021
	M8	15	1.8160	0.0660	0.1807	0.0066	0.4077	0.0746	0.0018
		16	1.7960	0.0600	0.1771	0.0053	0.3015	0.0749	0.0015
	M9	17	1.8020	0.0730	0.1796	0.0058	0.4970	0.0735	0.0017
		18	1.8880	0.0720	0.1886	0.0093	0.5639	0.0737	0.0020
	M10	19	1.8510	0.0720	0.1817	0.0078	0.4393	0.0733	0.0019
		20	2.2770	0.1000	0.2007	0.0086	0.3032	0.0847	0.0023
	M11	21	2.1340	0.0900	0.1921	0.0082	0.4875	0.0801	0.0021
11-AI-448	M12	22	1.8370	0.0730	0.1788	0.0060	0.2612	0.0736	0.0018
	M13	23	1.7890	0.0720	0.1757	0.0065	0.4634	0.0758	0.0022
		24	1.8020	0.0770	0.1731	0.0067	0.5654	0.0748	0.0025
	M14	25	1.7170	0.0800	0.1733	0.0057	0.2090	0.0703	0.0021
		26	1.8570	0.0730	0.1797	0.0053	0.3650	0.0735	0.0017
	M15	27	1.7720	0.0670	0.1701	0.0055	0.4549	0.0745	0.0019
	M16	28	1.6670	0.0700	0.1644	0.0060	0.5212	0.0717	0.0021
	M17	29	1.9970	0.0950	0.1789	0.0058	0.2503	0.0764	0.0022
		30	1.8630	0.0800	0.1783	0.0052	0.2004	0.0734	0.0018
		31	1.8140	0.0810	0.1774	0.0055	0.1214	0.0738	0.0020
	M18	32	1.7010	0.0850	0.1686	0.0055	0.1637	0.0711	0.0020
		33	1.7340	0.1000	0.1688	0.0061	0.4630	0.0736	0.0024
	M19	34	1.6940	0.0800	0.1645	0.0064	0.4121	0.0728	0.0023
		35	1.6450	0.0790	0.1673	0.0065	0.4558	0.0720	0.0025
	M20	36	1.8130	0.0830	0.1766	0.0068	0.5901	0.0721	0.0020
		37	1.7700	0.0880	0.1748	0.0071	0.3811	0.0720	0.0021
	M21	38	1.7390	0.0950	0.1693	0.0066	0.4351	0.0736	0.0022
	M22	39	1.7820	0.0840	0.1716	0.0063	0.2544	0.0729	0.0021
	M23	40	2.0600	0.0830	0.1704	0.0057	0.1172	0.0843	0.0022
		41	1.7980	0.0780	0.1745	0.0056	0.3125	0.0743	0.0019
	M24	42	1.7900	0.1000	0.1682	0.0055	-0.0016	0.0715	0.0022
		43	1.7170	0.0790	0.1673	0.0049	0.2786	0.0721	0.0020
	M25	44	1.7730	0.0690	0.1734	0.0052	0.4210	0.0729	0.0018

Table 4.3

Monazite U–Pb ages for the PLV1 (11-AI-448) and PLV2 (12-AI-15, 12-AI-20) granite samples.

Sample	Monazite	# of the analysis	Ages					
			$^{207}Pb/^{235}U$	2SE	$^{206}Pb/^{238}U$	2SE	$^{207}Pb/^{206}Pb$	2SE
12-AI-15	M1	1	1078	23	1069	32	1084	42
		2	1087	25	1076	36	1050	49
	M2	3	1106	22	1106	37	1146	43
		4	1081	23	1092	33	1062	40
		5	1071	23	1097	34	1057	43
	M3	6	1052	23	1068	35	1039	49
		7	1061	20	1034	35	1116	49
	M4	8	1047	22	1072	32	1037	44
		9	1049	24	1056	33	1030	44
12-AI-20	M5	10	1044	24	1057	32	1049	43
		11	1060	25	1064	35	1092	47
	M6	12	1114	29	1057	41	1214	54
		13	1052	25	1073	37	1033	55
	M7	14	1324	28	1355	45	1302	48
	M8	15	1050	24	1074	38	1058	49
		16	1043	22	1050	29	1067	40
	M9	17	1043	26	1069	34	1028	47
		18	1075	25	1121	54	1033	55
	M10	19	1061	26	1080	45	1022	52
		20	1204	33	1177	46	1309	53
	M11	21	1157	29	1131	44	1199	52
11-AI-448	M12	22	1056	25	1060	33	1031	49
	M13	23	1038	27	1042	36	1090	58
		24	1045	27	1033	39	1063	67
	M14	25	1011	30	1030	31	937	61
		26	1063	26	1065	29	1028	47
	M15	27	1036	26	1012	30	1055	51
	M16	28	991	27	980	33	977	60
	M17	29	1112	33	1060	32	1106	58
		30	1063	28	1060	30	1025	50
		31	1050	31	1052	30	1036	55
	M18	32	1002	31	1004	30	960	57
		33	1015	37	1005	34	1031	66
	M19	34	999	31	980	35	1008	64
		35	985	30	996	36	986	71
	M20	36	1045	30	1047	37	989	56
		37	1027	33	1037	39	986	59
	M21	38	1021	37	1007	37	1031	60
	M22	39	1035	31	1020	35	1011	58
	M23	40	1133	28	1019	29	1299	51
		41	1041	28	1036	31	1050	52
	M24	42	1032	36	1001	30	972	63
		43	1010	29	997	27	989	56
	M25	44	1033	25	1030	29	1011	50

Table 4.4

Counts per second values from Th, Y, U, Nd and Pb chemical maps for the younger monazite grains of the PLV1 sample 11-AI-448.

11-AI-448 Younger Ages

Monazite	# of the analysis	$^{206}Pb/^{238}U$	2SE		Th	Y	U	Nd	Pb	Th/Y	Th/U	Th/Nd
Orange: 985 ± 20 Ma												
M16	28	980	33	Core	270.00	350.00	350.00	8750.00	65.00	0.77	0.77	0.03
M19	34	980	35	Core	55.00	298.00	250.00	10000.00	53.00	0.18	0.22	0.01
	35	996	36	Rim	240.00	340.00	310.00	9000.00	65.00	0.71	0.77	0.03
Black: 1002 ± 14 Ma												
M18	32	1004	30	Rim	135.00	350.00	250.00	9000.00	48.00	0.39	0.54	0.02
	33	1005	34	Core	170.00	340.00	260.00	8500.00	60.00	0.50	0.65	0.02
M21	38	1007	37	Core	345.00	300.00	350.00	8500.00	100.00	1.15	0.99	0.04
M24	42	1001	30	Rim	110.00	350.00	270.00	9500.00	44.00	0.31	0.41	0.01
	43	997	27	Core	140.00	350.00	300.00	9200.00	65.00	0.40	0.47	0.02

5 CHAPTER 5: Phase Equilibria Modelling

Phase equilibria modelling was conducted to (a) calculate *P–T* pseudosections for two aluminous layers of the PLV (HJ-60C, PLV1and 12-10-Y, PLV2) to: (a) infer *P–T* paths and set the framework for melt calculations; and (b) determine the compositions of anatectic melt produced at selected *P–T* points, to compare them with the composition of the PLV granites. In addition, anatectic melt compositions were calculated using aluminous samples from the broader area (Fig. 1.2): hydrothermally altered felsic rocks (HAF; samples 216c, 333x from the northern part of the mid-*P* belt and aluminous rocks from the structurally lower high-*P* belt (samples 244 and 320). For these samples, pseudosections for *P–T* determinations were published in Lasalle and Indares (2014) and Indares et al. (2008) and are reproduced here to provide the basis for the melt calculations.

The bulk compositions of all rocks (Table 5.1) are derived by combining mineral chemistry, and modal proportions (see Appendix C.1) and were plotted on AFM and binary K_2O vs Na_2O, K_2O and vs $Na_2O + CaO$ diagrams (Fig. 5.1). The Alumina Index of all bulk compositions varies from 0.2 to 0.3. Samples HJ60x, 333x and 320 have higher FeO/(FeO+MgO) than the 12-AI-10y, 216c and 244 (F=~0.6 and ~0.5, respectively; Fig. 5.1.a). Most rocks are similar in terms of K_2O and Na_2O contents (about 3 wt% and 2 wt% respectively) except for the HAF rocks which are richer in Na_2O, with sample 333x showing the highest Na_2O and K_2O contents (about 3.5 w% and 5 wt% respectively; Figs. 5.1.b, c).

5.1. *P–T* Pseudosections for the PLV1 and PLV2 Samples

Two sets of pseudosections were calculated: one set with the present bulk composition of each rock, which, given microstructural evidence for melt loss discussed in section 3.1.3, will be referred to as residual, and is valid for the evolution of the rocks after melt loss (metamorphic peak and retrograde portion of the *P–T* path), and a second set with melt reintegrated bulk compositions, to calculate topologies before melt loss (prograde portion of the *P–T* path). All pseudosections were calculated in the *P–T* range of 700–940 °C and 5–14 kb. Each field is labelled by its characteristic phases, and the mineral abbreviations used are those produced by THERMOCALC (see Fig. 5.2)

5.1.1 P–T pseudosections calculated with residual bulk compositions.

In these *P–T* pseudosections, quartz, K-feldspar and garnet are stable in every field (Fig 5.2a, b). The field representing the peak assemblage of g + bi + pl + ksp + sill+ q (referred to from now on as main field) is limited at low *T* by the dry solidus and at high *T* by the biotite-out line, with both lines having a sub-vertical dP/dT gradient. Here 'dry' refers to the solidus of the residual bulk composition.

The *T* range and location of the main field are related to the amount of biotite and the X_{Mg} of the rock (Indares et al., 2008). This field is a few tens of degrees wide, from 830 to 870°C in the biotite-richer and low $X_{Mg,}$ HJ-60 (Fig. 5.2a), and narrower and at higher *T* (890 to 903°C) in the biotite-poor and high X_{Mg} 12-AI-10Y(Fig. 5.2b). For both bulk compositions, the main field is delimited at lower *P* by the cordierite-in line and at higher *P* by the kyanite–sillimanite transition line, ranging from~6 to 12 kb.

Isopleths for X_{Fe} (Fe/ (Fe+Mg)) and z(g) (grossular) of garnet were generated inside the main field. X_{Fe} decreases with increasing *T* and shows a positive, steep *dP/dT* gradient. Grossular isopleths have a flat *dP/dT* gradient and increasing values with increasing *P*. Isomodes for garnet and sillimanite were also produced, they display a steep *dP/dT* gradient, and show an increase and decrease as *T* rises, respectively.

5.1.2 Melt reintegrated P–T pseudosections

In addition to microstructural evidence, the sub-vertical dP/dT gradient of the dry solidus and the lack of stable muscovite in the subsolidus topology of the residual pseudosections, are consistent with melt loss during the prograde evolution of these rocks (see also White and Powell, 2002). Therefore, the subsolidus topology of these pseudosections is not valid. However, it is possible to calculate a pre-melt loss bulk rock composition by adding melt to the measured, residual bulk rock composition. The composition and amount of the assumed lost melt were calculated following the procedure outlined in Lasalle and Indares (2014) and Indares et al. (2008), for a scenario of melt loss in one step. The melt composition was calculated at the intersection of the solidus and the z (g) isopleth corresponding to the grossular content of the garnet core in each sample (Grs 3.1% and 3.5% for HJ-60c and 12-AI-10Y, respectively). This is inferred to represent the *P–T* conditions at which the prograde *P–T* path crosses the dry solidus. Then, an amount of that melt sufficient to stabilize the wet solidus at 8 kb (see Lasalle et al., 2013), was added to the residual bulk composition (29% for HJ-60C and 45% for 12-AI-10Y). Although it is impossible to know the exact melt loss history (including the number of steps and *P–T* conditions and amount and composition of the removed melt at each step, forward modelling has inferred that suprasolidus topologies do not change significantly in different scenarios of melt loss (White and Powell, 2002). Therefore, melt-reintegrated *P–T* pseudosections provide a reasonable framework to assess the prograde evolution of anatectic rocks.

The melt reintegrated pseudosections for the two samples are shown in Figures 5.2c, d, together with z(g) isopleths and aluminum silicate and liquid isomodes. The dry solidus line from the residual pseudosections was added as a reference line. The topologies at *T* above the dry solidus barely change in both scenarios, whereas new topologies are generated at lower *T*. For instance, muscovite appears as a stable phase in a number of fields and garnet is not stable in every field. In 12-AI-10Y the muscovite-out line almost coincides with the sillimanite-in line, meaning that along the prograde *P–T* path, aluminum silicate is first produced by the muscovite dehydration reaction [R1]. However, in HJ-60C, the muscovite-out line is decoupled from the sil-in line, and sillimanite is stable with muscovite at *P–T* conditions below those of [R1]. The main assemblage field is expanded towards lower *P–T* conditions, with the garnet-in line delimiting at low *T* and the cordierite-in line at low *P*.

5.1.3 P–T path constraints

In the framework of *P–T* pseudosections, *P–T* paths can be determined based on the observed mineral assemblages, microstructures, and mineral composition data. In anatectic rocks, the microstructures are particularly important due to the high probability of diffusion and resetting of the mineral composition in high-*T* rocks at the peak and during cooling (Powell and Holland, 2008; Spear and Florence, 1992). Concerning mineral chemistry Ca in garnet has a slower diffusion compared to Fe and Mg (Chakraborty and Ganguly, 1992), therefore, intersections between z(g) isopleths and relevant phase boundaries, can be used to constrain specific points on a *P–T* path.

The intersection between the biotite-out line and the z(g) corresponding to the grossular content of the core of the larger garnets (Grs 3.1% and 3.5% for the PLV1 and PLV2, respectively) was selected as a point reference for the *P–T* conditions of the metamorphic peak since it is assumed that the core composition has homogenized close to the metamorphic peak. This would represent the maximum *T* conditions, if biotite is stable at the thermal peak, or minimum peak *T* conditions, if biotite was eliminated during dehydration melting by reaction [R2], and all the biotite present in the rocks was formed during retrograde melt crystallization. The microstructures observed in the modelled samples are consistent with the second scenario, as biotite is only observed as small grains, mostly concentrated in garnet replacement sites (see Chapter 3, Fig. 3.3a,d). In addition, the intersection of the z(g) corresponding to the grossular content of garnet rims with the dry solidus was used to determine the *P–T* conditions of melt crystallization. Therefore, using the distribution of the z(g) isopleths the apparent retrograde *P–T* path down to the dry solidus was delineated in the field of the main assemblage q+ksp+g+bi+pl+sill+liq.

The prograde part of the *P–T* path was constrained considering the presence of kyanite in the rocks. The proportion of kyanite is small compared to the amount of prograde sillimanite present in the rock. Considering that the muscovite-out reaction produces most of the aluminum silicate, it was inferred that a portion of the prograde *P–T* path passes through the muscovite-out line very close to the kyanite-sillimanite univariant line (Fig. 5.2).

Regarding the *P–T* conditions indicated below; it is important to make a comment on the uncertainties on the location of the different lines of interest in the pseudosections. Error-propagation calculations using THERMOCALC for the location of key isopleths and isomodes are derived from uncertainties on the end-member properties, and give two-sigma errors of: 12° to 16° for the dry solidus and the biotite-out line, and 0.2–0.4 kb for z(g) (e.g. Indares et al., 2008) However, these errors do not take into account uncertainties on the $(a-x)$ relations, which are not quantifiable (White et al., 2007; Coggon and Holland, 2002; and Holland and Powell, 2003). Therefore, even though phase equilibria modelling is a powerful tool to investigate the *P–T* evolution of high-grade metamorphic rocks, the information provided by it has to be taken as semi-quantitative.

According to the inferred *P–T* path (Fig. 5.2, c,d), the prograde portion shows a moderate *dP/dT* gradient with peak conditions for sample HJ-60C of PLV1, at ~10.6 kb and 860 °C. The isopleth corresponding to the grossular content in the rims of garnet (Grs 2.1%) intersects the dry solidus at ~8.3 kb and 833 °C, which indicates cooling of 27°C and decompression of ~2.8 kb between the biotite-out line and the dry solidus. Regarding the *P–T* path of the PLV2 sample, 12-AI-10Y, its prograde part has a moderate *dP/dT* gradient, consistent with that of the PLV1, with peak conditions at ~10.7 kb and 903°C. The grossular isopleth (Grs 2.8) intersects the dry solidus at 9.3 kb and 892 °C, implying cooling of 10°C and decompression of 0.8 kb between the biotite-out line and the dry solidus. The difference in *T* between the minimum peak and the recorded retrograde conditions in both rocks is small, because it represents the *T* interval between the biotite-out line and the dry solidus. The inferred retrograde portion of the *P–T* path, has an overestimated *dP/dT* gradient if, as suggested by the observed microstructures, that all biotite present now is retrograde and peak *T* metamorphic conditions were above those of the biotite stability field.

Given the uncertainties on the *T* of the thermal peak, it is not clear whether there was any difference on the peak *P–T* conditions between the PLV2 and PLV1 rocks. In addition, these results are broadly consistent with the *P–T* paths interpreted for the mid-*P* rocks including a PLV1 sample by Lasalle and Indares (2014) where they constrained peak conditions of the mid-*P* rocks at ~9.5 kb and 850 °C, and cooling down to ~8 kb and 820 °C.

5.1.4 P–T pseudosections of HAF and high-P aluminous rocks

Pseudosections for the HAF and aluminous rocks from the high-*P* belt were recreated from the literature (Fig. 5.3) (Lasalle and Indares, 2014; Indares et al. 2008; Kendrick and Indares, 2018b). Comparable with those of the mid-*P* PLV rocks, these *P–T* pseudosections also show the appearance of muscovite at lower pressure once melt is added back to the system, whereas garnet, aluminum silicate, and K-feldspar are not stable at lower *T* at variable *P* conditions. Topologies at higher temperatures do not have major changes, the biotite-out line remains at the same *T,* and the plagioclase-out line varies from sample to sample.

5.2 Modelled Melt Compositions

The compositions of melts potentially produced by the PLV aluminous rocks, the HAF and aluminous rocks from the high-P belt, were modelled with THERMOCALC. The calculated melt compositions were compared with the compositions of the PLV granites and leucocratic layers associated with the metapelites in the PLV.

Two scenarios were modelled. First using the melt reintegrated composition, melt was calculated at three different *P–T* points: at the wet-solidus, muscovite-out and biotite-out lines.

This is equivalent to a closed-system, where the generated melt remains in the rock and the melt continues to equilibrate with the residue along the *P–T* path. Second, using the bulk composition of the actual rock (residual), melt was calculated at the dry solidus and at the biotite-out line. This represents an advanced stage of an open-system (referred to from now on as open-system), where, as the melt is produced, a portion of it migrates out of the rock.

When melting begins, melt pockets are formed at grain boundaries. As *T* rises and melting progresses these pockets connect and form a network, approximately at 7% of produced melt, making the rock permeable and allowing the melt to flow into, through and out of the rock (Sawyer, 1994). In most natural settings the open system case is more realistic, and the two-system approach followed here is based on the following premises: (a) the starting material is residual rocks, which are more appropriate for modelling the advanced stages of an open system; and (b) any differences in melt productivity and composition between open and closed systems would increase with increasing *T* (eg. Yakumchuk and Brown, 2014; Pavan et al., 2021), therefore the composition and evolution of earlier melts (at the wet solidus and at the muscovite-out line) can still be addressed by the closed system modelling.

The *P–T* points selected to calculate the melt compositions were chosen according to the inferred *P–T* path for each sample (Table 5.2). Specific *P* values were selected at the solidus, biotite-out and muscovite-out lines since these represent the most critical melting reactions in aluminous rocks. Along with the melt compositions, the amount of melt produced in each of these points was also calculated. In the closed-system models the amount of melt generated is up to 37.80% in the PLV metapelites, 28.97% in the high-*P* aluminous rocks and 41.81% by the HAF. In open-system models, the last melt produced at the biotite-out line is up to 6.10% by the PLV metapelites, 8.58% by the high-P aluminous rocks and 6.06% by the HAF. This percentage corresponds to the melt that remained in the rock.

The melt composition results are displayed in 3 types of diagrams: (a) those showing variations in major oxides, (b) normative diagrams, and (c) Shand index diagrams. For each type of diagrams, the results of the closed and open system modelling are shown separately. The closed-system ranges are wider than those displayed in the open-system diagrams in every sample, because then open system considered here only represents the highest *T* portion of the melt evolution, at *T* above the dry solidus.

These diagrams also permit comparison of the results with the work done by Pavan et al. (2021), to help assess the progress of the melt compositions produced with the changes in *P–T* conditions. These authors modelled melt compositions generated by greywacke and shale bulk compositions and compared the evolution of these melts through an isobaric *P–T* path with increasing *T*, in closed and open-systems. For comparison with this work, only the melts produced by the shale, up to the biotite-out line, are taking into consideration. Highlighted areas of the melt compositions modelled by Pavan et al. (2021) are superimposed over the diagrams as reference (Fig. 5.4–5.7).

5.2.1 Major oxide diagrams

5.2.1.1 Na_2O vs K_2O (wt%)

At the wet solidus, in the closed-system model, there are two distinct types of melt compositions: (a) Na_2O rich and K_2O -poor (~6–7 wt% and 1–2 wt%, respectively) produced by HJ-60c, 244, 320, and 216c, and (b) K_2O rich (~5. wt%) with lower Na_2O (~4–5 wt%) produced by 12-AI-10Y, and 333x (Fig. 5.4). With increasing *T,* up to the muscovite-out line, there is an increase of K_2O and decrease of Na_2O. This is most marked in the melts that were initially Na_2O rich and K_2O -poor. The same trend is observer at higher *T,* towards the biotite-out line, but with less marked increase in K_2O.

In the open system, the melt produced at the dry solidus is depleted in Na_2O and enriched in K_2O. Similar as the closed-system, as *T* rises, there is an increase in K_2O and a decrease in Na_2O from the solidus to the biotite-out line. The final melt compositions at the biotite-out line are comparable for both systems.

Most of the melt-reintegrated and residual bulk compositions have similar ranges of K_2O and Na_2O, with decreasing K_2O and Na_2O as the system loses melt. However, the hydrothermally altered felsic rocks (HAF) show a different trend. These compositions are the most Na_2O rich, and when melt loss occurs, they show an increase and decrease in K_2O and Na_2O, respectively.

5.2.1.2 $FeO + MgO$ - $Na_2O + CaO$ - K_2O (mol%)

The modelled melt compositions show in general decreasing $Na_2O + CaO$ and increasing K_2O trends from the solidus to the biotite-out line (Fig. 5.5). The composition of the final melt at the biotite-out line is very similar in both models, with a difference of less than 5 % for all the components.

In the closed-system, the melts with the more $Na_2O + CaO$ – rich initial compositions (produced by samples HJ-60c, 244, 320, and 216c) show the strongest increase in K_2O as T increases towards the muscovite-out line, with no change in $FeO + MgO$. Exception are the melts from the high-P rocks, which show a moderate rise in $FeO + MgO$. On the other hand, melts with more K_2O-rich initial compositions (produced by samples 12-AI-10Y and 333x) change only slightly in that interval. Towards the biotite-out line, all the melt compositions display an increase in $FeO + MgO$.

In the open-system, the melt compositions at the dry solidus show intermediate $Na_2O + CaO$ and K_2O proportions (~40–50%) and increase in K_2O as T increases towards the biotite-out line without any significant variation in the $FeO + MgO$ proportion. The composition of the melt at the biotite-out line from both closed, and open-system show comparable values.

The residue compositions are richer in $FeO + MgO$ and have intermediate $Na_2O + CaO$ and K_2O proportions. As the system loses melt, there is a shift to the $FeO + MgO$ component, with a minor increase in K_2O.

*5.2.2 Q–A–P (*wt%)

In these digrams, the modelled melts generally evolve from granodioritic to monzogranitic compositions as the T rises from the solidus to the biotite-out line (Fig. 5.6) and have less than 50% normative quartz. In the closed-system, the richest Na_2O melts at the wet solidus (from HJ-60C, 244, 320, and 216c) show a granodiorite composition. These melts move into the monzogranite field as T reaches the muscovite-out line, with those derived from the high-P aluminous rocks, closer to the boundary between monzogranite and quartz-monzonite. With increasing T towards the biotite-out line, they exhibit and increase in normative quartz and alkali feldspar, while remaining in the monzogranite field. The melts that were initially richer in K_2O (from 12-AI-10Y, and 333x) are already monzogranitic at the wet solidus and remain in that field with only minor increase in normative quartz and alkali feldspar as T increases to the biotite-out line.

In the open-system*,* most of the melt compositions produced at the dry solidus are in the monzogranite field, except for high-P sample 320, which is at the borderline between quartz-monzonite and quartz-monzodiorite. Again, the two high-P samples have lower normative quartz proportions than the rest. At the biotite-out line, the final melt compositions are generally similar in the two systems.

5.2.3 Shand's Index

In the closed-system, the modelled melts at the wet solidus are marginally peraluminous and as T rises towards the biotite-out line, they become increasingly peraluminous (Fig 5.7). However, the melts from the high-P aluminous rocks, remain close to the peraluminous-metaluminous boundary. In the open-system, melt compositions are moderately peraluminous, with a minor change between the dry solidus and the biotite-out line, except for those produced by the high-P rocks, which are close to the peraluminous-metaluminous boundary. For all samples, melt produced at the biotite-out line in the closed and open-system model show comparable compositions.

5.3 Modelled Melts and Comparison with the PLV Granites

5.3.1 Main trends of the modelled melts and comparison with other studies

All modelled melts show a general trend of increasing K_2O and decreasing Na_2O with rising T. Highest Na_2O contents at the wet solidus (Fig. 5.4) are consistent with natural experiments (Johannes and Holts, 1996). If plagioclase is present, its albite component is preferentially incorporated in the melt, and even decreases the onset of anatexis by few tens of degrees (Spear et al., 1999). Then, as anatexis progresses with rising T, Na_2O in the melt decreases because there is a decreasing supply of Na_2O in the residual rock, whereas other components keep on getting added to the melt (e.g., Al_2O_3, FeO, MgO from biotite breakdown; Pavan et al, 2021). In contrast, the increase of K_2O from the solidus to the biotite-out line, in both closed and open-systems, it is attributed to the breakdown of K-rich phases, such as muscovite and biotite. It is noted that modelled melts from the relatively K_2O -rich rocks (12-AI-10Y and 333x; Table 5.1), start at high K_2O contents at the wet solidus compared to the rest and show less increase in K_2O towards the muscovite-out line (Fig. 5.4).

As T increases from the muscovite-out line towards biotite-out line, there is a marked increase in $FeO + MgO$ (Fig. 5.5), consistent with the biotite dehydration melting. However, in the high-P rocks, this change is minor because of the reduced T difference at higher P between the muscovite-out line and the biotite-out line at 15 kb of approximately ~65 °C. This difference is higher than 140 °C in the mid-P settings.

In the normative classification, (Fig. 5.6), all evolved melts (in open and closed systems) are monzogranitic, with normative quartz less than 50%. Main changes in the evolution of melts in this field as T increases are increase in quartz and alkali-feldspar modal proportions. In contrast, earlier melts produced by the relatively K_2O-poor, NaO -rich rocks are granodioritic.

The modelled melt compositions and trends are comparable and fall within the ranges predicted by Pavan et al. (2021). These authors also reported trend of enrichment in K_2O and depletion in Na_2O with increasing T, from the solidus to the biotite-out line (Fig. 5.4), and an increase in $FeO + MgO$ from the muscovite-out line to the biotite-out line (Fig. 5.5). In addition, most of the melt compositions modelled in this study, fall within the field of leucosome compositions from Sawyer (2008), as cited in Pavan et al. (2021), although they are located on the low normative quartz side (Fig. 5.6). In the same manner, they also fall within the range of the peraluminous compositions of Pavan et al. (2021) and show the same trend of increasing peraluminosity at higher T (Fig. 5.7). Exceptions are the melts produced by the high-P rocks, particularly from the sample 320, which are richer in Na_2O than the ones modelled by Pavan et al. (2021).

5.3.2 Comparison with the PLV granites

In Figures 5.4 to 5.7 are also shown the compositions of the PLV granites and leucocratic layers. Generally, they plot close to the melt compositions modelled between the muscovite -out and the biotite-out lines, consistent with these rocks being the migrated product of dehydration melting of micas of aluminous protoliths. The most evolved rock is the PLV1 granite 11-AI-448 which has a composition comparable to those modelled at the biotite-out line and straddles the boundary between monzogranite and syenogranite in Figure 5.6. The rest however exhibit some notable differences with respect to the modelled compositions. For instance, most have slightly lower Na_2O and K_2O (Fig. 5.4) and slightly higher $FeO + MgO$ proportions (Fig. 5.5). These differences are more marked in PLV2 granite 12-AI-20 (and, in terms of $FeO + MgO$), in leucocratic layer AI-08-62b. In terms of modal mineralogy, they fall in the monzogranite field, but they are distinguished from the modelled melts by higher normative quartz.

Figures Chapter 5

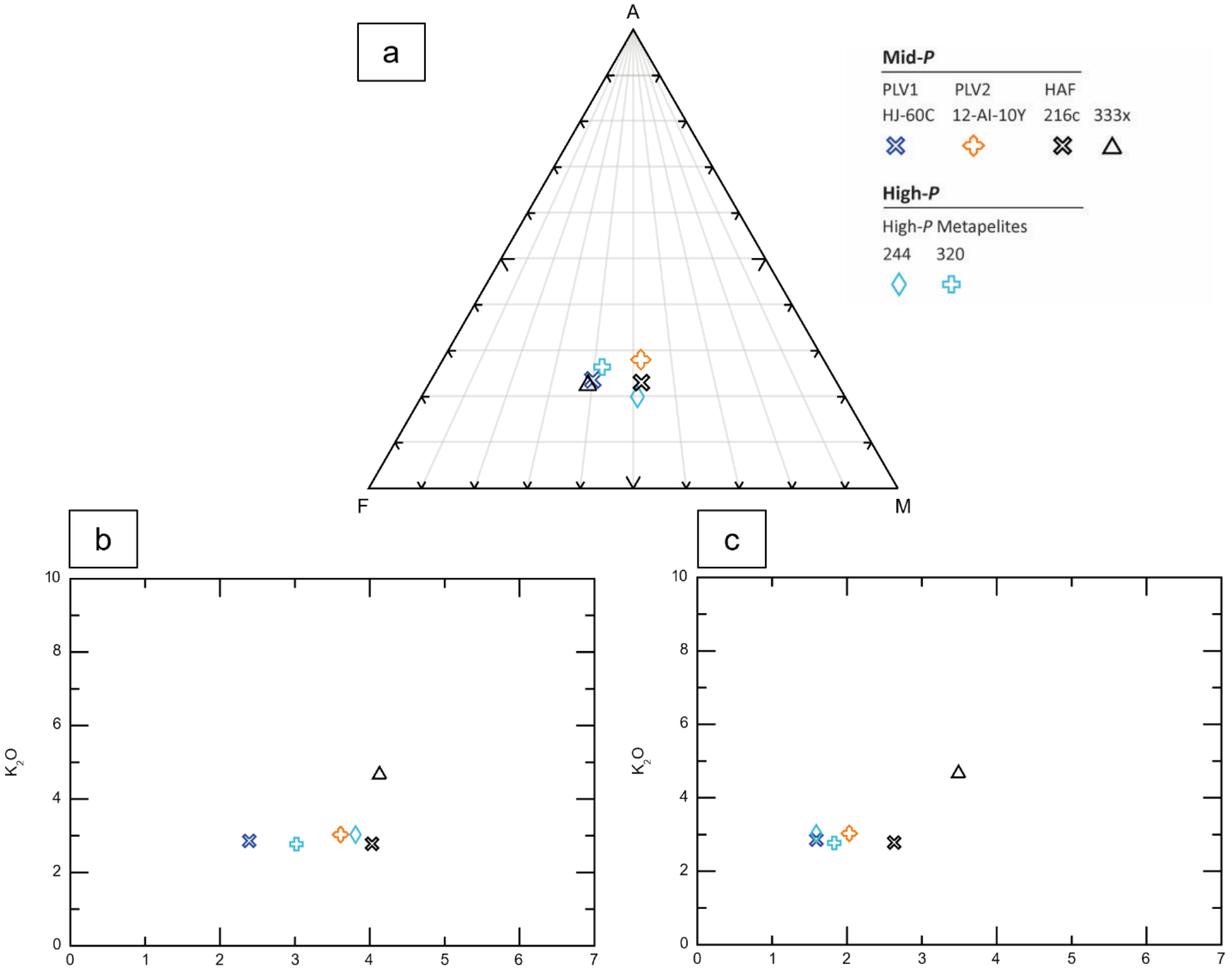

Figure 5.1 Residual bulk compositions of the PLV metapelites, hydrothermally altered felsic rocks (HAF) and high-*P* aluminous rocks. a) AFM diagram. b) Binary K_2O vs Na_2O diagram. c) Binary K_2O vs $Na_2O + CaO$ diagram.

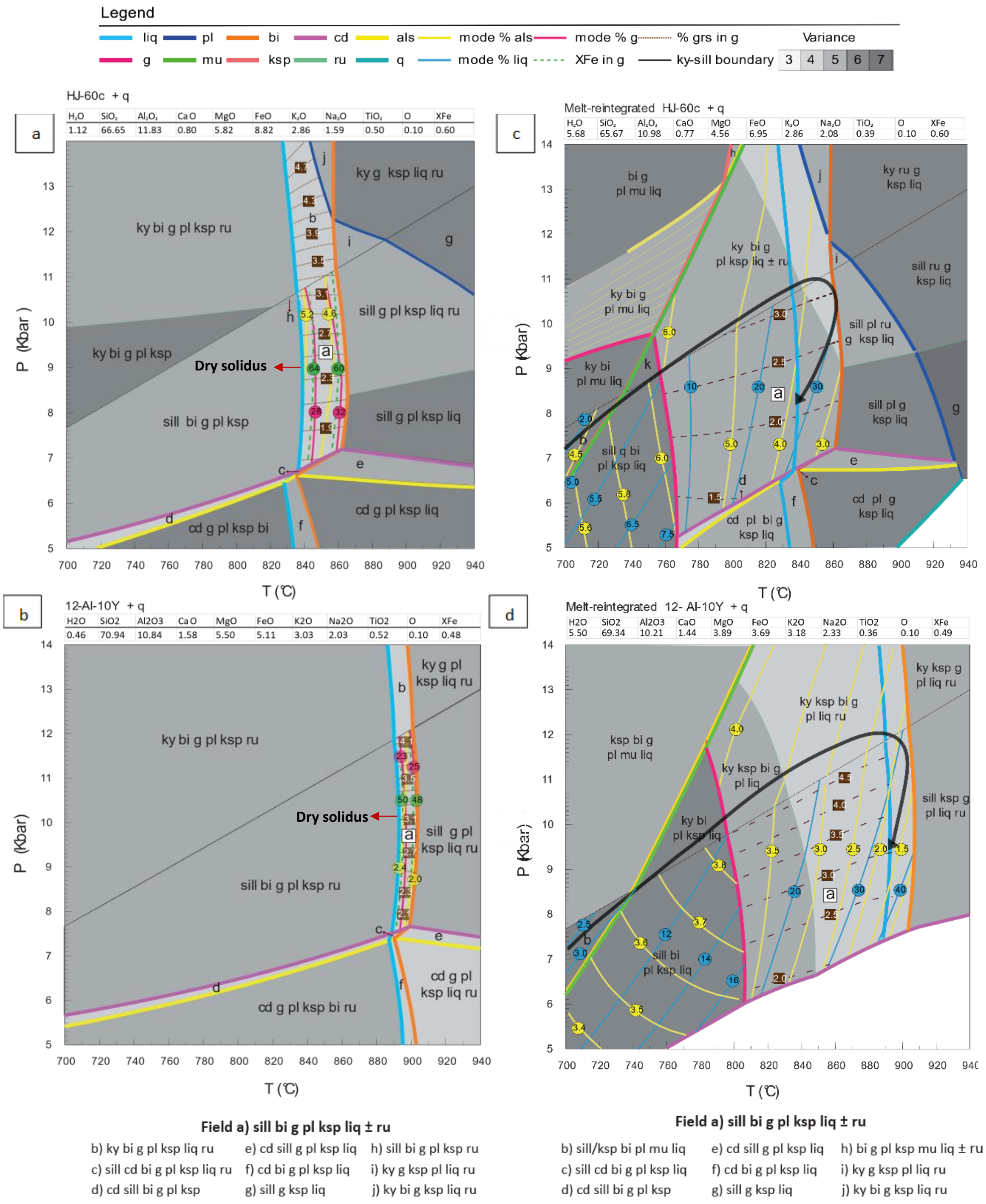

Figure 5.2 NCKFMASHTO *P–T* Pseudosections of (a, b) the PLV residual bulk compositions (mol%), and (c,d) the PLV melt-reintegrated bulk compositions, also showing the inferred *P–T* paths. The blue line represents the dry solidus, added in c and d for reference. The numbers in the circles represent isomode or isopleth values. Mineral abbreviations here are those produced by THERMOCALC: ky, kyanite; sill, sillimanite; g, garnet; b, biotite; mu, muscovite; cd, cordierite; pl, plagioclase; ksp, K-feldspar; q, quartz; ru, rutile; liq, liquid. The black arrow shows the interpreted *P–T* path.

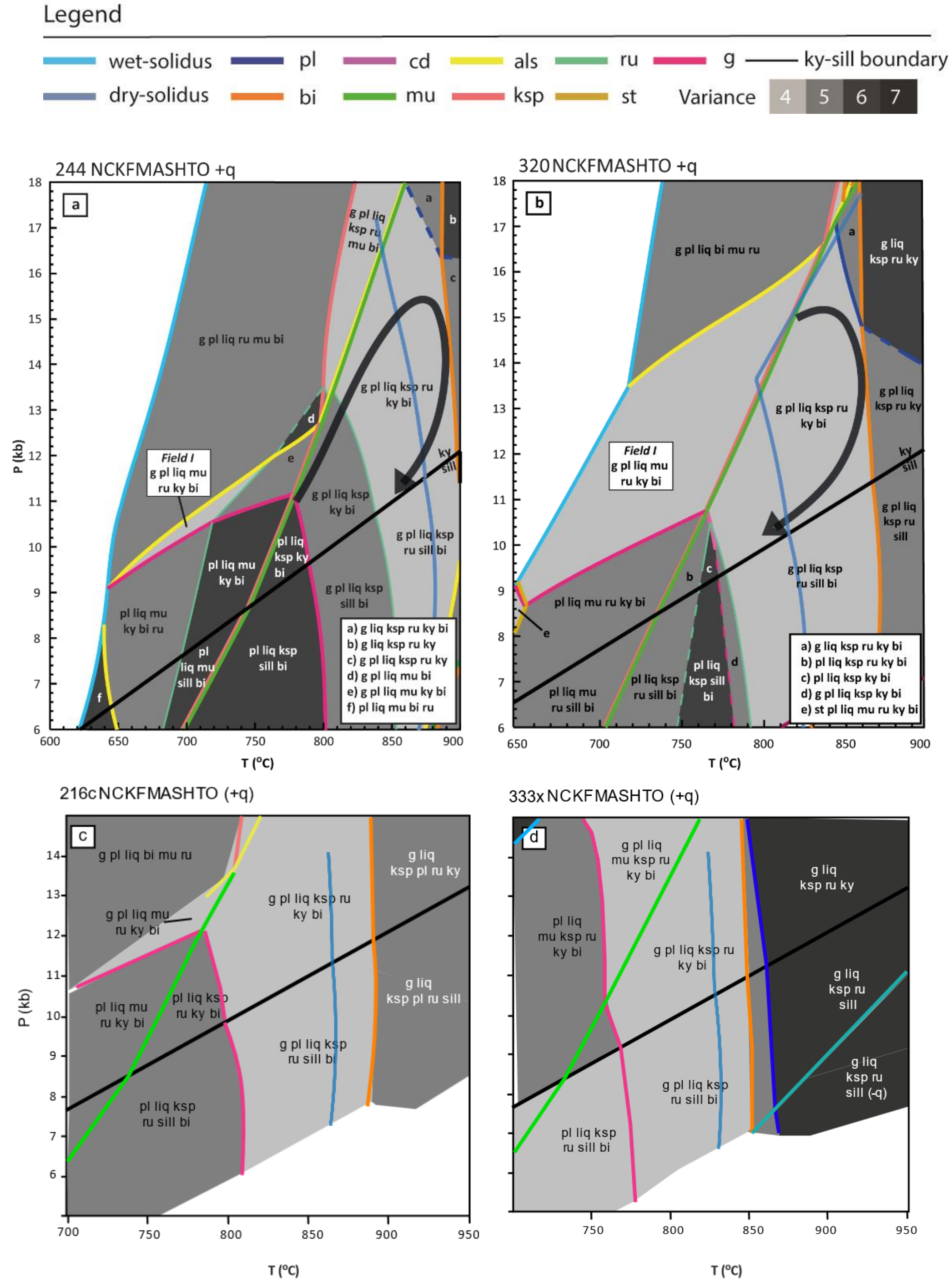

Figure 5.3 *P–T* melt reintegrated Pseudosections of aluminous rocks from the high-*P* belt and their inferred *P–T* path (a, b) and HAF (c, d), with the dry solidus superimposed as reference. Even though *P–T* paths have not been inferred for the mid-*P* belt HAF rocks, microstructures suggest a *P–T* path below the kyanite-sillimanite boundary and above the cordierite field (Kendrick, 2018; Lasalle, 2014).

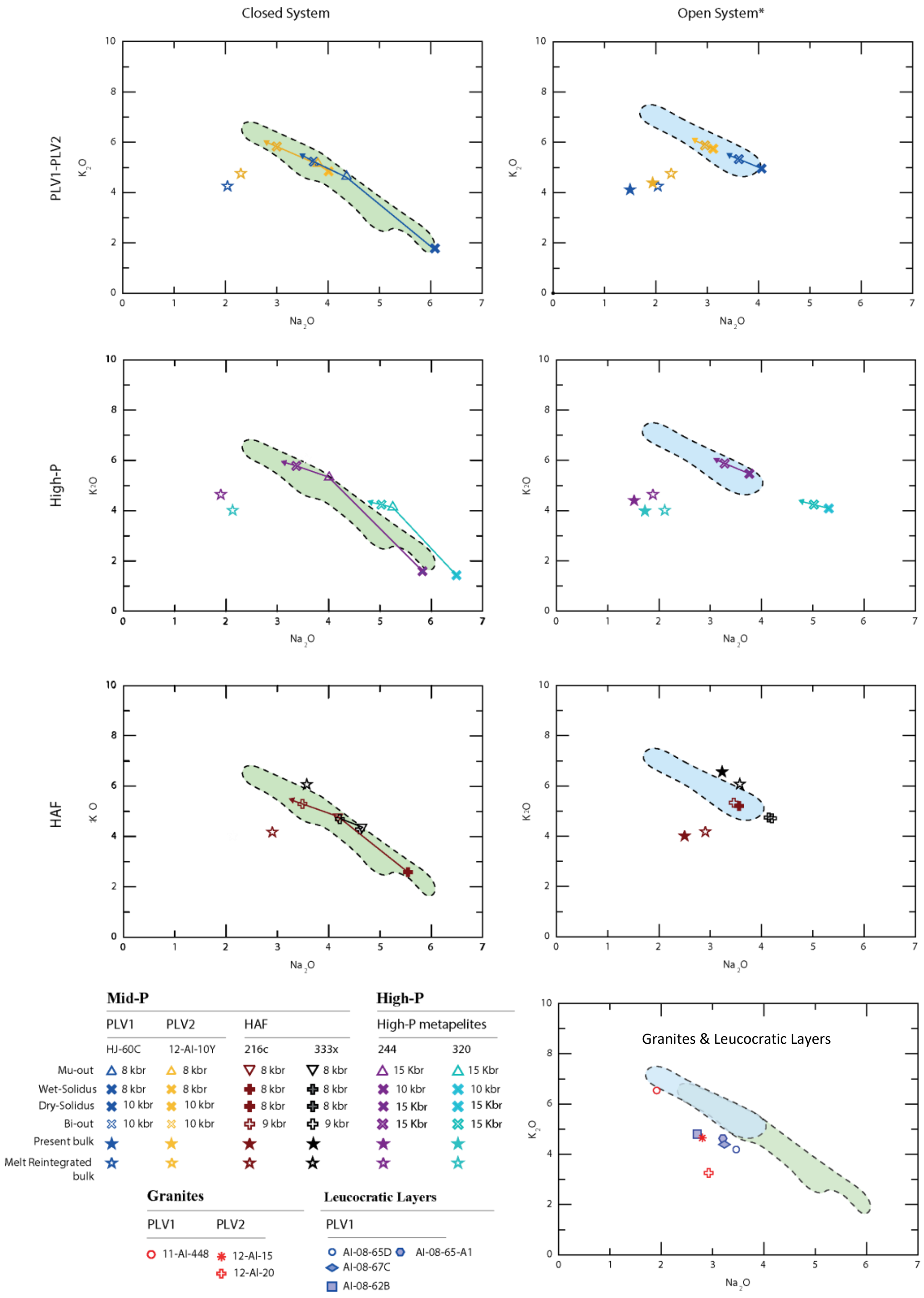

Figure 5.4 Binary Na_2O vs K_2O in wt% of the calculated melts. The residual bulks, melt reintegrated bulks, granites and leucocratic layers compositions are also added for reference. *Open-system: Melts calculated with the present bulk composition, from the dry solidus to the biotite-out line. Green and blue colored areas represent range of the results from Pavan et al, 2021.

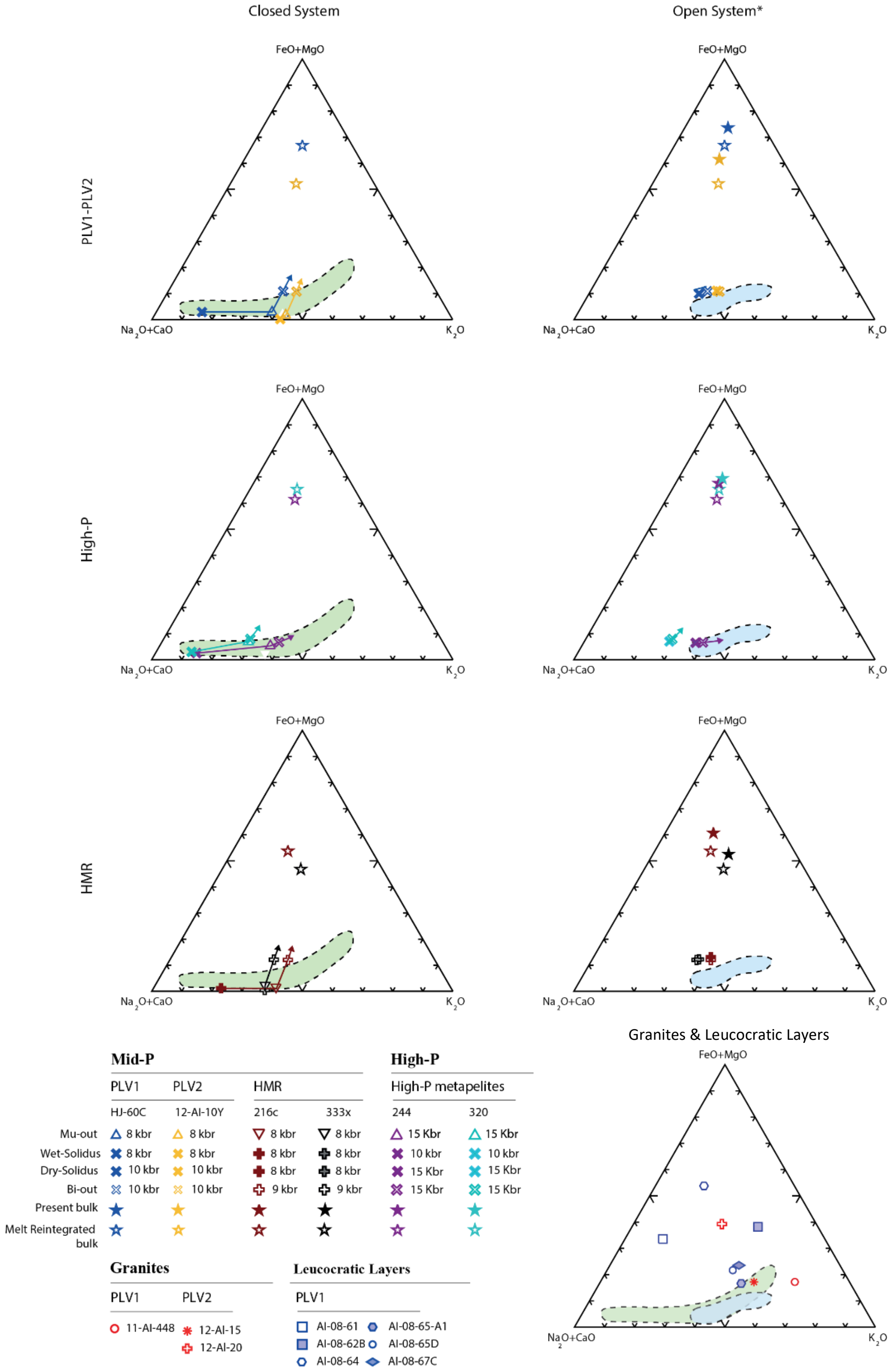

Figure 5.5 Ternary $FeO + MgO$ - $Na_2O + CaO$ - K_2O (mol%) of the calculated melts. The residual bulks, melt reintegrated bulks, granites and leucocratic layers compositions are also added for reference. *Open-system: Melts calculated with the present bulk composition, from the dry solidus to the biotite-out line. Green and blue colored areas represent range of the results from Pavan et al, 2021.

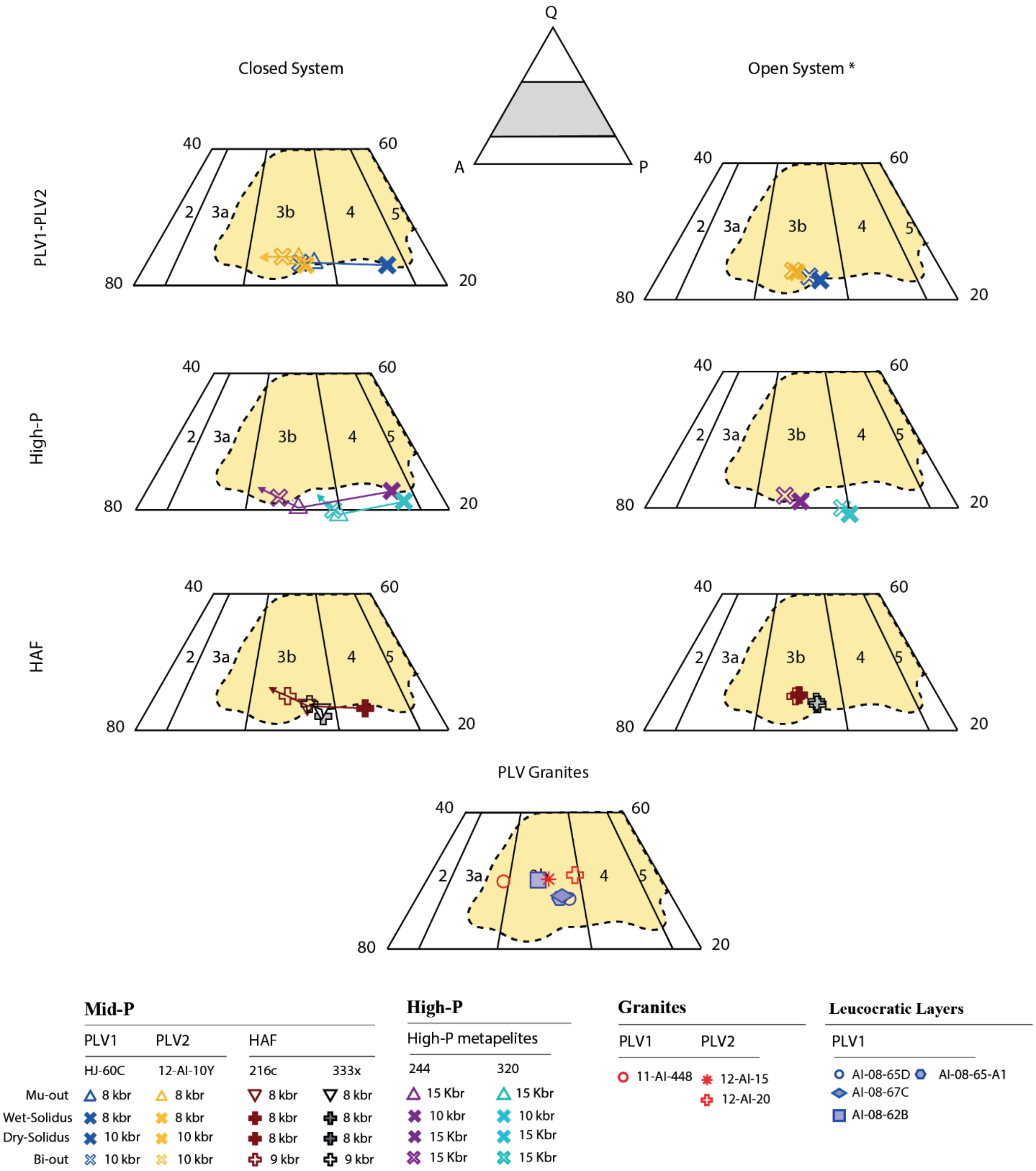

Figure 5.6 Q–A–P diagram (wt%) of the calculated melts. The residual bulks, melt reintegrated bulks, granites and leucocratic layers compositions are also added for reference. *Open-system: Melts calculated with the present bulk composition, from the dry solidus to the biotite-out line. Yellow areas represent the field of leucosome compositions replotted from Sawyer (2008), as cited in Pavan et al., 2021. QAP legend: 2, Alkali-Feldspar Granite; 3a, Syenogranite; 3b, Monzogranite; 4, Granodiorite; 5, Tonalite.

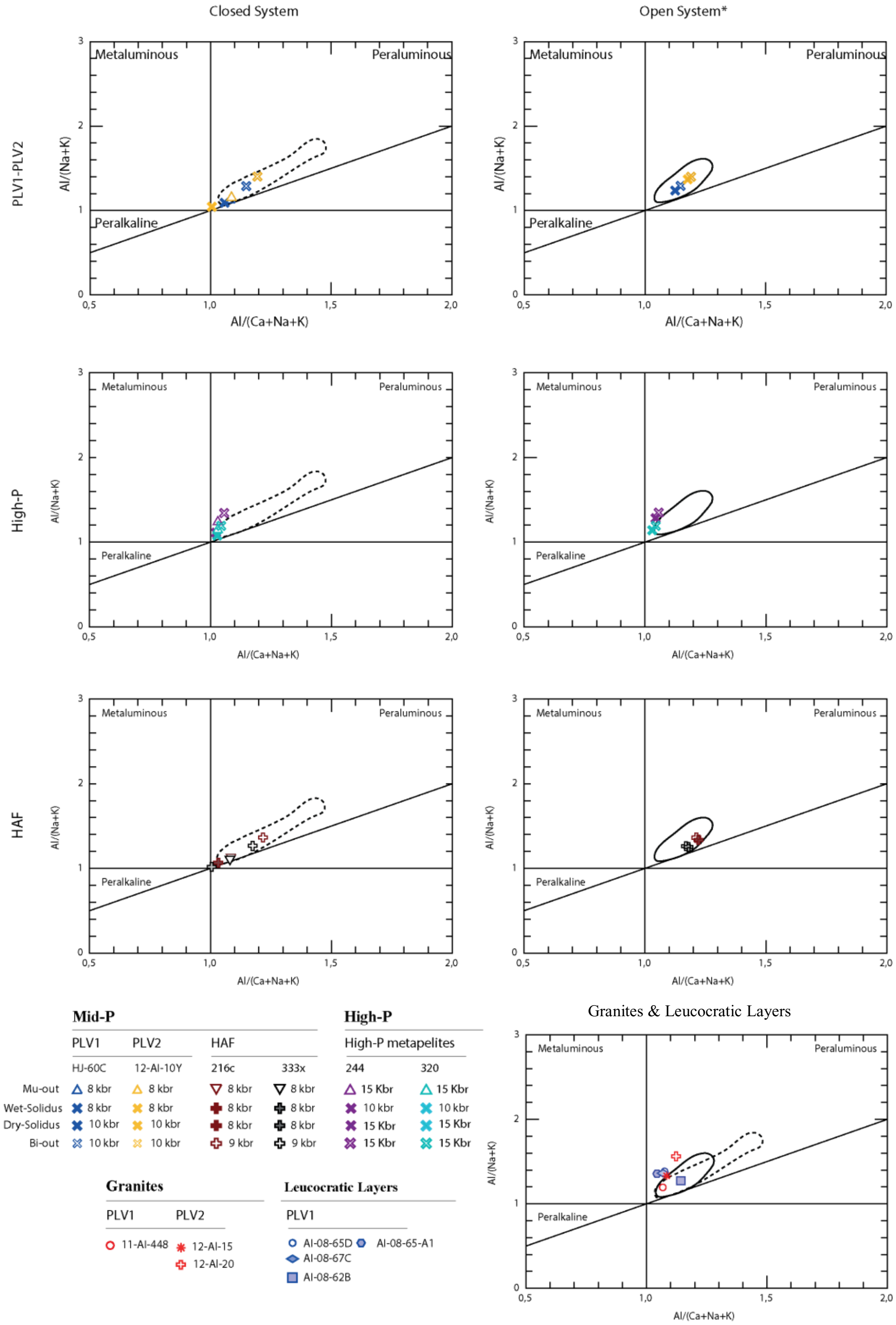

Figure 5.7 Shand's index diagram (wt%) of the calculated melts. The granites and leucocratic layers compositions are also added for reference. *Open-system: Melts calculated with the present bulk composition, from the dry solidus to the biotite-out line. Dotted and solid black line represent results from closed and open system, respectively from Pavan et al., 2021.

Table 5.1

Calculated bulk compositions for the PLV metapelites, hydrothermally felsic rocks (HAF) and the high-P aluminous rocks.

Bulk compositions mol%

Residual Bulk	PLV1	PLV2	HAF		High-P segment	
	HJ-60C	12-AI-10Y	216c	333x	244	320
H20	1.12	0.46	0.87	0.55	1.38	2.15
SiO2	66.65	70.94	69.60	67.37	64.92	64.59
Al2O3	11.83	10.84	11.37	12.74	11.71	13.31
CaO	0.80	1.58	1.29	0.59	2.07	1.13
MgO	5.82	5.50	5.44	3.81	7.32	5.58
FeO	8.82	5.11	5.06	5.92	6.95	7.58
K2O	2.86	3.03	2.78	4.66	3.03	2.77
Na2O	1.59	2.03	2.63	3.49	1.59	1.83
TiO2	0.50	0.52	0.81	0.81	0.63	0.71

Melt-reintegrated Bulk	PLV1	PLV2	HAF		High-P segment	
	HJ-60C	12-AI-10Y	216c	333x	244	320
H20	5.68	5.50	5.93	6.03	6.39	5.99
SiO2	65.67	69.34	67.66	66.12	63.73	63.48
Al2O3	10.98	10.21	10.62	11.51	10.98	12.52
CaO	0.77	1.44	1.29	0.59	2.07	1.13
MgO	4.56	3.89	4.19	2.86	5.77	4.81
FeO	6.95	3.69	3.96	4.50	5.52	6.56
K2O	2.86	3.18	2.78	4.11	3.09	2.72
Na2O	2.08	2.33	2.94	3.68	1.92	2.19
TiO2	0.39	0.36	0.61	0.60	0.49	0.61

Table 5.2a

Calculated melt compositions for the PLV metapelites, hydrothermally altered felsic rocks (HAF) and the high-P aluminous rocks (wt%).

Calculated Melt compositions - Closed System

			melt %	P (Kbr)	T (C°)	H20	SiO2	AL2O3	CaO	MgO	FeO	K2O	Na2O	TiO2	Total
PLV	HJ-60C	Liq-in	0.00	8	663	13.80	64.90	13.01	0.20	0.03	0.20	1.78	6.08	0.00	100.00
		Mu-out	5.03	8	728	9.22	67.59	13.70	0.26	0.03	0.21	4.64	4.36	0.00	100.00
		Bi-out	31.13	10	863	5.75	68.37	15.17	0.79	0.20	0.77	5.23	3.72	0.00	100.00
	12-Al-10Y	Liq-in	0.00	8	635	13.71	64.81	12.36	0.25	0.00	0.02	4.84	4.01	0.00	100.00
		Mu-out	10.36	8	732	9.12	67.76	13.64	0.40	0.02	0.11	5.15	3.80	0.00	100.00
		Bi-out	37.80	10	907	4.43	68.96	15.77	1.08	0.24	0.69	5.83	3.00	0.00	100.00
High-P	244	Liq-in	0.00	10	649	17.72	61.51	12.59	0.55	0.03	0.16	1.59	5.83	0.00	100.00
		Mu-out	16.13	15	826	9.58	63.94	15.28	1.36	0.10	0.41	5.32	4.01	0.00	100.00
		Bi-out	28.97	15	891	7.15	65.46	15.85	1.76	0.17	0.46	5.78	3.37	0.00	100.00
	320	Liq-in	0.00	10	666	15.73	62.60	13.17	0.32	0.04	0.21	1.43	6.49	0.00	100.00
		Mu-out	16.68	15	821	9.90	64.24	15.01	0.80	0.12	0.55	4.14	5.25	0.00	100.00
		Bi-out	23.90	15	862	8.38	65.26	15.33	1.00	0.17	0.60	4.24	5.03	0.00	100.00
HAF	216c	Liq-in	0.00	8	660	13.78	65.08	12.71	0.22	0.02	0.08	2.58	5.55	0.00	100.00
		Mu-out	11.10	8	729	9.20	67.68	13.69	0.30	0.02	0.11	4.80	4.18	0.00	100.00
		Bi -out	41.81	9	896	4.32	69.40	15.67	0.77	0.27	0.77	5.30	3.49	0.00	100.00
	333x	Liq-in	0.00	8	623	14.15	64.36	12.46	0.10	0.00	0.03	4.29	4.61	0.00	100.00
		Mu-out	12.23	8	725	9.30	67.54	13.74	0.18	0.02	0.18	4.38	4.65	0.00	100.00
		Bi -out	35.43	9	862	5.32	68.96	15.20	0.51	0.22	0.87	4.69	4.22	0.00	100.00

Calculated Melt compositions - Open System

			melt %	P (Kbr)	T (C°)	H20	SiO2	AL2O3	CaO	MgO	FeO	K2O	Na2O	TiO2	Total
PLV	HJ-60C	Liq-in	0.00	10	838	6.57	68.00	14.88	0.65	0.16	0.73	4.96	4.06	0.00	100.00
		Bi-out	6.10	10	863	5.75	68.36	15.16	0.82	0.20	0.77	5.33	3.62	0.00	100.00
	12-Al-10Y	Liq-in	0.00	10	893	4.83	68.77	15.55	1.02	0.23	0.74	5.75	3.12	0.00	100.00
		Bi-out	3.10	10	904	4.52	68.91	15.71	1.08	0.24	0.70	5.88	2.96	0.00	100.00
High-P	244	Liq-in	0.00	15	859	8.32	64.75	15.54	1.53	0.14	0.48	5.47	3.76	0.00	100.00
		Bi-out	6.27	15	890	7.14	65.42	15.87	1.79	0.17	0.45	5.88	3.28	0.00	100.00
	320	Liq-in	0.00	15	820	9.91	64.25	15.00	0.77	0.12	0.55	4.09	5.31	0.00	100.00
		Bi-out	8.58	15	861	8.41	65.22	15.34	1.01	0.17	0.60	4.24	5.02	0.00	100.00
HAF	216c	Liq-in	0.00	8	872	4.44	69.66	15.38	0.61	0.26	0.88	5.21	3.56	0.00	100.00
		Bi-out	6.06	9	894	4.38	69.38	15.63	0.78	0.27	0.77	5.34	3.46	0.00	100.00
	333x	Liq-in	0.00	8	841	5.34	69.29	14.98	0.42	0.20	0.90	4.74	4.14	0.00	100.00
		Bi-out	3.19	9	859	5.40	68.92	15.16	0.52	0.21	0.86	4.72	4.20	0.00	100.00

Note: *Open-system: Melts calculated with the present bulk composition, from the dry solidus to the biotite-out line. Melt% is given in mode%.

Table 5.2b

Calculated melt compositions for the PLV metapelites, hydrothermally altered felsic rocks (HAF) and the high-P aluminous rocks (mol%).

Calculated Melt compositions - Closed System

			melt %	P (Kbr)	T (C°)	H20	SiO2	AL2O3	CaO	MgO	FeO	K2O	Na2O	TiO2	Total
PLV	HJ-60C	Liq-in	0.00	8	665	36.50	51.50	6.08	0.17	0.04	0.13	0.90	4.68	0.00	100.00
		Mu-out	5.03	8	728	26.96	59.24	7.07	0.24	0.04	0.15	2.59	3.70	0.00	100.00
		Bi-out	31.13	10	863	18.22	64.98	8.50	0.80	0.29	0.61	3.17	3.42	0.00	100.00
	12-Al-10Y	Liq-in	0.00	8	635	36.56	51.81	5.82	0.22	0.00	0.01	2.47	3.10	0.00	100.00
		Mu-out	10.36	8	732	26.74	59.59	7.07	0.38	0.03	0.08	2.89	3.24	0.00	100.00
		Bi-out	37.80	10	907	14.53	67.78	9.13	1.13	0.35	0.57	3.66	2.86	0.00	100.00
High-P	244	Liq-in	0.00	10	685	43.62	45.40	5.48	0.44	0.04	0.10	0.75	4.17	0.00	100.00
		Mu-out	16.13	15	826	27.99	56.03	7.89	1.28	0.13	0.30	2.97	3.40	0.00	100.00
		Bi-out	28.97	15	891	22.05	60.55	8.64	1.74	0.23	0.36	3.41	3.02	0.00	100.00
	320	Liq-in	0.00	10	666	40.16	47.94	5.94	0.26	0.05	0.13	0.70	4.82	0.00	100.00
		Mu-out	16.68	15	821	28.62	55.71	7.67	0.74	0.15	0.40	2.29	4.41	0.00	100.00
		Bi-out	23.90	15	862	25.04	58.45	8.09	0.96	0.22	0.45	2.42	4.36	0.00	100.00
HAF	216c	Liq-in	0.00	8	660	36.51	51.71	5.95	0.19	0.02	0.05	1.31	4.27	0.00	100.00
		Mu-out	11.10	8	729	26.92	59.36	7.08	0.29	0.03	0.08	2.69	3.56	0.00	100.00
		Bi -out	41.81	9	896	14.18	68.25	9.08	0.81	0.39	0.63	3.33	3.33	0.00	100.00
	333x	Liq-in	0.00	8	623	37.38	50.99	5.81	0.08	0.01	0.02	2.17	3.54	0.00	100.00
		Mu-out	12.23	8	725	27.14	59.07	7.08	0.17	0.03	0.13	2.45	3.94	0.00	100.00
		Bi -out	35.43	9	862	17.01	66.09	8.58	0.52	0.31	0.70	2.87	3.92	0.00	100.00

Calculated Melt compositions - Open System

			melt %	P (Kbr)	T (C°)	H20	SiO2	AL2O3	CaO	MgO	FeO	K2O	Na2O	TiO2	Total
PLV	HJ-60C	Liq-in	0.00	10	838	20.41	63.37	8.17	0.65	0.23	0.57	2.95	3.66	0.00	100.00
		Bi-out	6.10	10	863	18.24	64.98	8.49	0.83	0.29	0.61	3.23	3.33	0.00	100.00
	12-Al-10Y	Liq-in	0.00	10	893	15.66	66.92	8.92	1.06	0.34	0.60	3.57	2.94	0.00	100.00
		Bi-out	3.10	10	904	14.78	67.59	9.08	1.14	0.35	0.57	3.68	2.82	0.00	100.00
High-P	244	Liq-in	0.00	15	859	24.99	58.31	8.25	1.48	0.19	0.36	3.14	3.28	0.00	100.00
		Bi-out	6.27	15	890	22.04	60.54	8.65	1.78	0.23	0.35	3.47	2.94	0.00	100.00
	320	Liq-in	0.00	15	820	28.64	55.70	7.66	0.72	0.16	0.40	2.26	4.46	0.00	100.00
		Bi-out	8.58	15	861	25.11	58.39	8.09	0.97	0.22	0.45	2.42	4.36	0.00	100.00
HAF	216c	Liq-in	0.00	8	872	14.51	68.24	8.88	0.64	0.38	0.72	3.26	3.38	0.00	100.00
		Bi-out	6.06	9	894	14.34	68.14	9.04	0.82	0.39	0.63	3.34	3.29	0.00	100.00
	333x	Liq-in	0.00	8	841	17.06	66.33	8.45	0.43	0.28	0.72	2.89	3.84	0.00	100.00
		Bi-out	3.19	9	859	17.24	65.92	8.55	0.53	0.31	0.69	2.88	3.89	0.00	100.00

Note: *Open-system: Melts calculated with the present bulk composition, from the dry solidus to the biotite-out line.

6 CHAPTER 6: Discussion and Conclusions

The Grenville Province is a Mesoproterozoic large hot orogen with widespread exposures of granulite facies rocks and migmatites. Aluminous rocks in the hinterland of the central Grenville Province experienced partial melting and melt escape during the Ottawan phase of the Grenvillian orogeny (Lasalle and Indares, 2014), but the fate of the migrated melt remained unclear. This study explored the links between anatexis of metapelites from the central Grenville Province, mostly from the PLV metasedimentary sequence of the mid-*P* belt, and biotite-garnet bearing granitic rocks of potential anatectic origin from the PLV area. The melt productivity of the metapelites of the PLV and correlations between the presumed migrated melt and the granitic rocks were assessed by documentation of microstructures, phase equilibria modelling, and geochemistry and monazite dating of granites.

6.1 Anatectic and *P–T* Record of the Aluminous Rocks

The examined metapelites of the PLV come from 2 locations, PLV1 and PLV2, separated by about 50 km. In both cases they have the mineral assemblage quartz, garnet, K-feldspar, plagioclase, biotite, and sillimanite (with, locally, relict kyanite in PLV1 samples), which is consistent with dehydration melting of biotite (Spear et al., 1999). In addition, the presence of former melt domains is suggested by observed microstructures, and good preservation of the peak assemblage is consistent with melt-loss from the source rock, leaving behind less material for retrograde reactions during melt crystallization (Jones and Brown, 1990; Sawyer, 1999; Holness and Sawyer, 2008; Holness, 2008; Sawyer, 2001; Vernon 2011).

Results from mineral chemistry microstructural observations, and phase equilibria modelling, suggest *P–T* paths with moderate dP/dT gradients, peak *P–T* conditions of about 10.6–10.7 kb and 860–903 °C, and melt crystallization at 8.3–9.3 kb and 833–892 °C. For the proposed prograde *P–T* path the presence of kyanite in the PLV1 rocks was taken into account. The absence of kyanite in the examined samples from the PLV2 is likely due to differences in bulk compositions that prevented early formation of Al-silicate in the latter case, or limited amount of sampling from this area. Inferred *P–T* paths in PLV1 and PLV2 are broadly similar, and consistent with a *P–T* path previously proposed for PLV1 by Lasalle and Indares (2014), with peak conditions at ~9.5 kb and 850 °C and a retrograde portion down to ~8kb and 820°C.

Similar microstructures to those of the PLV metapelites were also reported from aluminous rocks derived from hydrothermally altered felsic (HAF) protoliths in the mid-P belt farther north, and also from aluminous rocks of uncertain affiliation, from the structurally lower high-P belt, the latter having kyanite instead of sillimanite. (Kendrick and Indares, 2018; Lasalle and Indares, 2014). Based on $P–T$ pseudosection topologies, $P–T$ paths for the HAF rocks are inferred to be broadly similar to those of the PLV, but are less well constrained (Lasalle and Indares, 2014). In contrast, aluminous rock of the high-P belt record peak conditions of 14–15 kb and ~900°C and $P–T$ paths with stronger pressure variations and a steep dP/dT gradients (Kendrick and Indares, 2018; Lasalle and Indares, 2014).

6.2 Melt Productivity of the Aluminous Rocks and Modelled Melt Compositions

Phase equilibria modelling of the metapelites of the PLV, the HAF rocks, and the high-P aluminous rocks shows that from the 45% of the produced melt, only 6−8% remained in the rock. All modelled melts are peraluminous and with increasing T, from the wet solidus to the muscovite -out and to the biotite-out boundaries on the $P–T$ space their compositions evolve from granodioritic to monzogranitic. The composition of the modelled melts and their evolution with increasing T are comparable with the results of the modelling of shales by Pavan et al. (2021). Early melts produced in closed and open systems are richer in Na_2O than K_2O, and as the system evolves, the proportion of K_2O increases due to the breakdown K bearing phases, in this case, muscovite and biotite. In addition, there is a notable increase in $FeO + MgO$ when biotite starts melting.

6.3 Granites and Leucocratic Layers

The PLV granite bodies and leucocratic layers associated with the metapelites, have minor amounts of garnet associated with biotite and locally sillimanite. Based on microstructures, garnet in the leucocratic layers is inferred to have mostly grown peritectically in the source and then entrained in the migrating anatectic melt. In contrast, in the granites garnet is suggested to have crystallized directly from melt. The PLV granites and most of the leucocratic layers show peraluminous, monzogranitic compositions, consistent with the modelled melts.

In the PLV granites, monazite morphologies suggest growth in the presence of melt and resorption, the different chemical zones in the core of some monazite grains also indicate different growth and resorption episodes. Even though the Th and Y contents are variable and hard to directly correlate to different stages, the high Y content of the monazite with idiomorphic rims, suggest growth of monazite during melt crystallization (Kohn, 2016).

The monazite ages of the PLV granites are dominantly Ottawan, and similar to the metamorphic ages, also obtained by monazite, from the mid-*P* metapelites of the PLV (1.08 – 1.04 Ga, Dunning and Indares, 2010; Lasalle et al., 2014). This is shown in the main clusters of monazite ages from the PLV1 and PLV2 granites (1.08 ± 16 – 1.03 ± 10 Ga. Fig. 4.6). In addition, some monazite from the PLV2 granites yielded inherited, pre-Grenvillian ages (1355 ± 45 Ma – 1131 ± 37 Ma) and some monazite from the PLV1 granite yielded younger, Rigolet ages (1002 ± 14 and 985 ± 20 Ma).

Older pre-Grenvillian monazite ages (~1467 to ~1420 Ma) were reported by Dunning and Indares (2010) and Lasalle et al (2014) from PLV1 metapelites. Lack of these older monazite ages in the PLV granites may be attributed to more efficient dissolution of older monazites in the granitic melts relative to the residual rocks.

Late Grenvillian, Rigolet ages in monazite, ranging from 1010– 990 Ma are also reported from PLV1 metapelites by Lasalle et al. (2014). Collectively, these young monazite ages from the PLV1 granite and metapelites are aligned with independent evidence of a Rigolet thermal event in the mid-*P* belt south of the Manicouagan reservoir. In this area, there are widespread felsic pegmatites and ultrapotassic dykes with crystallization ages at 995 ± 3.5 Ma and 980 ± 3Ma, respectively (Dunning and Indares, 2010). Felsic pegmatites of similar ages were also reported farther south by Turlin et al. (2017) The composition of the PLV1 granite is not consistent with the type of melts produced in the Rigolet, suggesting that this granite might represent an Ottawan body that was reworked during the Rigolet, whereas the absence of Rigolet melts and monazite in the PLV2 could possibly indicate that the effect from the Rigolet was less important in this area.

6.4 Link Between the PLV Aluminous Rocks and the PLV Granite Bodies

According to the results from the petrology, geochronology, geochemistry and phase equilibria modelling, the PLV aluminous rocks and the PLV granites seem to be related. Monazite ages of PLV granites are consistent with the age of metamorphism of the mid-*P* aluminous rocks and their composition is consistent with melts produced by the PLV aluminous rocks through the biotite dehydration reaction. Even though processes such as the mixing of melts, fractional crystallization and wall-rock contamination are not assessed, these should not have a big influence in the overall leucosome composition, while the extracted melts are expected to be monzogranitic (Sawyer, 2008; Koblinger and Pattison, 2017; Pavan et al., 2021). This suggests that the PLV granites are the likely product of the partial melting of the PLV aluminous rocks and may be the only S-type Ottawan-age granites that were preserved for more than a thousand million years in the central Grenville Province.

References

Beaumont, C., Nguyen, M.H., Jamieson, R.A., Ellis, S., 2006. Crustal flow modes in large hot orogens. In: Law, R.D., Searle, M.P., Godin, L. (Eds.), Channel Flow, Ductile Extrusion, and Exhumation of Lower-Midcrust in Continental Collision Zones. Geological Society Special Publication, 268:91–145.

Brown, M., 2008. Granites, migmatites and residual granulites: relationships and processes, in Sawyer, E.W., and Brown, M., eds., Working with Migmatites: Mineralogical Association of Canada Short Course Series, v. 38:97–144.

Brown, M.., 2010. Melting of the continental crust during orogenesis: The thermal, rheological, and compositional consequences of melt transport from lower to upper continental crust. Canadian Journal of Earth Sciences. 47: 655–694.

Chakraborty, S., Ganguly, J., 1992. Cation diffusion in aluminosilicate garnets: experimental determination in spessartine-almandine diffusion couples, evaluation of effective binary diffusion coefficients, and applications. Contributions to Mineralogy and Petrology 111:74–86.

Coggon, R., & Holland, T.J.B., 2002. Mixing properties of phengitic micas and revised garnet phengite thermobarometers. Journal of Metamorphic Geology, 20(7) :683–696.

Cuney, M. & Barbey, P., 1982.Mise en évidence de phénomènes de cristallisation fractionée dans les migmatites. C. R. Académie des sciences Paris, 295 :37–42.

Dunning, G., Indares, A., 2010. New insights on the 1.7–1.0 Ga crustal evolution of the central Grenville Province from the Manicouagan–Baie Comeau transect. Precambrian Research, 180:204–226.

Ferry, J. M., Spear, F. S., 1978. Experimental calibration of the partitioning of Fe and Mg between biotite and garnet Contributions to Mineralogy and Petrology. 66:113–117.

Hetherington, C. J., Backus, E. L., McFarlane, C. R. M., Fisher, C. M., Pearson, D. G., 2017. Origins of textural, compositional, and isotopic complexity in monazite and its petrochronological analysis.Geophysical Monograph Series, 232: 63–90.

Hindemith, M., Indares, A., Piercey, S., 2017. Hydrothermally altered volcanic rocks metamorphosed at granulite-facies conditions: an example from the Grenville Province. Canadian Journal of Earth Sciences, 54(6): 622–638.

Holland, T.J.B., Powell, R., 1998. An internally-consistent thermodynamic dataset for phases of petrological interest. Journal of Metamorphic Geology, 16:309-344.

Holland, T.J.B., & Powell, R., 2003. Activity–composition relations for phases in petrological calculations: An asymmetric multicomponent formulation. Contributions to Mineralogy and Petrology, 145(4): 492–501.

Holland, T.J.B., & Powell, R., 2011. An improved and extended internally consistent thermodynamic dataset for phases of petrological interest, involving a new equation of state for solids. Journal of Metamorphic Geology, 29(3):333–383.

Holness, M.B., 2008. Decoding migmatite microstructures, in Sawyer, E.W., and Brown, M., eds., Working with Migmatites: Mineralogical Association of Canada Short Course Series, v. 38:57–76.

Holness, M.B., and Sawyer, E.W., 2008. On the pseudomorphing of melt-filled pores during the crystallization of migmatites: Journal of Petrology, v. 49:1343–1363.

Indares, A., 2020. Deciphering the metamorphic architecture and magmatic patterns of large hot orogens: Insights from the central Grenville Province. Gondwana Research. 80: 385-409 .

Indares, A., Moukhsil A., 2013. ca 1.2 Ga Crustal extension in the central Grenville Province: implications for the orogenic architecture and potential influence on the emplacement of anorthosites. Canadian Journal of Earth Sciences, 50(9): 955–966.

Indares, A., White, R.W., Powell, R., 2008. Phase equilibria modelling of kyanite-bearing anatectic paragneisses from the central Grenville Province. Journal of Metamorphic Geology, 26: 815–836.

Indares, A., Dunning, G., 2001. Partial melting of high-P–T metapelites from the Manicouagan Imbricate Zone (Grenville Province): evidence, interpretation and U-Pb geochronology. Journal of Petrology, 42: 1547–1565.

Jamieson, R.A., Beaumont, C., Nguyen, M.H., Culshaw, N.G., 2007. Syn-convergent ductile flow in variable strength continental crust: numerical models with application to the western Grenville Province. Tectonics 26(5): 5005–TC5005.

Jamieson, R.A., Beaumont, C., Warren, C.J., Nguyen, M.H., 2010. The Grenville orogen explained. Applications and limitations of integrating numerical models with geological and geophysical data. Canadian Journal of Earth Sciences, 47: 517–539.

Jamieson, R.A., Beaumont, C., 2011. Coeval thrusting and extension during lower crustal ductile flow – implications for exhumation of high-grade metamorphic rocks. Journal of Metamorphic Geology, 29, 33–51.

Jamieson, R.A., Beaumont, C., 2013. On the origin of orogens. Bulletin of the Geological Society of America, 125: 1671–1702.

Johannes,W., Holtz, F., 1996. Petrogenesis and Experimental Petrology of Granitic Rocks. Minerals and Rocks. v. 22: 0–355 pp. Springer-Verlag, Berlin

Jones, K.A., and Brown, M., 1990, High-temperature ‘clockwise’ P–T paths and melting in the development of regional migmatites: An example from southern Brittany, France: Journal of Metamorphic Geology, v. 8:551–578.

Jurewicz, S. R. & Watson, E. B., 1985. The distribution of partial melt in a granitic system: the application of liquid phase sintering theory. Geochimica et Cosmochimica Acta, 49: 1109–1121.

Kelsey DE, Clark C, Hand M., 2008. Thermobarometric modeling of zircon and monazite growth in melt-bearing systems: examples using model metapelitic and metapsammitic granulites. Journal of Metamorphic Geology, 26:199–212.

Kendrick, J., Indares, A., 2018a. The reaction history of kyanite in high-P aluminous granulites. Journal of Metamorphic Geology, 36: 125–146.

Kendrick, J., Indares, A., 2018b. The Ti record of quartz in anatectic aluminous granulites. Journal of Petrology, 59: 1493–1516.

Kohn, M. J., 2016. Metamorphic chronology – a tool for all ages: Past achievements and prospects: American Mineralogist, Volume 101: 25–42.

Koblinger, B.M., Pattison, D.R.M., 2017. Crystallization of heterogeneous pelitic migmatites: insights from thermodynamic modelling. Journal of Petrology 58: 297–326.

Lasalle, S., Fisher, C., Indares, A., Dunning, G., 2013. Contrasting types of Grenvillian granulite facies aluminous gneisses: Insights on protoliths and metamorphic events from zircon morphologies and ages. Precambrian Research, 228: 117–130.

Lasalle, S., Indares, A., 2014. Anatectic record and contrasting P–Tpaths of aluminous gneisses from the central Grenville Province. Journal of Metamorphic Geology, 32, 627–646.

Lasalle, S., Dunning, G., Indares, A., 2014. In situ LA–ICP–MS dating of monazite from aluminous gneisses: insights on the tectono-metamorphic history of a granulite-facies domain in the central Grenville Province. Canadian Journal of Earth Sciences, 51: 558–572.

Ludwig, K. R., 2003. “User’s Manual for Isoplot/Ex, Version 3.00. A Geochronological Toolkit for Microsoft Excel,” Berkeley Geochronology Center Special Publication, Vol. 4, No. 2: 1–70.

Moukhsil, A., Solgadi, F., Lacoste, P., Gagnon, M., David, J., 2012. Géologie de la région du lac duMilieu (SNRC 22O03, 22O04, 22O06, 22J13 et 22J14). Ministère des Ressources naturelles et de la Faune, RG, 1–31.

Palin, R. M., Dyck, B., 2021. Metamorphism of Pelitic (Al-Rich) Rocks, Encyclopedia of Geology (Second Edition), Academic Press, 445-456.

Patchett, P. J., Samson, S. D., 2003.Ages and growth of the continental crust from radiogenic isotopes Treatise on Geochemistry, 3:321–348.

Pavan, M.,Moraes, R.,Sawyer, E., 2021. Changes in the composition of anatectic melt and its complementary residue by forward-modelling using THERMOCALC, Lithos, 396:106220.

Patrick, M., Indares, A., 2017. Petrography and phase equilibria modeling of mid-P aluminous gneisses derived from hydrothermally altered protoliths, Grenville Province, Canada. Canadian Journal of Earth Sciences, 54: 1103–1118.

Powell, R., & Holland, T.J.B., 1988. An internally consistent dataset with uncertainties and correlations: 3. Applications to geobarometry, worked examples and a computer program. Journal of Metamorphic Geology, 6(2): 173–204.

Powell R. and Holland T. J. B., 2010.Using Equilibrium Thermodynamics to Understand Metamorphism and Metamorphic Rocks: Elements, 6: 309–314.

Evans, K. A. and Powell, R. and Holland, T. J. B., 2010. Internally consistent data for sulphur-bearing phases and application to the construction of pseudosections for mafic greenschist facies rocks in Na2O–CaO–K2O–FeO–MgO–Al2O3–SiO2–CO2–O–S–H2O. Journal of Metamorphic Geology, 28 (6):667-687.

Rivers, T., 2008. Assembly and preservation of lower, mid, and upper orogenic crust in the Grenville Province–Implications for the evolution of large hot long-duration orogens. Precambrian Research, 167: 237–259.

Rivers, T., 2012. Upper-crustal orogenic lid and mid-crustal core complexes: signature of a collapsed orogenic plateau in the hinterland of the Grenville Province. Canadian Journal of Earth Sciences, 49: 1– 42.

Rivers, T., Culshaw, N., Hynes, A., Indares, A., Jamieson, R., Martignole, J., 2012. The Grenville orogen – a post Lithoprobe perspective. In: Percival, J.A., Cook, F.A., Clowes, R.M. (Eds.), Tectonic Styles in Canada: The Lithoprobe Perspective. Geological Survey of Canada, Special Paper, 49: 97–236.

Rivers, T., Martignole, J., Gower, C. F., and Davidson, A., 1989. New tectonic divisions of the Grenville Province, Southeast Canadian Shield, Tectonics, 8(1): 63– 84.

Rivers, T., Corrigan, D., 2000. Convergent margin on southeastern Laurentia during the Mesoproterozoic: tectonic implications. Canadian Journal of Earth Sciences, 37: 359–383.

Rosenberg, C.L., Handy, M.R., 2005. Experimental deformation of partially melted granite revisited: implications for the continental crust. Journal of Metamorphic Geology, 23: 19–28.

Rivers, T., 2015.Tectonic Setting and Evolution of the Grenville Orogen: An Assessment of Progress Over the Last 40 Years. Geoscience Canada, 42: 77-124.

Slagstad, T., Hamilton, M.A., Jamieson, R.A., Culshaw, N.G., 2004. Timing and duration of melting in the mid orogenic crust: constraints from U-Pb (SHRIMP) data, Muskoka and Shawanaga domains, Grenville Province, Ontario. Canadian Journal of Earth Sciences, 41: 1339–1365.

Sawyer E. W., 1994. Melt segregation in the continental crust. Geology,, 22 (11): 1019–1022.

Sawyer E. W., 1999. Criteria for the recognition of partial melting, Physics and Chemistry of the Earth, Part A: Solid Earth and Geodesy.24 (3):269–279.

Sawyer, E.W., 2001, Melt segregation in the continental crust: Distribution and movement of melt in anatectic rocks: Journal of Metamorphic Geology, 19:.291–309.

Sawyer, E.W., 2008. Atlas of Migmatites. The Canadian Mineralogist, Special Publication 9. NRC Research Press, Ottawa, Ontario, Canada.1–371.

Sparkes, G., and Dunning, G., 2015. New U-Pb age constraints on the development of uranium mineralization within the Central Mineral Belt of Labrador: Newfoundland and Labrador Department of Resources Geologic Survey. Report 15–1: 105–113.

Spear, F., Florence, F. P., 1992. Thermobarometry in granulites: pitfalls and new approaches, Precambrian Research, 55(1–4): 209–241.

Spear, F., Kohn, M.,Cheney, J., 1999. P - T paths from anatectic pelites. Contributions to Mineralogy and Petrology. 134: 17–32.

Tohver, E., Bettencourt, J.S., Tosdal, R., Mezger, K., Leite, W.B., Payolla, B.L., 2004. Terrane transfer during the Grenville orogeny: tracing the Amazonian ancestry of southern Appalachian basement through Pb and Nd isotopes. Earth and Planetary Science Letters228: 161–176.

Turlin, F., André-Mayer, A.-S., Moukhsil, A., Vanderhaeghe, O., Gervais, F., Solgadi, F.,Groulier, P.-A. and Poujol, M., 2017. Unusual LREE-rich, peraluminous, monazite- or allanite-bearing pegmatitic granite in the central Grenville Province, Québec: Ore Geology Reviews, 89: 627–667.

Vanderhaeghe, O., Teyssier, C., 2001. Partial melting and flow of orogens. Tectonophysics, 342: 451–472.

Vernon, R.H., 2011. Microstructures of melt-bearing regional metamorphic rocks, in van Reenen, D.D., Kramers, J.D., McCourt, S., and Perchuk, L.L., eds., Origin and Evolution of Precambrian High-Grade Gneiss Terranes, with Special Emphasis on the Limpopo Complex of Southern Africa: Geological Society of America Memoir 207: 1–11.

Wei, C., Wang, W., 2007. Phase Equilibria in the Process of Anatexis in High-grade Metapelites. Earth Science Frontiers, 14(1): 125–134.

White, R.W., 2008. Petrological modeling of migmatites, in Sawyer, E.W., and Brown, M., eds.Working with Migmatites: Mineralogical Association of Canada Short Course Series, 38:77–96.

White, R. & Powell, R., 2002. Melt loss and the preservation of granulite facies mineral assemblages. Journal of Metamorphic Geology, 20: 621–632.

White, R.W., Powell, R., & Holland, T.J.B., 2007. Progress relating to calculation of partial melting equilibria for metapelites. Journal of Metamorphic Geology, 25(5): 511–527.

White, R.W., Powell, R., Holland, T.J.B., Johnson, T.E., & Green, E.C.R., 2014b. New mineral activity–composition relations for thermodynamic calculations in metapelitic systems. Journal of Metamorphic Geology, 32(3): 261–286.

Whitney, D. L., Evans, B.W., 2010. Abbreviations for names of rock-forming minerals. Am Mineral, 95: 185–187.

Yakymchuk, C., 2017. Applying Phase Equilibria Modelling to Metamorphic and Geological Processes: Recent Developments and Future Potential. Geoscience Canada, 44(1): 27–45.

Yakymchuk, C., Brown, M., 2014. Consequences of open-system melting in tectonics. Journal of the Geological Society. 171: 21–40.

Yakymchuk, C., Clark, C., White, R. W., 2017. Phase Relations, Reaction Sequences and Petrochronology. Reviews in Mineralogy and Geochemistry, 83(1): 13–53.

Yardley, B., Valley, J., 1997. The petrologic case for a dry lower crust. Journal of Geophysical Research B: Solid Earth. 102: 12173–12185.